



HAL
open science

Fabrication et propriétés physiques de conducteurs multifilamentaires MgB₂ dopés au carbone

Qingyang Wang

► **To cite this version:**

Qingyang Wang. Fabrication et propriétés physiques de conducteurs multifilamentaires MgB₂ dopés au carbone. Physique [physics]. Université de Grenoble; Northwestern Polytechnical University (Chine), 2012. Français. NNT : 2012GRENY115 . tel-00950672v2

HAL Id: tel-00950672

<https://theses.hal.science/tel-00950672v2>

Submitted on 6 May 2014

HAL is a multi-disciplinary open access archive for the deposit and dissemination of scientific research documents, whether they are published or not. The documents may come from teaching and research institutions in France or abroad, or from public or private research centers.

L'archive ouverte pluridisciplinaire **HAL**, est destinée au dépôt et à la diffusion de documents scientifiques de niveau recherche, publiés ou non, émanant des établissements d'enseignement et de recherche français ou étrangers, des laboratoires publics ou privés.



UNIVERSITÉ DE
GRENOBLE

THÈSE

Pour obtenir le grade de

DOCTEUR DE L'UNIVERSITÉ DE GRENOBLE

**préparée dans le cadre d'une cotutelle entre
l'Université de Grenoble et la Northwest
Polytechnical University de Xi'an**

Spécialité : **Physique des Matériaux**

Arrêté ministériel : le 6 janvier 2005 -7 août 2006

Présentée par

Qingyang WANG

Thèse dirigée par **Pingxiang ZHANG** et **André SULPICE**

préparée au sein des **Northwest Institute for Nonferrous Metal
Research** et **Institut Néel**

dans **les Écoles Doctorales Physique de Grenoble et NPU**

**Fabrication et propriétés physiques de conducteurs
multifilamentaires MgB₂ dopés au carbone**

Thèse soutenue publiquement le **25 septembre 2012**,
devant le jury composé de :

Françoise HIPPERT

Professeur Grenoble-INP , Présidente

Jacques NOUDEM

Professeur Université de Caen Rapporteur

Chengshan LI

Chercheur NIN Xi'an Rapporteur

Jinshan LI

Professeur NPU Membre

Rui HU

Professeur NPU Membre

Daniel CHATEIGNER

Professeur Université de Caen Membre

Pingxiang ZHANG

Professeur NPU Directeur de thèse

André SULPICE

DR CNRS , Directeur de thèse



ACKNOWLEDGEMENTS

This work would not have been possible without the support from the scholarship of France embassy in China and French-Chinese International Associated Laboratory LAS2M (Laboratory for the Applications of Superconductors and Magnetic Materials).

I have spent four years in Xi'an, China and in CNRS/Grenoble, France for which I am really grateful and enjoyable. There are many people I would like to thank during my Ph.D. research period. First, I should give my sincere appreciations to my supervisors, Prof. André Sulpice and Prof. Pingxiang Zhang for their understanding, encouragement and advices throughout the years of my Ph.D. studies.

I especially need to acknowledge Dr. Guo Yan, who is the leader of MgB₂ group in NIN, for his arrangement and guidance in MgB₂ wire and tapes fabrication. Many thanks to Prof. Chengshan Li, Prof. Ping Ji and Dr. Zeming Yu in SMRC/NIN, Dr. Bernard Hebral, Dr. Jean-louis Soubeyroux and Dr. Eric Beaugnon in CRETA/CNRS and Prof. Jinshan Li, Prof. Rui Hu and Prof. Hongchao Kou in NPU for their support and providing convenience during the past four years. I have truly appreciated CRETA, Institut Néel, LNCMI/CNRS, SMRC, Analysis Center/NIN and WST for their help and assistance in my experiments and measurements.

I also thank Xiaomei Xiong, Gaofeng Jiao, Guoqing Liu and the whole MgB₂ research group in NIN for their help on fabricating MgB₂/Nb/Cu wires. I am deeply indebted to Pierre Brosse-Marion and Joël Balay for their enthusiastic work during my sample preparation. I am also grateful to Sébastien Pairis, Laureline Porcar in CNRS for their excellent microscopy skills. And I would like to sincerely thank Eric Mossang, Xavier Chaud and Laureline Porcar for their help and convenience in critical current measurements.

I want to thank my Chinese friends who accompany with me in France: Zihui Peng, Jinna MEI, Haixia Zhang, Jun Wang and Zhaosheng Wang, *et al.* Especially, I want to express my gratitude to André Sulpice. I have got his enormous help in my research and live when I stay in France.

I would like to express my thanks to Fang Yang, Shengnan Zhang, Di Shan,

Jianqing Feng, Xifeng Pan, Yuyan Sun and Chao Li for their help in analyzing the experimental data and revising the manuscript draft.

I would like to express my sincere thanks to my doctoral committee for their excellent instruction for my Ph.D. dissertation refereeing and oral examination.

Lastly, I am forever grateful to my wife and my family for their love, support, understanding and encouragement during my extensive Ph.D. career.

A word of thanks is given to all the people who help me!

Merci beaucoup!

TABLE OF CONTENTS

ACKNOWLEDGEMENTS	I
TABLE OF CONTENTS	III
LIST OF FIGURES AND TABLES.....	VII
LIST OF ABBREVIATIONS AND SYMBOLS	XII
CHAPTER 1 INTRODUCTION	1
1.1 Superconductivity.....	1
1.1.1 Fundamentals of superconductivity theory	2
1.1.1.1 The Cooper Pairs.....	2
1.1.1.2 The Coherence Length.....	2
1.1.1.3 The penetration depth.....	3
1.1.1.4 The Meissner Effect	3
1.1.1.5 The BCS theory	4
1.1.2 Type-I and Type-II superconductors	4
1.2 Superconductivity of MgB ₂	5
1.2.1 Background	5
1.2.2 The fundamental properties of MgB ₂	6
1.2.3 The phase diagram of MgB ₂	9
1.3 Element and compound doping of MgB ₂	11
1.3.1 Metallic element doping	12
1.3.2 Non-metallic element doping	12
1.3.3 Compound doping.....	14
1.4 The fabrication method of MgB ₂ superconducting wires	15
1.4.1 Mg infiltration method	15
1.4.2 Powder-in-tube technology	16
1.4.2.1 <i>In-situ</i> PIT technique	17
1.4.2.2 <i>Ex-situ</i> PIT technique	17
1.4.3 The Continuous Tube Forming and Filling process	17
1.4.4 The Internal Magnesium Diffusion method	18

1.4.5 The sheath materials.....	19
1.5 Long length MgB ₂ wires and tapes fabrication	20
1.6 The typical application of MgB ₂ superconductor.....	22
1.7 Motivation	24
1.8 Thesis arrangement	25
CHAPTER 2 FABRICATION AND ANALYSIS WAY OF MgB₂ WIRES	27
2.1 Fabrication process of MgB ₂ wires	27
2.1.1 Conductor design	27
2.1.2 Fabrication of mono- and multi-filamentary MgB ₂ wires	27
2.1.3 Heat treatment process.....	28
2.2 Phase formation analysis	29
2.3 Microstructure observation	30
2.3.1 Scanning Electron Microscope Analysis.....	30
2.3.2 Electron Probe Micro-Analysis	31
2.3.3 Magneto-Optical analysis.....	32
2.4 Characterization of superconducting properties.....	33
2.4.1 Magnetization measurement.....	33
2.4.2 Resistivity measurement.....	34
2.4.3 Transport critical current measurement.....	35
CHAPTER 3 THE PROPERTIES OF <i>IN-SITU</i> MONO-FILAMENTARY	
MgB₂/Nb/Cu WIRES	37
3.1 Sample fabrication.....	37
3.2 Phase formation analysis of MgB ₂ /Nb/Cu wires.....	38
3.3 Microstructure analysis of MgB ₂ /Nb/Cu wires.....	41
3.4 Superconducting performance of MgB ₂ /Nb/Cu wires	44
3.4.1 Critical temperature T_c derived by magnetization and resistance.....	44
3.4.2 Transport critical current density J_c of MgB ₂ /Nb/Cu wires	47
3.4.2.1 Short length MgB ₂ /Nb/Cu sample	47
3.4.2.2 J_c - B performance of MgB ₂ /Nb/Cu coil.....	50
3.5. The interface between Nb and MgB ₂ core	52
3.5.1 EDS analysis of MgB ₂ -Nb interface	53

3.5.2 Magneto-Optical Imaging analysis of the MgB ₂ -Nb interface.....	56
3.5.3 Phase formation at MgB ₂ -Nb interface.....	59
3.5.4 Electron Probe Micro-Analysis of MgB ₂ -Nb interface.....	61
3.6 Conclusion	64
CHAPTER 4 EFFECT OF CHEMICAL DOPING ON MgB₂/Nb/Cu WIRES...65	
4.1 Sample preparation	65
4.2 Phase formation of chemical doping MgB ₂ wire	66
4.2.1. Influence of doping content on the phase formation	66
4.2.2. Influence of sintering temperature on the phase formation	72
4.3 Microstructure of chemical doping MgB ₂ wire	75
4.4 Superconductivity of chemical doping MgB ₂ wire	75
4.4.1 The <i>M-T</i> performance of chemical doping MgB ₂ wire.....	75
4.4.2 The <i>R-T</i> performance of chemical doping MgB ₂ wire.....	77
4.4.3 The <i>M-H</i> performance of chemical doping MgB ₂ wire	82
4.4.4 The <i>J_c-B</i> performance of chemical doping MgB ₂ wire	85
4.5 Conclusion	87
CHAPTER 5 FABRICATION AND PROPERTIES OF MULTICORE MgB₂ WIRES WITH Nb REINFORCEMENT89	
5.1 Conductor structure design and the sample fabrication	89
5.2 Mechanical properties of Nb reinforced multi- filamentary MgB ₂ wires	92
5.2.1 Stress-strain analysis of multi-filamentary MgB ₂ wires.....	92
5.2.2 Bending strain analysis of mono- and multi-filamentary MgB ₂ wires.....	95
5.3 Magneto-optical analysis of multi-filamentary MgB ₂ /Nb/Cu wires	100
5.4 Superconductivity of the multi-filamentary MgB ₂ wires.....	102
5.5 Critical current of 100 meter MgB ₂ /Nb/Cu wires	106
5.6 Current homogeneity on 6-filamentary MgB ₂ wires.....	107
5.7 Conclusion	108
CHAPTER 6 SUMMARY.....109	
REFERENCE.....113	

PUBLICATIONS121

LIST OF FIGURES AND TABLES

FIGURE DESCRIPTION PAGE

CHAPTER 1

Figure 1-1	Critical surface of superconducting state and normal state	1
Figure 1-2	Diagram of the Meissner effect. Flux lines are excluded from a superconductor when it is below its critical temperature	4
Figure 1-3	The difference between type I and type II superconductor.....	5
Figure 1-4	The hexagonal (AlB ₂ -type) crystal structure of MgB ₂	6
Figure 1-5	Comparison of the crystal structures of MgB ₂ and some others practical superconductors.....	7
Figure 1-6	Temperature dependence of upper critical field of MgB ₂ single crystal. Inset shows the anisotropy of the upper critical field, $\gamma_a = H_{ab\ c2} / H_{c\ c2}$	8
Figure 1-7	The phase diagrams of the Mg-B system under the Mg vapor pressure of 1atm.....	10
Figure 1-8	The DTA curve of mixture of Mg:B = 1:2 ^[22]	10
Figure 1-9	Critical surfaces of MgB ₂ , NbTi and Nb ₃ Sn ^[23]	11
Figure 1-10	The first MgB ₂ wires fabricated by infiltration method ^[77]	15
Figure 1-11	Schematic diagram of the Powder in tube process (PIT).....	16
Figure 1-12	Sketch map of Continuous Tube Filling and Forming (CTFF) process.....	18
Figure 1-13	Schematic diagram of the Internal Magnesium Diffusion process (IMD)	19
Figure 1-14	Transverse cross section of the MgB ₂ superconducting tape fabricated by Columbus Superconductors	21
Figure 1-15	Cross section of typical 18+1 multifilament MgB ₂ wire fabricated by Hyper Tech Research.....	22
Figure 1-16	The MgB ₂ -based, cryogenic free, open MRI magnet as delivered from ASG Superconductors to Paramed (left) and first brain image acquired by Paramed Medical Systems on the MR-Open system (right)	23
Figure 1-17	Photograph of MgB ₂ SFCL prototypes (left) and detail of electrical connections (right) ^[104]	24

CHAPTER 2

Figure 2-1	Schematics of the <i>in-situ</i> PIT process for the fabrication of multi-filamentary MgB ₂ /Nb/Cu wires and tapes	28
Figure 2-2	A temperature profile for the annealing of MgB ₂ wires	29
Figure 2-3	Schematic diagram of the Scanning Electron Microscope	

	Equipment.....	30
Figure 2-4	The sketch map of Faraday Effect	32
Figure 2-5	Photograph of Magneto Optical Equipment	32
Figure 2-6	Design of the pick-up coil with the superconducting coil (a) and magnetic flux in the coil versus the position of the sample (b).....	33
Figure 2-7	The sample holder for resistance measurement.....	34
Figure 2-8	Schematic diagram of standard Four-probe method for the MgB ₂ wires	35
Figure 2-9	Illustration of the facility for transport current measurement.....	36
CHAPTER 3		
Figure 3-1	XRD patterns of MgB ₂ wire sintered at different temperature	38
Figure 3-2	Comparisons of the characteristic peaks (002) and (110).....	39
Figure 3-3	Lattice parameter of MgB ₂ wires heat treated at different temperature	39
Figure 3-4	The FWHM value of MgB ₂ wires heat treated at different temperature	40
Figure 3-5	XRD patterns of short sample and long wires heat treatment at 800 °C	41
Figure 3-6	Microstructure of MgB ₂ wires heat treated at various temperature of a) 650 °C, b) 700 °C, c) 750, d) 800 °C, e) 850 °C, and f) 900 °C.....	42
Figure 3-7	SEM pictures of MgB ₂ wires at larger magnification, a) 650 °C, b) 750 °C, and c) 850 °C	43
Figure 3-8	Magnetization curves of MgB ₂ wires with various sintering temperatures.....	44
Figure 3-9	Sintering temperature dependence curve of T_c , T_c 's are obtained from the onset of superconducting transition curves during the magnetization measurement.	44
Figure 3-10	T_c of MgB ₂ wire after heat treated at various temperatures.....	45
Figure 3-11	Relationship between heat treatment temperature and T_c	46
Figure 3-12	The residual resistance just below the transition point dependence on heat treatment temperature.....	47
Figure 3-13	Voltage-Current Curves of the MgB ₂ /Nb/Cu wires heat	

	treated at (a) 650 °C and (b) 850 °C at 4.2K.....	48
Figure 3-14	Transport J_c of short MgB ₂ /Nb/Cu wires with different sintering temperatures at 4.2K.....	49
Figure 3-15	The coils with MgB ₂ wires for transport current measurement.....	50
Figure 3-16	Transport J_c as a function of the field for MgB ₂ coil at 4.2K.....	52
Figure 3-17	EDS Analysis of the interface layer between MgB ₂ and Nb.....	54
Figure 3-18	EDS analysis of MgB ₂ superconductor filament.....	55
Figure 3-19	Magneto-optical image of MgB ₂ wires heat treated at 650 °C under the magnetic fields from zero to 100 mT.....	56
Figure 3-20	Magneto-optical image of MgB ₂ wires heat treated at 800 °C under the magnetic fields from zero to 100 mT.....	57
Figure 3-21	MOI of the samples heat-treated at 800 °C for different time from 5 hours to 30 hours.....	59
Figure 3-22	B-Nb phase diagram.....	60
Figure 3-23	XRD pattern of MgB ₂ -Nb interface.....	61
Figure 3-24	EPMA element maps for niobium (b) and boron (c) of the MgB ₂ /Nb/Cu wires heat treated at 900 °C.....	62
Figure 3-25	EPMA line scanning of MgB ₂ -Nb interface of the MgB ₂ wires heat treated at 900 °C.....	63

CHAPTER 4

Figure 4-1	XRD pattern of MgB _{2-x} C _x ($x = 0, 0.05, 0.08, 0.1, 0.15$) wires heat treated at 650 °C (a) and 700 °C (b).....	67
Figure 4-2	XRD pattern of MgB _{2-x} (TiC) _x ($x = 0, 0.05, 0.08, 0.1, 0.15$) wires heat treated at 650 °C (a) and 700 °C (b).....	68
Figure 4-3	Comparison of (002) and (110) characteristics peak of MgB _{2-x} C _x wires.....	70
Figure 4-4	Comparison of (002) and (110) characteristics peak of MgB _{2-x} (TiC) _x wires.....	71
Figure 4-5	Crystal parameters of MgB ₂ /Nb/Cu wires with TiC and C doping.....	72
Figure 4-6	XRD pattern of MgB _{1.92} (TiC) _{0.08} heat treated at different temperatures.....	73
Figure 4-7	lattice parameter of MgB _{1.92} (TiC) _{0.08} wires heat treated at	

	different temperatures	74
Figure 4-8	Second electron image of $\text{MgB}_{1.92}(\text{TiC})_{0.08}$ wires heat treated at 700 °C	75
Figure 4-9	Magnetic moment as a function of temperature on $\text{MgB}_{1.92}(\text{TiC})_{0.08}$ wires heat treated at different temperatures.....	76
Figure 4-10	Critical temperature as a function of doping content on $\text{MgB}_{1.92}(\text{TiC})_{0.08}$ wires heat treated at different temperatures.....	77
Figure 4-11	Resistance depend on the temperature of $\text{MgB}_{2-x}(\text{TiC})_x$ wires heat treated at 700 °C (a) and 750 °C(b).....	78
Figure 4-12	The field dependence of the R-T curves of the $\text{MgB}_{2-x}(\text{TiC})_x$ wires in 3.0 T, 2.5 T, 2.0 T, 1.5 T, 1.0 T, 0.5 T and 0 T from left to right in perpendicular fields.....	81
Figure 4-13	T_c verses magnetic field of MgB_2 wires with TiC doping	82
Figure 4-14	M - H curves of the $\text{MgB}_{1.92}(\text{TiC})_{0.08}$ wires heat treated at different temperatures	83
Figure 4-15	Magnetic J_c versus applied field for the $\text{MgB}_{1.92}(\text{TiC})_{0.08}$ wires at different temperatures.....	84
Figure 4-16	Normalized flux pinning force as a function of magnetic field at 20 K for the pure and TiC doped samples sintered at different temperature.....	85
Figure 4-17	Transport J_c of MgB_2 and $\text{MgB}_{1.92}(\text{TiC})_{0.08}$ at 4.2K with the magnetic field up to 16 T	86
Figure 4-18	Transport J_c of $\text{MgB}_{2-x}(\text{TiC})_x$ with the field up to 16 T at different testing temperature	87
CHAPTER 5		
Figure 5-1	The cross section of the $\text{MgB}_{1.92}(\text{TiC})_{0.08}/\text{Nb}/\text{Cu}$ wires with different filament. (a) mono-filamentary, (b) 6-filamentary, (c) 12-filamentary and (d) 36-filamentary	90
Figure 5-2	The tensile stress vs strain curve of 6-filamentary MgB_2 wires with (a) or without (b) Nb reinforcement heat treated at 680 °C for 1.5 hours.....	92
Figure 5-3	Room-temperature stress-strain curves of $\text{MgB}_2/\text{Nb}/\text{Cu}$ wires with 6-, 12- and 36-filamentary.....	93
Figure 5-4	The voltage depend on the current curve of MgB_2 wires with different stress at 20K	94
Figure 5-5	The bending strain measurement holder	96
Figure 5-6	Critical current declines dependent on the bending of different filamentary wires.....	97

Figure 5-7	Compare of the J_c reduce with the bending of 6-filamentary wires and tapes	98
Figure 5-8	Critical current I_c change with the bending and straighten of the wires	99
Figure 5-9	Crack in mono-filamentary (a) and 6-filamentary (b) MgB_2 wires heat treated at 700 °C	100
Figure 5-10	The Optical microscopy image (a) and Magneto-optical image (b-g) of 6-filamentary MgB_2 wires at 6 K with a perpendicular applied field from 0 to 100 mT	101
Figure 5-11	Transport J_c as a function of magnetic field on $MgB_{1.92}(TiC)_{0.08}$ wires with different filaments.....	102
Figure 5-12	Transport J_c as a function of magnetic field on 6-filamentary $MgB_{1.92}(TiC)_{0.08}$ wires at 4.2 K with the field up to 10 T	103
Figure 5-13	Transport J_c as a function of magnetic field on 6-filamentary $MgB_{1.92}(TiC)_{0.08}$ wires	104
Figure 5-14	Critical current I_c as a function of temperature on 6-filamentary $MgB_{1.92}(TiC)_{0.08}$ wire	105
Figure 5-15	Critical current measurement of 100 meter $MgB_2/Nb/Cu$ wires.....	106
Figure 5-16	Homogeneity of the critical current in 100 meter MgB_2 wire (20K, 1T).....	107

TABLE DESCRIPTION PAGE

Table 1-1	Fundamental superconducting properties of the practical superconductors	9
Table 5-1	The volume percent of Cu, Nb and MgB_2 phase in the different conduct structure $MgB_{1.92}(TiC)_{0.08}/Nb/Cu$ wires.	90
Table 5-2	The mechanical properties of multi-filamentary $MgB_2/Nb/Cu$ wires	93

LIST OF ABBREVIATIONS AND SYMBOLS

AC	Alternating Current
BCS	Bardeen, Cooper, and Schrieffer theory
BSCCO	Bismuth Strontium Calcium Copper Oxide
Bi-2223	$\text{Bi}_2\text{Sr}_2\text{Ca}_2\text{Cu}_3\text{O}_{10+x}$ Superconductor
CTFF	Continuous Tube Forming and Filling process
DC	Constant Current /Direct Current
DTA	Differential thermal analysis
EDS	Energy Dispersive Spectrometer
EMPA	Electron Micro Probe Analyzer
FC	Field Cooled
FCL	Fault Current Limiters
FWHM	Full Width of Half Maximum
FT	Fourier Transform
GL	Ginzburg-Landau parameter
HTS	High Temperature Superconductors
IMD	Inter Magnesium Diffusion method
ITER	International Thermonuclear Experimental Reactor
LHe	Liquid Helium
LTS	Low Temperature Superconductor
MagLev	Magnetic Levitation
MgB_2	Magnesium Diboride Superconductor
MO	Magneto-Optical
MOL	Magneto-Optical Layer
MRI	Magnetic Resonance Imaging
NMR	Nuclear Magnetic Resonance
OFHC	Oxygen Free High Conductivity copper
PIT	Powder-In-Tube technique
RRR	Residual Resistance Ratio
SEI	Secondary Electron Imaging
SEM	Scanning Electron Microscopy
SI	Système International d'unités
SMES	Superconducting Magnetic Energy Storage
SPM	Scanning Probe Microscope

SQUID	Superconducting QUantum Interference Device
SS	Stainless Steel
TG	Thermo Gravimetry
W&R	Wind and Reaction
XRD	X-Ray Diffraction
YBCO	YBa ₂ Cu ₃ O ₇ Superconductor
YIG	Yttrium Iron Garnet
ZFC	Zero Field Cooled
<i>a. u.</i>	Arbitrary Unit
<i>B</i>	Magnetic flux density
<i>B_c</i>	Critical magnetic flux density
<i>B_{c1}</i>	Lower critical magnetic flux density
<i>B_{c2}</i>	Upper critical magnetic flux density
<i>B_{irr}</i>	Irreversible magnetic flux density
<i>e</i>	Electronic charge
<i>E</i>	quantity of energy
<i>F_p</i>	Flux pinning force
<i>F_p^{max}</i>	Maximum flux pinning force
<i>H</i>	Magnetic field intensity
<i>H_{c1}</i>	The lower critical field
<i>H_{c2}</i>	The upper critical field
<i>H_{irr}</i>	Irreversible critical field
<i>I</i>	Current
<i>I_c</i>	Critical current
<i>J_e</i>	Engineering critical current density
<i>J_c</i>	Critical current density
<i>L</i>	Inductance
<i>m</i>	magnetic moment
<i>M</i>	Magnetization of the superconducting sample
<i>ΔM</i>	Vertical width of the magnetization loop
<i>P</i>	Pressure
<i>q</i>	Electric charge
<i>R</i>	Resistance
<i>R_{norm}</i>	Normal zone resistance

T	Temperature
T_c	Critical temperature
U	Voltage
U_c	Voltage criterion
W	Power
α	Rotation angle of the polarization direction of the light
β	Coefficient of absorption of the MOL
ρ	density
Φ	Magnetic flux
μ	permeability
χ	susceptibility
Λ	Light wavelength
λ	Penetration depth
λ_{ab}	Penetration depth parallel to the a-b planes
μ_0	Magnetic permeability in space
ξ	Coherence length
ξ_{ab}	Coherence length parallel to the a-b planes
ξ_c	Coherence length perpendicular to the a-b planes

CHAPTER 1

INTRODUCTION

1.1 Superconductivity

The superconductivity phenomenon was first discovered by Kamerlingh Onnes on mercury at liquid helium temperature in 1911^[1]. One of the important properties of superconductivity is that the electrical resistance suddenly drops to zero when the temperature goes below the characteristic temperature, namely critical transition temperature (T_c); and such a material is named superconductor. There is no energy loss when using superconductors for transport electrical DC current.

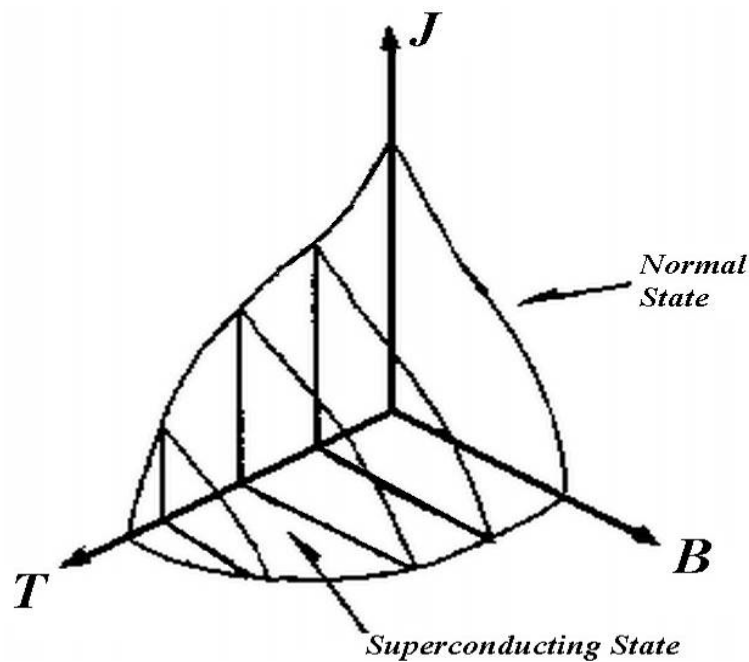


Figure 1-1 Critical surface of superconducting state and normal state

However, if a large current is put through a superconductor, it will change to the normal state, even it is still below its transition temperature. This is because the electrical current in a superconductor wire creates a magnetic field around the wire. The strength of the magnetic field increases with increasing current in the wire. If the magnetic field is increased to a critical point, the superconductor will return to the normal resistive state. The maximum value for the magnetic field at a certain

temperature is known as the critical magnetic field (H_c). Based on the analysis above, there should be a maximum current value that a superconductor can carry, namely critical current density (J_c), and J_c is a function of temperature. T_c , J_c and H_c are three crucial parameters for a certain superconductor.

Figure 1-1 shows the relationship of these three parameters, each of them is mutually dependent on the other two properties. Maintaining the superconducting state requires each of these parameters remains below the critical values, all of which depend on the material.

1.1.1 Fundamentals of superconductivity theory

1.1.1.1 The Cooper Pairs

When a material is cooled below the critical temperature, the free electron gas transforms from the normal state to a quantum fluid of coherent electron pairs in the reciprocal space. Each individual pair is formed when one electron with momentum combine with another electron of exactly the opposite momentum and spin, giving a net momentum of zero. These charge carriers are called the “Cooper pairs”^[2].

1.1.1.2 The Coherence Length

The dimension between the paired electrons in a Cooper pair is generally called the “coherence length” (ξ), which has a value varying between a few hundreds to more than ten thousand angstroms in metals. The partners in the Cooper pair are only a few angstroms away from the nearest electrons in other pairs. This makes the mechanism of such a fluid flow different from that of the normal electron gas. The coherence length is a fundamental length scale which is a function of temperature as follow:

$$\xi^2(T) = \frac{\hbar^2}{2m^* a(T)} \quad (1-1)$$

where m^* is the mass of a superconducting electron in a Cooper pair and $a(T)$ is a temperature dependent parameter in the Ginzburg-Landau (GL) equation:

$$a(T) \approx a_0[(T/T_c) - 1] \quad (1-2)$$

1.1.1.3 The penetration depth

A superconductor is able to exclude magnetic field by forming surface shielding currents which flow in a direction of creating an opposite magnetic field that cancels the applied field and remains no net flux density ($B = 0$) within the superconductor. However, these shielding currents are not confined entirely to the surface, otherwise the resulting current density would be infinite. The surface layer depth where the shielding current penetrated in is defined as the penetration depth (λ) with a dependence of temperature as the following equation:

$$\lambda(T) = \frac{\lambda_0}{\sqrt{1 - (T/T_c)^4}} \quad (1-3)$$

where λ_0 is the penetration depth at 0K, which is a material characteristic.

1.1.1.4 The Meissner Effect

In 1933, H. Walter Meissner and his student Robert Ochsenfeld analyzed the magnetic characteristics of superconductors and discovered that when a superconducting material makes the transition from normal state to superconducting state under a certain external magnetic field, the flux lines are expelled from the interior of the superconductor and then the magnetic field inside the superconductor is zero. The perfect diamagnetic property was obtained in this material. This effect was named the Meissner effect and known to occur because the screening current, induced on the surface by the external field, generates an interior field, which flows in a direction to exactly cancel the applied field within the material. But it does not occur in a perfect conductor in the normal state.

The Meissner effect is also recognized as a factor that determines whether a material is a superconductor. As shown in Figure 1-2, a simple experiment to demonstrate the Meissner effect in a laboratory is to put a small permanent magnet on the surface of a superconductor sample. If the superconductor is not cooled or the sample is a perfect conductor the magnet will stay in there unvarying with the flux penetrating into the sample. However, if a superconductor sample is cooled to below its T_c , an electric current will run on the surface of the sample creating an opposing magnetic field that interacts with the existing field from the magnet. By doing so, a repulsive force is generated to cancel the field in the interior of the sample.

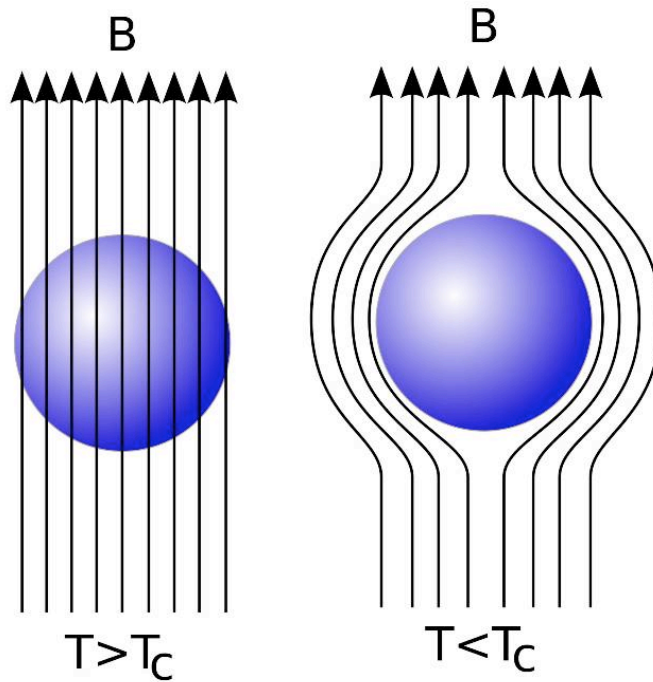


Figure 1-2 Diagram of the Meissner effect. Flux lines are excluded from a superconductor when it is below its critical temperature

1.1.1.5 The BCS theory

The first microscopic theory of superconductivity was proposed in 1957 by three physicists: Bardeen, Cooper and Schrieffer [2]. This theory is known as the BCS theory. It is based on the phonon-mediated coupling of electrons with opposite moment and spins to form pairs, known as Cooper pairs. The coherence length (ξ) corresponds to the size of such pair. This theory describes accurately the superconductivity phenomenon in LTS. However, it fails to fully explain some experimental observations in HTS, such as their high T_c and magnetic history dependence. Up to now, a theory accounting for all the observed superconducting properties in HTS still needs to be established.

1.1.2 Type-I and Type-II superconductors

The superconductor materials have been divided into two groups based on their behavior in magnetic fields: type-I and type-II superconductors. As shown in Figure 1-3, there are two critical fields in type-II superconductors, the lower critical field (H_{c1}) and the upper critical field (H_{c2}). If the external magnetic field is lower than H_{c1} ,

the field can be completely expelled and the material behaves the same as the type-I superconductor. By increasing the field above H_{c1} up to H_{c2} , the magnetic flux can not be completely excluded, but partially penetrates into the superconductor as vortices, which are called mixed state. The diameters of these vortices are of the order of the superconducting coherence length (ζ). As the field increases towards H_{c2} , the entire sample was totally penetrated by the magnetic flux and it returns to the normal state. When a type-I superconductor is placed in a weak external magnetic field, the field penetrates the superconductor within only a limited distance, which is called the penetration depth (λ).

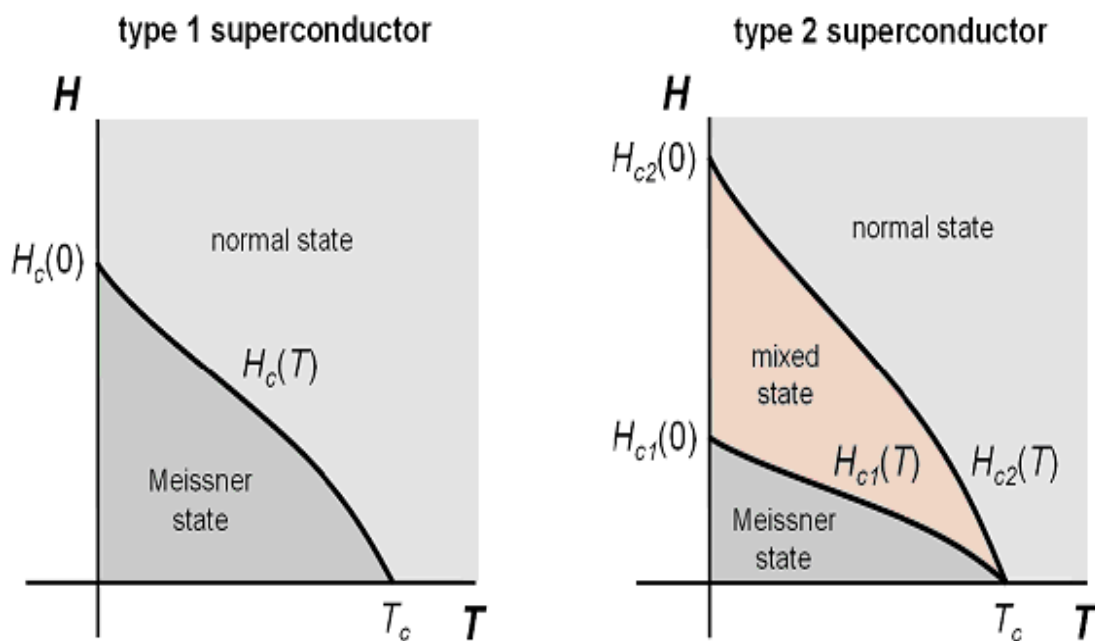


Figure 1-3 Difference between type I and type II superconductor

Since the discovery of superconductivity, physicists have discovered a wide variety of superconducting materials, including pure metal, alloy, metallic compound, oxide ceramic and organic compound, all of which lose their electrical resistance at low temperatures.

1.2 Superconductivity of MgB₂

1.2.1 Background

The superconductivity of MgB₂ was discovered by Akimitsu Jun and his team in 2001^[3] although MgB₂ was known since 1950. MgB₂ superconductor is the simple

metallic binary compound which has the highest critical temperature. The critical temperature of around 39 K is nearly twice the temperature of the intermetallic superconductors at that time. Of course, this announcement had excited the tremendous research passion from fundamental physics properties to practical application research around the world.

MgB₂ superconductor would be a high quality material for both large scale applications and electronic devices due to its high critical temperature T_c , large coherence lengths ξ , high critical current densities J_c , simple crystal structure, and high upper critical fields H_{c2} , as well as the transparency of its grain boundaries to current [4]. MgB₂ has been fabricated into various shapes such as bulks [5], [6], single crystals [7], [8], thin films [9], [10], wires [11], [12] and tapes [13], [14], *etc.* An abundant published research results revealed the great interest community in this materials.

1.2.2 The fundamental properties of MgB₂

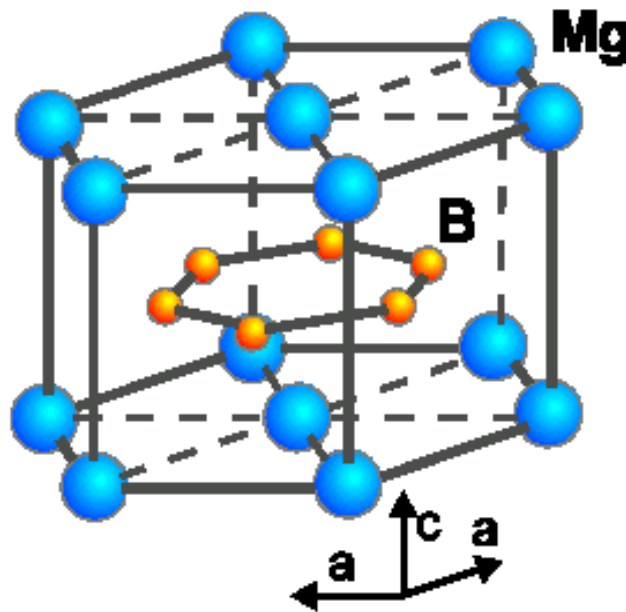


Figure 1-4 Hexagonal (AlB₂-type) crystal structure of MgB₂

Compared with the traditional metallic low-temperature superconductors (LTS) and the copper oxide high-temperature superconductors (HTS), MgB₂ has prominent characteristic, the critical temperature is obviously higher than LTS, and less serious problem of anisotropy and weak links at grain boundaries, which are unavoidable in HTS.

The crystal structure of MgB₂ is shown in Figure 1-4. It is a simple binary compound and has a hexagonal AlB₂ type structure similar to those of other kinds of boride. Its unit structure consists of alternating hexagonal layers of magnesium atoms and graphite-like honeycomb layers of boron atoms. The boron planes are separated by the layers of magnesium, and magnesium atoms are closely packed with each magnesium atom situated in between the centers of the hexagons forming each of the boron lattice planes. In each boron layer, each of the hexagons consists of six boron atoms, giving an overall 1:2 Mg-B ratio in the unit cell. The entire material structure of MgB₂ is anisotropic^{[15],[16]}, the in-plane B-B distance is significantly shorter than the distance between layers.

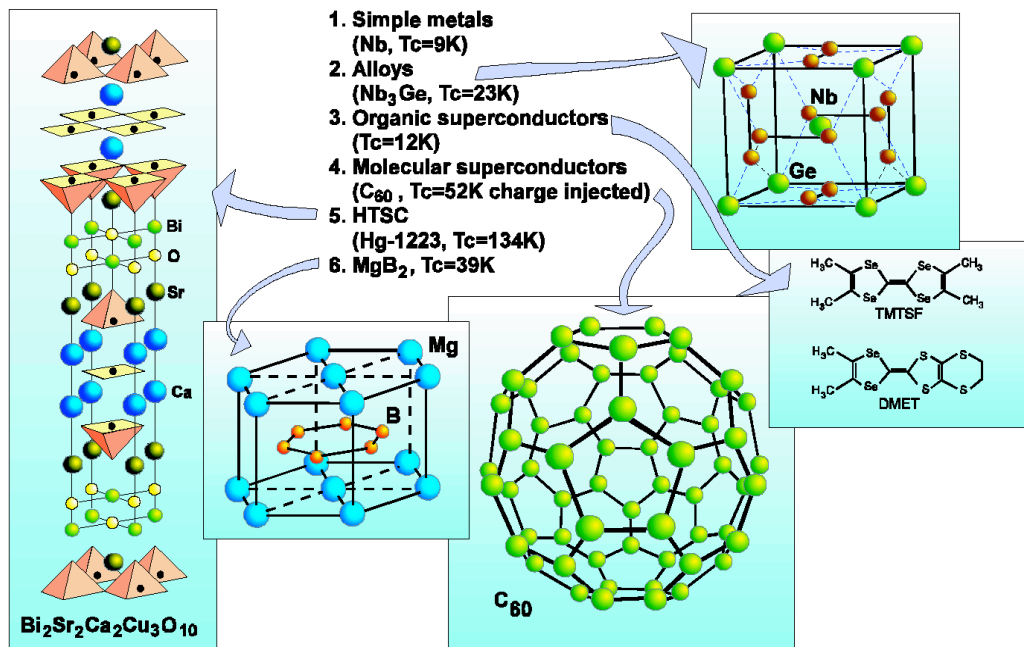


Figure 1-5 Comparison of the crystal structures of MgB₂ and some others practical superconductors

In Figure 1-5, the crystal structure of MgB₂ was compared with other practical superconductors. Similar to graphite, MgB₂ exhibits a strong anisotropy in the B–B lengths, the distance between the boron planes is significantly longer than the in plane B–B distance^[17]. At ambient temperature, the lattice parameters is $a = b = 0.3086$ nm, $c = 0.3521$ nm. Hence, the electromagnetic properties show the anisotropy due to the crystal structure, and the coherence length in the a - b plane is longer than that along c -axis, resulting in a lower value of the upper critical field for the magnetic field

direction along c -axis normal to the plane, as shown in Figure 1-6 [18]. The anisotropy of the upper critical field is shown in the inset. It is shown that the anisotropy factor is about 2 at the critical temperature and increases with decreasing temperature.

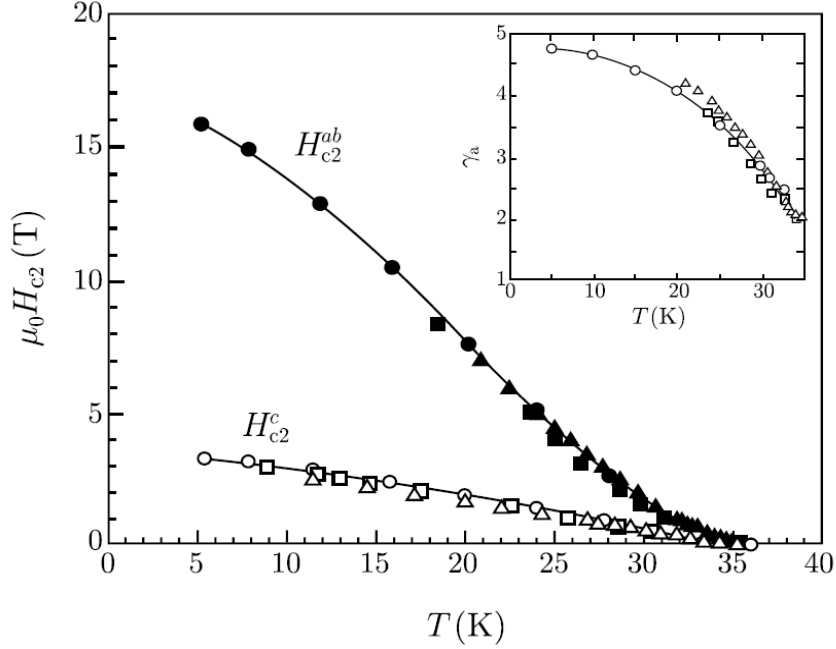


Figure 1-6 Temperature dependence of upper critical field of MgB₂ single crystal.

Inset shows the anisotropy of the upper critical field, $\gamma_a = H_{c2}^{ab} / H_{c2}^c$ [18]

The coherence lengths estimated from the upper critical fields are approximately $\xi_c(0)=9.6$ nm and $\xi_{ab}(0)=2.0$ nm. These are considerably longer than that in high-temperature superconductors, so the flux pinning properties of MgB₂ is probably similar with the traditional metallic superconductors. The typical parameter of MgB₂ and other practical superconductors are shown in Table 1-1.

Many magnetization and transport measurements show that MgB₂ does not exhibit weak-link electromagnetic behavior at grain boundaries [4] or fast flux creep [19]. The transport measurements in high magnetic fields of dense bulk samples yield very similar J_c values to those from magnetization measurements [20]. This confirms that the inductive current flows coherently all the way through the sample, unaffected by grain boundaries. As a result the flux motion will decide the J_c dependence on both field and temperature.

Table 1-1 Fundamental superconducting properties of the practical superconductors

Parameter	NbTi	Nb ₃ Sn	MgB ₂	YBCO	Bi-2223
T_c (K)	9	18	39	92	110
Anisotropy	Negligible	Negligible	1.5~5	5~7	50~200
J_c at 4.2 K (A/cm ²)	~10 ⁶	~10 ⁶	~10 ⁶	~10 ⁶	~10 ⁷
H_{c2} at 4.2 K (T)	11–12	25–29	15–20	>100	>100
H_{irr} at 4.2K (T)	10~11	21~24	6~12	5~7(77K)	0.2(77K)
Coherence length $\xi(0)$ (nm)	4~5	3	4~5	1.5	1.5
Penetration depth $\lambda(0)$ (nm)	240	65	100~140	150	150
Resistivity $\rho(T_c)$ ($\mu\Omega\text{cm}$)	60	5	0.4	150~800	40~60

1.2.3 The phase diagram of MgB₂

Phase diagram is an important guide for the fabrication, composition selection and application of materials and chemical products. As shown in Figure 1-7, the temperature-composition phase diagrams for Mg-B system at ambient pressure is plotted ^[21]. The labels Solid, Liquid and Gas represent the Mg-rich solid, liquid and gas phases, respectively. From the figure we can see that when the temperature is higher than 650 °C and the atomic Mg:B ratio is greater than 1:2, Mg is melt and coexists with MgB₂ solid. If $1:4 < \text{Mg:B} < 1:2$ and the temperature is below 1090 °C, MgB₂ coexists with MgB₄. There are large composition windows in which Mg liquid and MgB₂ coexist.

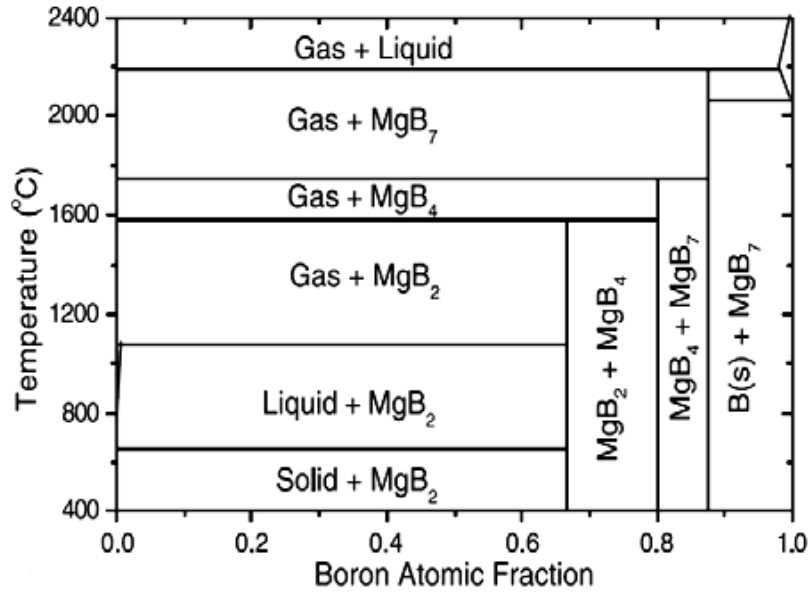


Figure 1-7 Phase diagrams of the Mg-B system under the Mg vapor pressure of 1atm.

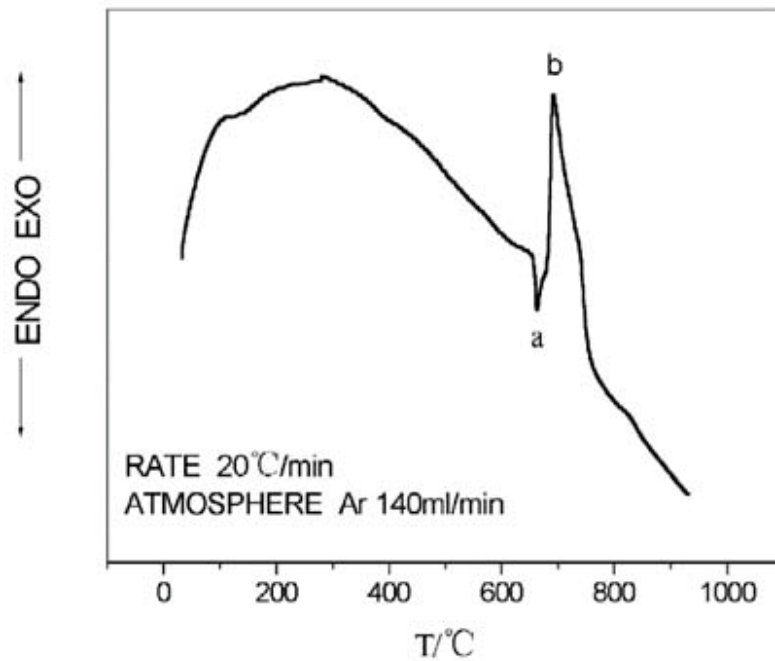


Figure 1-8 DTA curve of Mg:B = 1:2 mixture ^[22]

Figure 1-8 shows the phase formation process with Differential Thermal Analysis (DTA) measurement. The two peaks in the DTA curve represent the two reactions as following,





s and l in above equation represent for the solid phase and liquid phase, respectively. Reaction (a) suggests that the solid state Mg becomes liquid state, while Reaction (b) shows the formation of MgB_2 phase. It is clear that the reaction of MgB_2 (b) appears just following with the melting Mg (a), and this reaction progress is very fast. The vapor pressure at Mg melting point 650°C is only 135 Pa, which implies that the evaporation of Mg at this temperature is very less. This liquid-solid reaction between Mg and B will improve the density of MgB_2 .

1.3 Element and compound doping of MgB_2

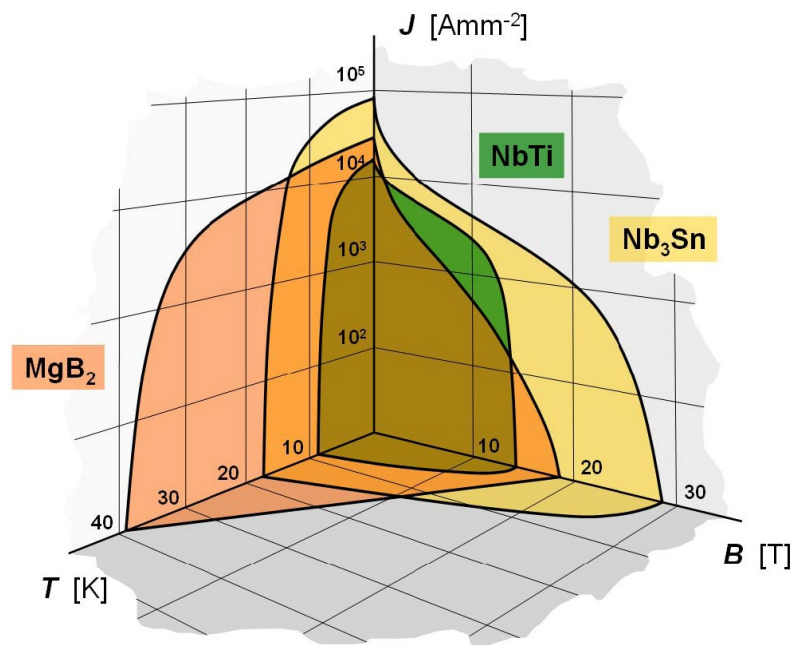


Figure 1-9 Critical surfaces of MgB_2 , NbTi and Nb_3Sn [23]

In self field, the transport current densities J_c of pure MgB_2 is around 10^6 A cm^{-2} in the bulks, films, wires and tapes, even at temperatures of 20-25 K. Figure 1-9 shows the relationship among T_c , J_c and H_c for MgB_2 , NbTi and Nb_3Sn , respectively. It can be seen that the J_c value of pristine MgB_2 drops rapidly with the increasing the external magnetic field due to its poor flux pinning strength in magnetic field and low upper critical field (H_{c2}).

Enhanced J_c - B and flux pinning of MgB_2 have been attempted using several of techniques, including irradiation [24]-[26], chemical doping [27]-[30], magnetic field

annealing^{[31], [32]} and ball-milling methods^{[33]-[35]}, *etc.* Compared to other techniques, chemical doping was thought as a convenient and effective method to enhance the J_c - B properties of MgB_2 . The electronic state, lattice constants and crystallinity are expected to be changed by chemical doping. On the other hand, impurity particles are expected to perform as effective pinning sites if their grain size is moderately small and they are dispersed throughout the MgB_2 matrix. Another expected effect of doping is the suppression of the grain growth of MgB_2 .

1.3.1 Metallic element doping

There are many elements that form metal diborides into the AlB_2 -type structure. The effects of partial substitution at Mg sites in MgB_2 with other metals have been reported for several elements such as Al^{[36]-[38]}, Ti^{[39]-[42]}, Zr^{[40], [43], [44]}, Zn^{[45]-[46]}, Sn^[47], Fe^{[48], [49]}, La^{[50]-[51]}, Li^{[52]-[54]}, *etc.* Among these so many metallic dopants, Al, Ti and Zr were found to be effective in improving the critical current properties^{[36]-[44]}. Unexpectedly, Ti and Zr can not get into the MgB_2 lattice but form thin layers of TiB_2 or ZrB_2 less than 1 nm thick, resulting in the very fine MgB_2 grains with the diameter of ~ 10 nm and dense microstructures including fine MgO particles. Corresponding to the dramatic change in the microstructure, Ti- or Zr-doped MgB_2 bulk shows dramatically improved J_c , particularly under low magnetic fields. J_c is higher for Ti-doped samples and the sample with a nominal composition of $\text{Mg}_{0.9}\text{Ti}_{0.1}\text{B}_2$ exhibits the highest J_c for bulk of $1.3 \times 10^6 \text{ A cm}^{-2}$ at 20 K under self-field. However, H_{irr} is not high even when compared with undoped MgB_2 bulk, ~ 70 kOe at 5 K and ~ 40 kOe at 20 K.

Although Al substitution at Mg site dramatically decreases T_c of MgB_2 due to the decrease of the hole carrier concentration, J_c under low magnetic fields is enhanced by 20~30% when the doping content is $\sim 0.5\%$ at Mg site. In this case, local weak superconducting regions around Al ions are considered to act as effective pinning sites. Similar dilute substitution effects are also found in cuprate superconductors^[36].

1.3.2 Non-metallic element doping

Partial element substitution at B site has more significant effects on the superconducting properties of MgB_2 , because superconductivity appears at the honeycomb B lattice. Substitution effects at B site of MgB_2 have been reported for Si

[55], C [56]-[58], O [59], and Be [60], all of which are found to essentially decrease T_c . However, C substitution effects have been eagerly studied to clarify the superconductivity mechanism and the improvement of critical current properties.

Although there are numerous systematic studies on the relationship between the C substitution content and various physical properties of MgB_2 with different type of carbon source, such as amorphous C [61], graphite [62], C60 [63], nano diamond [64] and carbon nanotubes (CNT) [65]-[67], *etc*, many inconsistencies concerning structural parameters and superconducting properties can be found. This problem originates from the difference in the C substitution content between nominal composition and the actual content in the resulting samples. In the case of single crystal growth at high temperatures of 1600~1700 °C, the C substitution content is almost identical to the nominal one, while the actual C substitution content is usually much lower for polycrystalline bulk, even when they are heat treated at high temperatures above 1000 °C. Because C contains impurity phases, such as original C, MgB_2C_2 and Mg_2C_3 often remain in the C-substituted MgB_2 bulk, resulting in a decrease in the actual C content in MgB_2 .

The original high T_c of MgB_2 decreases dramatically with increasing C substitution content at B site, ~30 and ~ 2.5 K for 5 and 12.5%, respectively. The temperature dependence of H_{c2} is steeper for C-substituted MgB_2 bulk, therefore, a small amount of C substitution into MgB_2 leads to higher H_{c2} at low temperatures. Corresponding to the enhancement of H_{c2} at low temperatures, J_c values under high fields and H_{irr} below 20 K are higher for C-substituted MgB_2 bulk with moderate C concentrations than those of undoped bulk. This means that the pinning force in MgB_2 polycrystalline bulk is somehow enhanced when coherence length is shortened. Since the enhancement of H_{irr} is also observed for C substituted single crystals, intragrain pinning is essentially improved by incorporating C.

For O substitution, unintentionally O-added thin films have attracted great interest due to their extremely high H_{c2} at low temperatures and improved J_c under high fields even at 20 K, although T_c is greatly lowered to ~30 K. In the case of MgB_2 bulk, intentional substitution of O had been believed to be difficult, because O preferentially forms MgO and B_2O_3 during the high temperature heat treatment. However, several groups pointed out that small $\text{Mg}(\text{B},\text{O})_2$ regions are generated in the

MgB₂ crystals, which suggests that O can substitute at B site even in a bulk specimen. Recently, O was found to dissolve into MgB₂ bulk resulting in the improved H_{c2} , H_{irr} and J_c , when the bulk was synthesized at low temperatures below 700 °C, similar as in the case of thin films, Partial substitution with Si is also reported to be effective for improving the critical current properties under high fields.

It should be noted that the substitutions with C, O or Si at B site are effective for improving critical current properties only under high magnetic fields, and J_c in low fields are usually lower than that of undoped MgB₂. On the contrary, as described above, substitutions of Ti, Zr or Al at Mg site are effective in enhancing J_c only under low fields.

1.3.3 Compound doping

The improvement of critical current properties of MgB₂ has been also attempted by doping various compounds such as SiC [67]-[69], B₄C [70], [71], hydrocarbons [72], carbohydrates [73], *etc*, among which SiC fine powder is well known as one of the most effective dopants for improving H_{irr} and J_c . A 10 wt % SiC-doped MgB₂ bulk showed $H_{irr} \sim 80$ kOe and $J_c \sim 10^5$ A cm⁻² under 30 kOe at 20 K, while its density was almost half the theoretical value. These are the highest values obtained for MgB₂ bulk at the present stage and are almost comparable to those of commercial Bi(Pb)2223/Ag sheathed tapes. In the SiC-doped MgB₂ bulk, both Si and C are considered to contribute to the enhancement of H_{irr} and J_c by substituting at B site. In addition, J_c under low fields has not been lowered by SiC doping. Highly dense dislocations and fine inclusions of Mg₂Si ~10 nm in size and unreacted SiC observed in the microstructure are believed to be attributed to the enhancement of J_c even under low fields. Recently, by SiC-doped MgB₂ tapes exhibited high H_{irr} of up to 230 kOe at 4.2 K, suggesting the possibility of practical applications for high magnetic field generation at the liquid He temperature.

Other effective dopants for the enhancement of J_c are fine powders of Y₂O₃ [74], SiO₂ [75] and metal carbonates [76], such as Li₂CO₃, Na₂CO₃ and Mg₂CO₃. For Y₂O₃-doped MgB₂ bulk, very small YB₄ particles of 3~5 nm formed in MgB₂ grains are observed as effective pinning centers. In the case of metal-carbonate-doped MgB₂ bulk, C and O are considered to substitute at B site, resulting in the enhancement of J_c under high magnetic fields.

An additional advantage of compound doping is the high reactivity at low temperatures. Although substitution with C is known to be effective for improving J_c under high fields, the reaction of C into $Mg(B,C)_2$ is nominal during low-temperature heating below 650 °C, which is a desirable condition for enhancing both H_{irr} and J_c . On the other hand, C substitution at B site in MgB_2 can also be obtained with low-temperature processing using SiC or B_4C as starting materials. A similar tendency is found for O substitution using B_2O_3 as a starting reagent.

1.4 The fabrication method of MgB_2 superconducting wires

Since the discovery of superconductivity in MgB_2 in 2001, conductor development has progressed to where MgB_2 superconductor wires in kilometer long lengths have been demonstrated in magnets and coils. Currently, works have been started and are in-progress on demonstrating MgB_2 wire in superconducting devices for which the wires are also available commercially.

1.4.1 Mg infiltration method

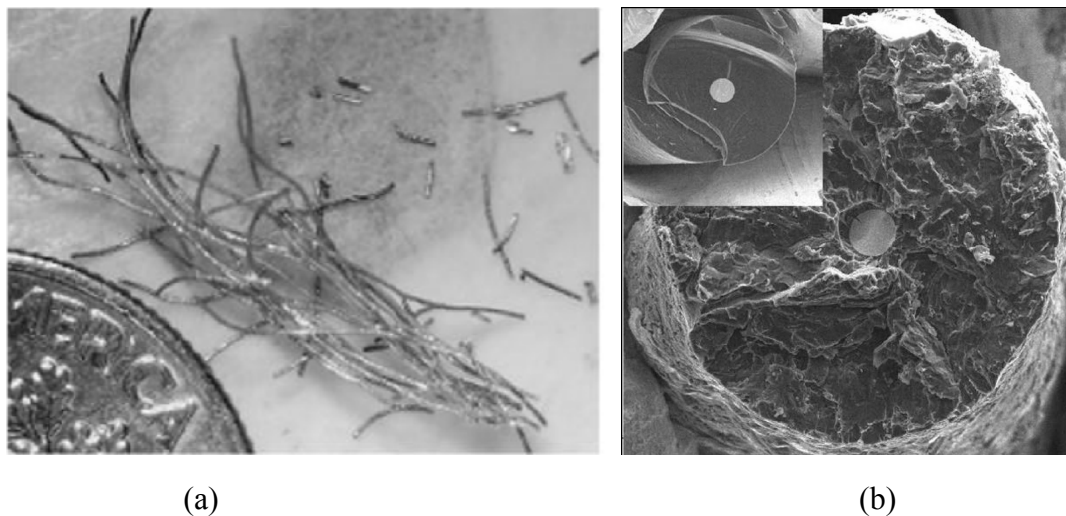


Figure 1-10 MgB_2 wire fabricated by Mg infiltration method ^[77]

Only several months after the discovery of superconductivity in MgB_2 , the first MgB_2 wires were prepared by Canfield *et al* ^[77]. Tungsten reinforced boron fibers with 100 μm in diameter were exposed to magnesium vapor at 950 °C for 2 hours in a sealed Ta tube. The resulting MgB_2 wires with the diameter of 160 μm exhibited very high density and purity. The macroscopical photograph and electron microscope image of the cross section of these grown MgB_2 wires are shown in Figure 1-10.

Figure 1-10 (b) is the electron microscope image of the unreacted boron filament. The central core of tungsten wire with diameter of 15 μm can be clearly seen. This MgB_2 wire has been measured with J_c value of 10^5 A/cm^2 at 4.2 K. This method is similar to the coated conductor route or the liquid infiltration technique. It also succeeded in the fabrication of short tapes, but the applicability to long lengths wires has not been demonstrated.

1.4.2 Powder-in-tube technology

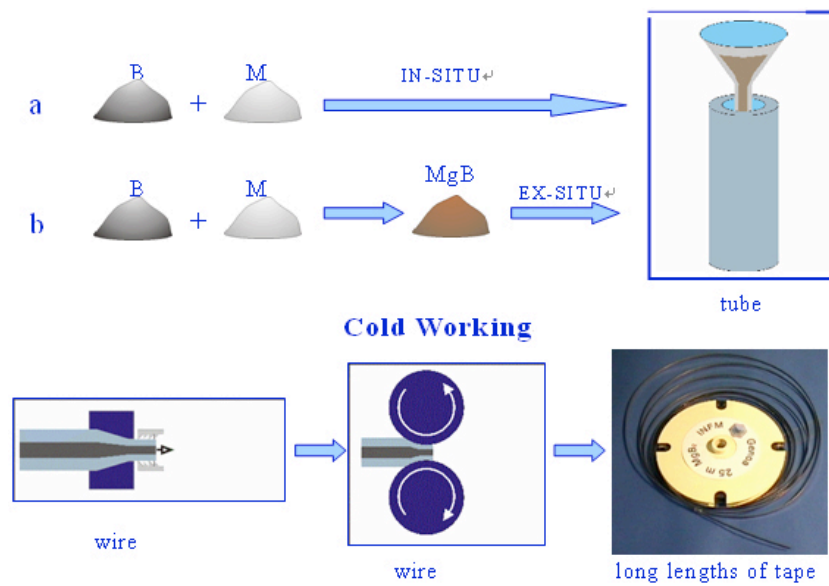


Figure 1-11 Schematic diagram of the Powder in tube process (PIT)

A very convenient method, powder-in-tube (PIT) technique, which has been used to fabricate the HTS BSCCO-conductors widely, was using to produce MgB_2 wires and tapes with industrial lengths in a large number of laboratories^{[72], [78], [79]}. The key advantages for PIT process are the low cost and simple fabrication process. Moreover, it is very mature and stable technique for fabricating multi-filamentary structure superconducting wires and tapes, which usually exhibited better current-carrying and mechanical properties than mono-filamentary wires or tapes, due to the smaller size for each filament. Multi-filamentary wires and tapes also can resist larger tensility and bending strains than mono-filaments; multi-filamentary wires and tapes show a higher thermal stability, due to the smaller dimension filaments. However, one of the primary issues while producing industrial MgB_2 wires and tapes by the PIT process is the hardness and brittleness of the MgB_2 . Especially, drawing or rolling the

multi-filamentary MgB₂ wires or tapes into small size is a very hard work. Therefore, in the practical high current MgB₂ multi-filamentary wires and tapes, the filaments size is around 30 μm^[80], much larger than those in Nb₃Sn wires. Two methods including *in-situ* and *ex-situ* PIT have been reported in the literature. The fabrication process is shown in Figure 1-11.

1.4.2.1 *In-situ* PIT technique

In-situ PIT technique consists of filling the metallic tubes with elemental Mg and B powders subsequent deformation and heat treatment. In this case, much lower heat treatment temperatures are sufficient to achieve high critical current densities which extend the choice of applicable sheath materials. The major impurity in both *in-situ* and *ex-situ* precursor routes is MgO formed by the oxidation of Mg with the content up to ~1%. For the *in-situ* route, Boron rich phases also are presented due to the insufficiently reacted precursor.

The advantages of the *in situ* process are simplicity of fabrication, lower reaction temperatures, and increased ease in adding dopants or other additives into the wire. The lower reaction temperature is particularly important as it helps to minimize the possibility of powder-barrier reactions. The overlap-closed filled tube must be chemically compatible with the powders at the MgB₂ reaction temperature.

1.4.2.2 *Ex-situ* PIT technique

Another fabrication route is the *ex-situ* PIT technique, which consists of direct filling of the metallic tubes with reacted MgB₂ powders, followed by cold deformation. Heat treatment at 600-1000 °C is usually applied to the cold-worked tapes or wires to obtain superconductivity for an improved core density with well connected grains. The high annealing temperature, however, reduced the choices of sheath materials, because the chemical reactions between the sheath and filament have to be avoided in future multi-filamentary wires with much smaller filament dimensions. The thickness of the reaction layer is typically in the range of 1-25 μm depending on the used sheath and applied heat treatment temperature.

1.4.3 The Continuous Tube Forming and Filling process

Another technique was so-called continuous tube filling/forming (CTFF) process

[81]. During the CTFF process, powders are dispensed onto a strip of metal as it is being continuously formed into a tube. Figure 1-12 shows a conceptual schematic diagram of this process. Wire begins with a metal strip made of Nb, which is formed into a tube after being filled continuously with powder. Then the whole Nb tube with powders is put into another tube made of Monel. After double sheathed the tube is ready for drawing. Historically, all other manufacturers of superconductor wires use a batch process, which involves filling tubes of a fixed length with powder. This requires much larger tubes to obtain longer lengths of wire. This traditional method also involves more wire processing (drawing or extrusion) and thus incurs high manufacturing costs.

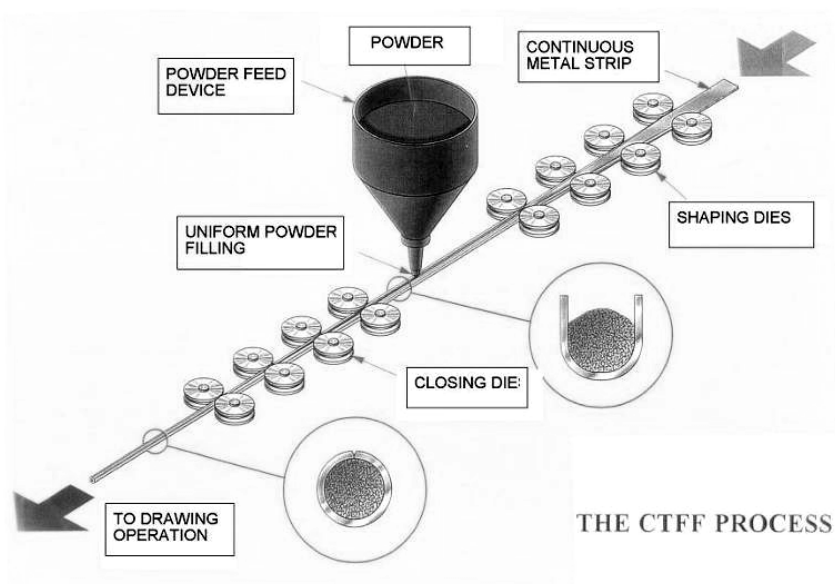


Figure 1-12 Sketch map of Continuous Tube Filling and Forming (CTFF) process

1.4.4 The Internal Magnesium Diffusion method

Hur *et al.* [82] and Giunchi *et al.* [83] succeeded in the fabrication of high- J_c MgB₂/Fe wires by applying the internal Mg diffusion (IMD) process (as shown in Figure 1-13) with a pure Mg core and SiC addition. According to the IMD process, a pure Mg rod with a 2 mm diameter was positioned at the center of a Fe tube, and the gap between the Mg and the Fe tube was filled with B powders or powder mixtures of B-(5mol%) SiC. The composite was cold worked into 1.2 mm diameter wire and finally heat treated at temperatures above the melting point of Mg (~650 °C).

Throughout the heat treatment, the liquid Mg infiltrated into the B layer and reacted with B to form MgB_2 .

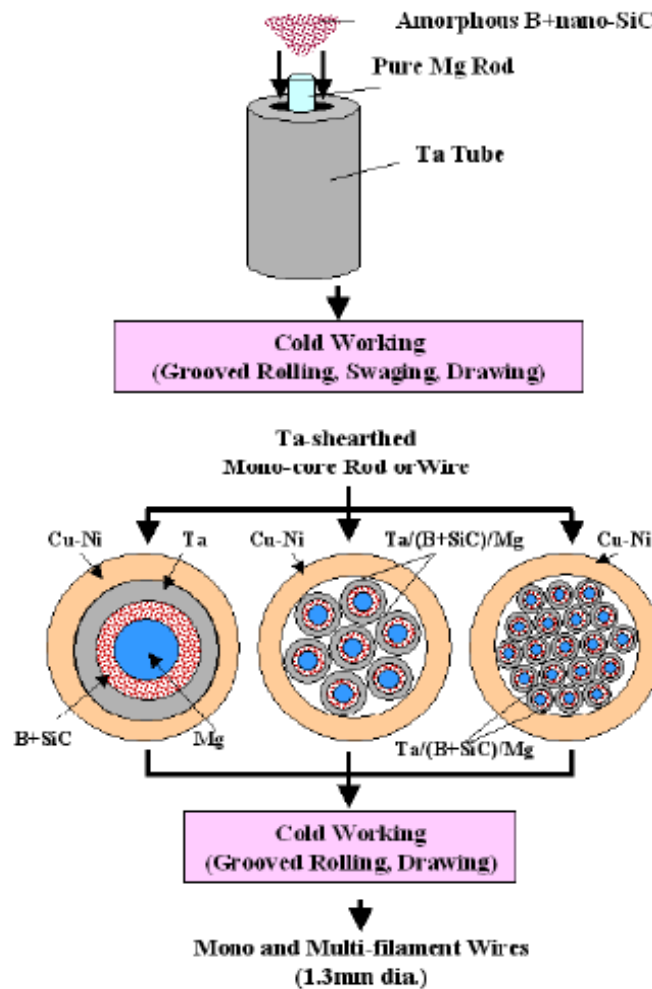


Figure 1-13 Schematic diagram of the Internal Magnesium Diffusion process (IMD)

1.4.5 The sheath materials

Practical superconductors consist with several filaments of superconducting material embedded in a highly conducting matrix. The compound wires are usually reduced in size by drawing, rolling or extrusion process. This is a simple and feasible process for flexible alloys, like Nb-Ti superconductor. However, MgB_2 is a hard and brittle intermetallic compound similar to Nb_3Sn and BSCCO, which is more difficult to deform directly.

The powder-in-tube (PIT) process is adopted for fabricating these brittle superconducting materials by using a suitable sheath material. The resulting wire is

not as flexible as conventional metal wire, but is sufficient for many applications. In this process, the sheath material plays a crucial role. High thermal conductivity and electrical conductivity metal, Ag and Cu was adopted for fabrication the Nb₃Sn and BSCCO. But for Mg-B mixed powders, this matrix metal is not a proper choice, due to the higher chemical reactivity of Mg and B which will react with many metals such as Ag, Cu, Al *etc.*, and form an obvious reaction layer between the superconducting core and sheath material during the intermediate or final annealing. Usually, this reaction layers will decrease the superconducting properties or damage the thermal stability of the MgB₂ wires. Therefore, this reaction layer should be avoided or reduced by using the proper sheath material.

Generally principles for sheath material choice as following:

- (1) chemical stability;
- (2) outstanding plasticity;
- (3) higher thermal conductivity and electrical conductivity;
- (4) lower material cost.

Various metal materials such as Ni^{[84], [85]}, Cu^{[86]-[88]}, Fe^{[89]-[90]}, Nb^{[91], [92]}, Ta^[91], Stainless Steel (SS)^{[93], [94]}, *etc.* have been employed as the sheath materials of MgB₂ wires in different teams. In order to increase the mechanical strength of the MgB₂ wires, a variety of composite sheath are also used, such as the Cu/Ta, Cu-Ni, Fe/SS, Fe/Ni, Fe/Cu, *etc.*^{[95]-[99]}. Considering all the factors mentioned above, Fe, Nb and Cu are the ideal sheath materials for fabrication of MgB₂ wire. Fe sheath offers much lower cost and enough mechanical strength, and Nb is not easy to react with Mg or B. Certainly, Cu combines the low cost and well thermal stability.

1.5 Long length MgB₂ wires and tapes fabrication

There are several companies which can fabricate MgB₂ wires and tapes presently. Columbus Superconductors has fabricated the first kilometer level long length MgB₂ tapes up to 1.6 km in 2006^[100]. The tapes had been fabricated with *ex situ* powder-in-tube method. In such a process, fully reacted MgB₂ powders were packed into pure nickel tubes, which were cold worked in order to manufacture a long wire. Such a monofilament wire was cut into several pieces and stacked again inside the

second nickel tube, which also included an inner oxygen free high conductivity copper core (OFHC) and an iron diffusion barrier in order to prevent diffusion of copper to nickel and MgB_2 during heat treatment. The composite was cold worked again by drawing and rolling to achieve the final rectangular shape of the tape. The typical thickness and width of the manufactured tapes were 0.65 mm and 3.65 mm, respectively. The final heat treatment at high temperature (900 °C) was applied to sinter the MgB_2 grains and achieve the high critical current density. A typical transverse cross section of the MgB_2 conductor after the final heat treatment is shown in Figure 1-14.^[101]

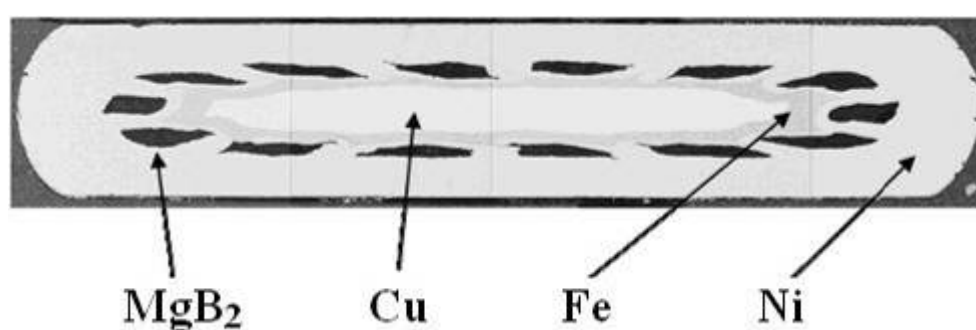


Figure 1-14 Transverse cross section of the MgB_2 superconducting tape fabricated by Columbus Superconductors

Hyper Tech Research, Inc., (Hyper Tech) using the continuous tube filling and forming (CTFF) process fabricate the multifilament MgB_2 wire. In general, Nb barrier is enclosed in an outer sheath, to aid the wire drawing and eventually to provide electrical stabilization. For most of wires made at Hyper Tech, the overlap closed niobium strand is inserted into a seamless copper (or copper alloy) tube and is drawn to a predetermined size, creating a monofilament MgB_2 strand. The monofilament strands are then restacked into another seamless tube; the diameter and length of this restack tube will determine the final length of the wire. Billets are currently being sized to produce continuous wire lengths of 5 km for a typical 0.8 mm diameter wire.

The commercial wire currently fabricated at Hyper Tech is a multifilament strand constructed with 18 monofilaments (Nb barrier, Cu sheath) and one center copper filament restacked in Monel. The designation of this standard multifilament is 18+1 Nb/Cu/Monel. Figure 1-15 shows a typical wire cross section. A number of experimental strands have been fabricated for various projects. For the purpose of

increasing the ductility and stability of the strand (and increasing the copper to superconductor ratio), the Monel outer restack sheath is replaced with pure 101 copper or oxide-dispersion strengthened (ODS) copper, trade name Glidcop™. ODS Cu offers the benefits of lower resistivity without sacrificing a significant degree of strength needed for drawing. Strands with high filament counts and very small diameters also have been made. Hyper Tech has fabricated the Nb/Cu/Monel MgB₂ superconductor wires with up to 61 total filaments. The smallest MgB₂ superconductor strands made were 0.07 mm round for monofilament and a 0.117 mm round for 7 filament Nb/Cu/Monel wire. The size of MgB₂ filament in the 0.117 mm 7 filament-restack strand was 17 μm. MgB₂ filament in the standard 18 + 1 multifilament wire at 0.8 mm is 76 μm. Finally, experimental MgB₂ superconductor wires have been fabricated in a rectangular- shape with a 0.5×1.0 mm aspect ratio in various multifilament strand designs. [102]

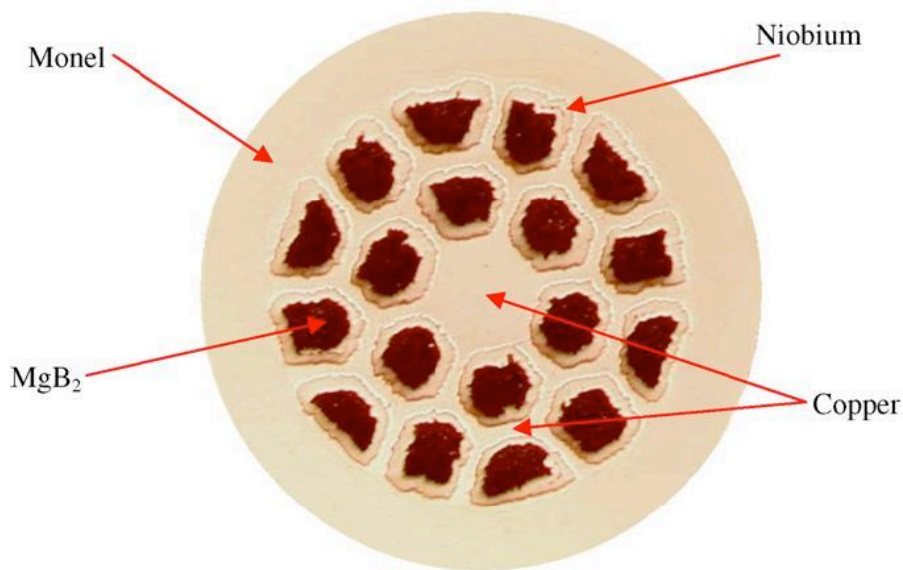


Figure 1-15 Cross section of typical 18+1 multifilament MgB₂ wire fabricated by Hyper Tech Research

1.6 The typical application of MgB₂ superconductor

In general, the application range for MgB₂ superconductor is in two main regions: the “low field” applications using cryogenic free systems and able to work in a temperature range around 20 K, and the “high field” region, where the conductor could be used as NbTi at 4.2 K but at magnetic fields potentially higher than those currently reachable with this material (around 8 T at 4.2 K).

ASG started to design an MRI magnet based on MgB_2 conductors well in advanced compared with the expected industrialization of the conductor (Figure 1-16)^[103]. The design was changed to follow the evolution of the conductors during the engineering study. On the other hand, this work provide the possibility to start winding the first double pancake and composing the magnet, just few weeks after the production of the cable in its first real and usable length. The magnet was finally assembled and the tests were already started with positive results.

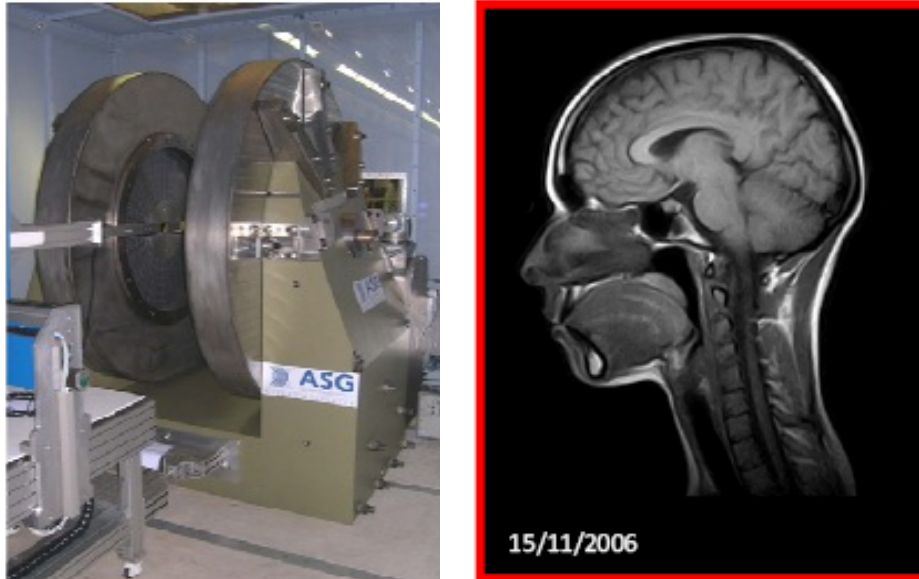


Figure 1-16 MgB_2 -based, cryogenic free, open MRI magnet as delivered from ASG Superconductors to Paramed (left) and first brain image acquired by Paramed Medical Systems on the MR-Open system (right)^[103]

The preliminary results confirmed that the 18 km of conductor used to wind the coils are satisfying the requirements of the MRI system. The magnet reached its nominal current of 90 A and the central field of 0.5 T without any training. The 12 double pancakes are electrically connected to each other in series with optimized but still resistive joints, as the superconducting joint technology had not yet been successfully developed in ASG at that time. Plan for this product is to put it on the MRI market as soon as the tests and the full industrialization are successfully completed. When this happens, the first large scale commercial application of magnesium diboride superconductor will be out on the market. It will give the Columbus' factory a continuous production rate for the conductors which would help to reduce its production cost.

Recent years, several MgB₂ Fault Current Limiter (FCL) prototypes were built in the framework of the LIMSAT Italian project, for the development of FCL coordinated by CESI ^[104]. The test results of them were in agreement with what expected from the transport properties of the conductor: the non inductive winding has reached a critical current in the order of 600 A. These non inductive windings were tested with AC transport currents both in LHe and in Liquid Neon at different frequencies (from 2–500 Hz) and different peak to peak currents, up to the several times the I_c .

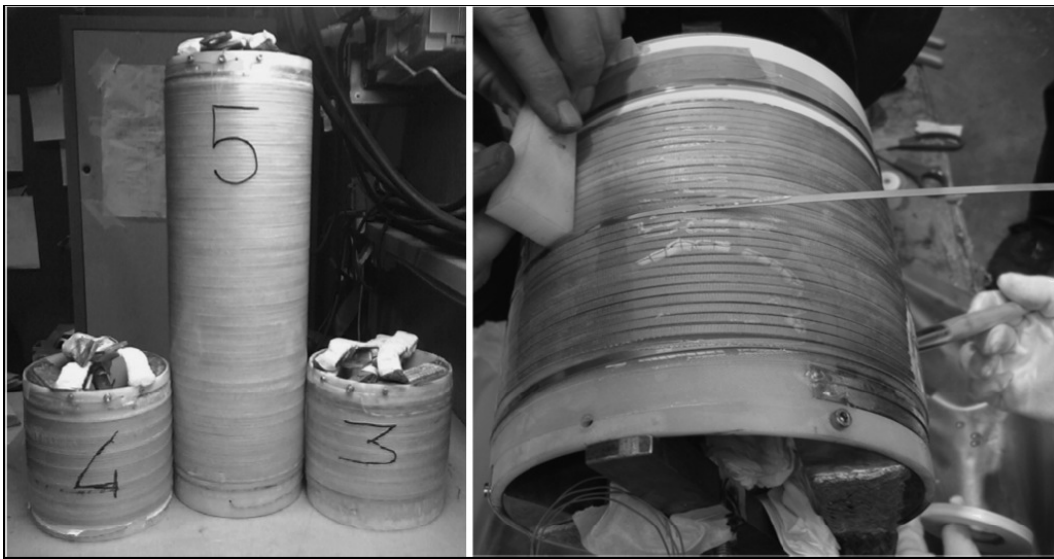


Figure 1-17 Photograph of MgB₂ SFCL prototypes (left) and detail of electrical connections (right)^[104]

Several prototype solenoids were realized with different conductors and various winding techniques, yielding a central magnetic field up to 5 T. The possibility to wind an already reacted conductor in a relative small diameter without any degradation is demonstrated with the test of one solenoid R&W magnet wound on 135 mm ID. The solenoid made with 500 m of multi filamentary tapes reached the short sample limit at 20 K without any training. And such a magnet reached a central field of 1 T at an operating temperature of 16 K.

1.7 Motivation

According to a new technical market research report, Superconductors: Technologies and Global Markets, the global market value for superconductors was

estimated \$2 billion in 2010, and is expected to increase to nearly \$3.4 billion in 2015 [105]. MRI devices constituted an important role of that figure, whereas the share of conventional low temperature superconductors was almost 99%. Currently, about 150 000 km of conductor is manufactured yearly from NbTi. The biggest MgB₂ conductor supplier, Columbus Superconductors, produced 1 000 km of MgB₂ wire in 2010. This is still a small market, e.g., Columbus Superconductors aims to grow twice their production each year for the next three years. They also estimate that with production capacity reaching 10 000 km/year, the price becomes comparable to that of NbTi.

Due to high superconducting transition temperature T_c , weak-link free grain coupling and low raw material cost, MgB₂-based superconducting materials have been a strong competitor for electric power and magnet applications at temperatures around 20 K, especially for magnetic resonance imaging (MRI) magnet which prefers to work at cryogen-free circumstances. However, the above application brings some rigorous requirement on mechanical, electrical, and superconducting properties of MgB₂ wires as well as the thermal stability.

For those applications, an important foundation is to fabricate the high performance MgB₂ wires and tapes. The main purpose of this work is to optimize the superconducting properties and performances by optimizing three key factors, heat treatment process, element doping, and wire composite design. At the same time, microstructures, microchemistry and superconductivity are investigated in order to find some basic theoretical general rules for *in-situ* MgB₂ superconductors.

1.8 Thesis arrangement

This thesis is organized into six chapters.

Chapter 1 is a brief introduction of the background of this work. The characteristic, fabrication technique, and superconductivity of MgB₂ materials were reviewed. The motivation and aims are outlined, and the organization of this thesis is presented in this part.

Chapter 2 describes the wires design, fabrication process of both mono-filamentary and multi-filamentary MgB₂/Nb/Cu wires and tapes by *in-situ* PIT technique. Then the characterization methods and techniques was described, including X-ray diffraction (XRD), scanning electron microscope (SEM), Superconductivity

Quantum Interference Device (SQUID), transport critical current measurement, resistivity measurement, and magneto-optical image (MOI).

Chapter 3 studies the effect of heat treatment temperatures on mono-filamentary MgB₂/Nb/Cu wires. The phase formation processes, microstructures, superconductivity, as well as the diffusion layer between Nb and MgB₂ core were studied respectively.

Chapter 4 researches the effect of carbon doping on MgB₂/Nb/Cu mono-filamentary wires. The effect of both TiC and C doping on the lattice parameters a and c , critical transition temperature (T_c), critical current density (J_c) and magnetic flux pinning in MgB₂ was systematically investigated within a wide range of processing conditions. It was found that substitution of B for C enhances the flux pinning but depresses T_c slightly. By controlling the processing parameters, an optimized $J_c(H)$ performance is achieved under a partial amorphous C substitution.

In Chapter 5, Cu-clad 6-, 12-, and 36- filamentary MgB₂ wires with Nb buffer layer have been fabricated with *in-situ* PIT method. To improve the strength of wires, the Nb-core was used as the central filament. The stress-strain, bending properties, microstructures, and superconductivity properties were analyzed, respectively.

Chapter 6 is the summary of this thesis.

CHAPTER 2

FABRICATION AND ANALYSIS WAY OF MgB₂ WIRES

In this Chapter, the conductor design, fabrication process of mono-filamentary and multi-filamentary MgB₂/Nb/Cu wires and tapes by *in-situ* PIT technique was described. Then the examination methods and techniques was introduced, including X-ray diffraction (XRD), scanning electron microscope (SEM), Superconductivity Quantum Interference Device (SQUID), transport critical current measurement, resistivity measurement, and magneto-optical image (MOI).

2.1 Fabrication process of MgB₂ wires

2.1.1 Conductor design

In order to make MgB₂ wires achieve the requirement of mechanical strength for magnet application, the superconducting wires employ the conductor structure with the center Nb rod-reinforcement, and Cu tube as the stability materials to transmit the thermal energy. For avoiding the reaction of Mg and Cu, Nb barrier layer with enough thickness is also used. The cross section areas of the Nb rod and outer Cu tube can be adjusted to obtain a necessary MgB₂/Nb/Cu ratio. Four typical cross section MgB₂ wires with mono, 6-, 12-, and 36- filament, respectively, are designed.

2.1.2 Fabrication of mono- and multi-filamentary MgB₂ wires

MgB₂/Nb/Cu monofilament wire was fabricated by *in-situ* PIT process. Mg (325 mesh, 99%), B (sub-micron, 99%) and amorphous carbon (sub-micron, 99%) were used as precursor powders. These powders were mixed with a premeditated ratio and grounded in agate mortar for 30 minutes in vacuum glove box at argon atmosphere. The precursor powders were filled into Nb/Cu composite tubes, and the filled composite tube was then drawn to an appropriate size in diameter and rebuilt in the Cu tube with 6-, 12-, and 36- filament. Due to the perfect ductibility of Nb/Cu composite tube, there is no annealing needed during the cold-deformation process. After that, the composite wires were cut and sintered at various temperatures from 600 to 950 °C for 2 hours in flowing argon, respectively, then furnace-cooled to room

temperature. The fabrication process is shown in Figure 2-1.

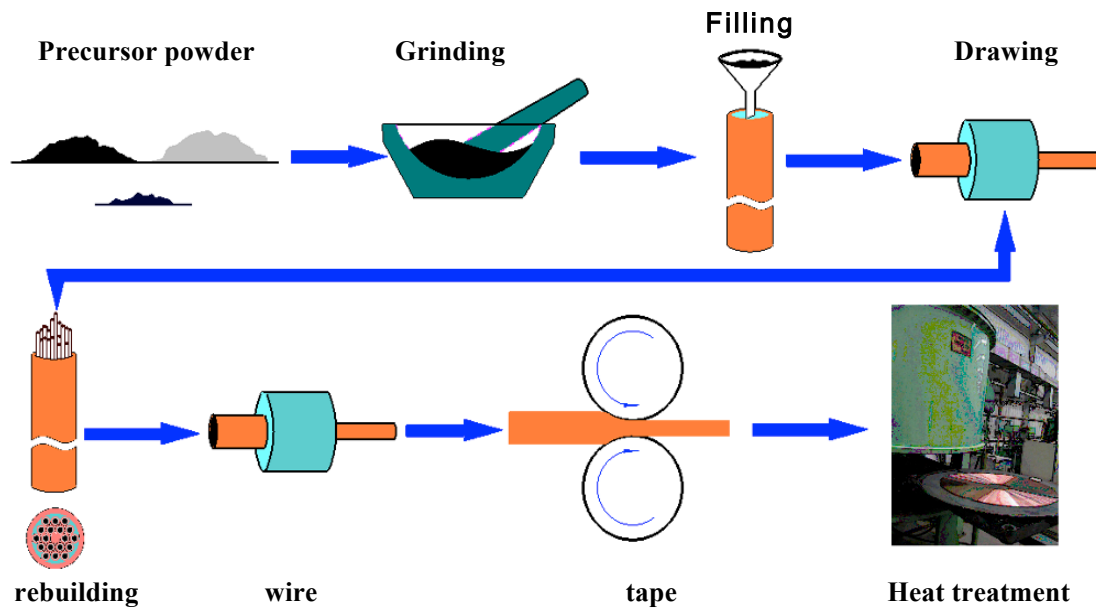


Figure 2-1 Schematics of the *in-situ* PIT process for the fabrication of multi-filamentary MgB₂/Nb/Cu wires and tapes

2.1.3 Heat treatment process

The filled and drawn wires of 50 mm in length were annealed for 2 hours at different temperatures ranging from 600 °C to 950 °C. Heat treatment was performed under Ar gas flowing at ambient pressure using a horizontal electric hinged furnace (Thermo Electron Corporation Lindberg/Blue M).

The hinged furnace has the maximum temperature limit of 1200 °C. The annealing system used in this experiment is composed of a power supply, which has the voltage ranges between 208/240 V and 30 A input. Regarding the working principle of this system, it is important to decide the set point of the temperature. After deciding the annealing process temperature, the system was set to the desired temperature for heating up. After the temperature was stabilized, the system was left 5 to 10 minutes. Then, the furnace was set to the desired temperature for suitable time and then cooled down to the room temperature. The most essential step here was to utilize a rapid cooling process. A temperature profile for the annealing of MgB₂ wires is shown in the Figure 2-2.

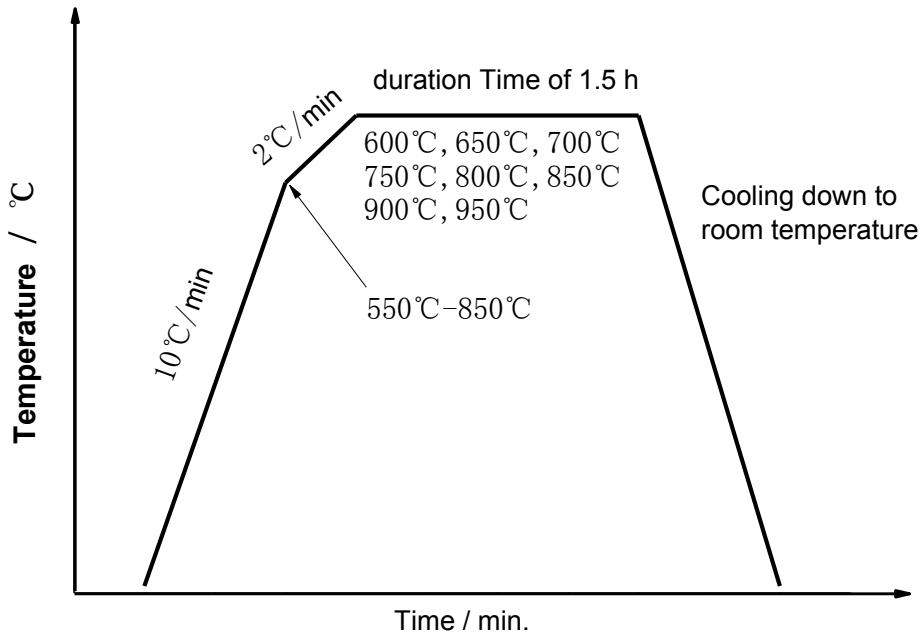


Figure 2-2 A temperature profile for the annealing of MgB₂ wires

2.2 Phase formation analysis

The X-Ray diffraction is most useful for qualitative rather than quantitative analysis (although it can be used for both) of powders, single crystals and thin films. We can use it to identify phases, and to measure crystal lattice parameters, residual stress, texture, and crystalline size of nano-materials. The most commonly used X-ray radiation is that emitted by copper, whose characteristic wavelength ($K\alpha$) for the radiation is $\lambda = 1.5406 \text{ \AA}$.

For powder X-ray diffraction, well grounded powders of the samples were placed onto a sample holder of the diffractometer equipped with Cu $K\alpha$ radiation. Data were collected from $2\theta = 20^\circ$ to 80° with a constant scan speed of $0.02^\circ/\text{step}$ per 10 seconds at room temperature. When the incident beam strikes the powder sample, diffraction occurs in every possible orientation of 2θ . The diffracted beam may be detected by using a moveable detector such as a Geiger counter, which is connected to a chart recorder. In normal use, the counter is set to scan over a range of 2θ values at a constant angular velocity. Routinely, a 2θ range of 20° to 80° is sufficient to cover the most useful part of the powder pattern. In this work, XRD measurements were carried out using the Powder Diffractometer in the Consortium de Recherche pour l'Emergence de Technologies Avancées (CRETA) Grenoble and in Analysis Center

for Materials Research (ACMR) in Northwest Institute for Nonferrous Metal Research Group (NIN), to perform the X-ray diffraction properties of MgB₂ wires.

2.3 Microstructure observation

2.3.1 Scanning Electron Microscope Analysis

Scanning Electron Microscope (SEM) is a type of electron microscope that images a sample by scanning it with high-energy beam of electrons in a raster scan pattern. The electrons interact with the atoms that make up the sample producing signals that contain information about the sample's surface topography, composition, and other properties such as electrical conductivity. The types of signals produced by SEM include secondary electrons, back-scattered electrons (BSE), characteristic X-rays, specimen current and transmitted electrons. The Schematic diagram of an SEM is showed in Figure 2-3.

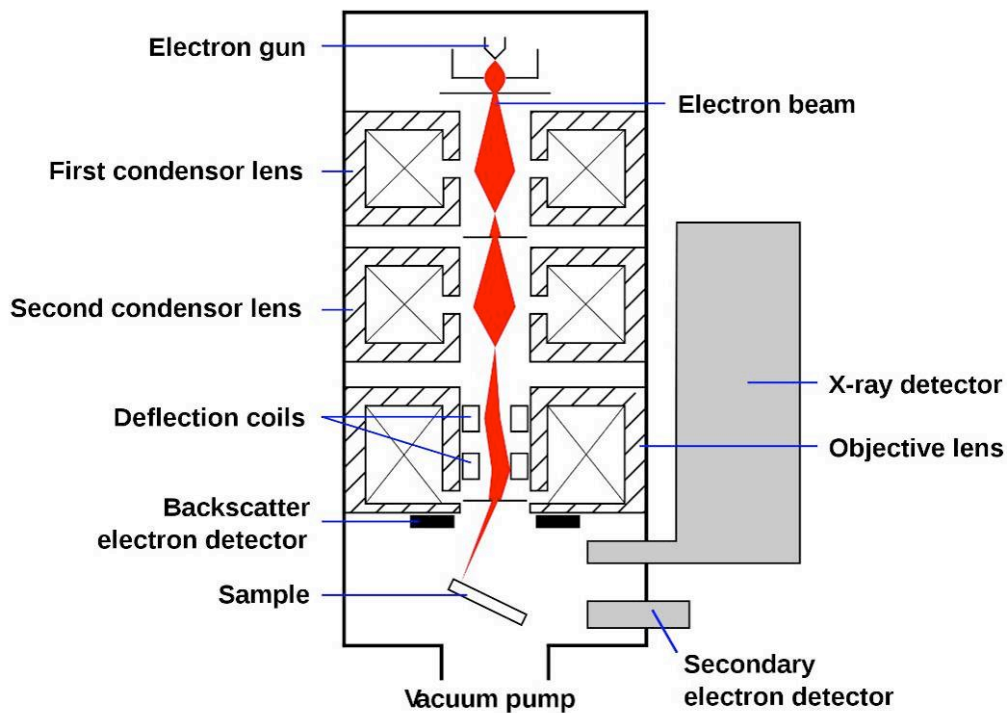


Figure 2-3 Schematic diagram of the Scanning Electron Microscope Equipment

Secondary electron detectors are common in all SEMs, but it is rare that a single machine would have detectors for all possible signals. The signals result from the interactions between the electron beam and the atoms at or near the surface of the sample. In the most common or standard detection mode, secondary electron imaging

(SEI), SEM can produce very high-resolution images of a sample surface, revealing details about less than 1 to 5 nm in size. Due to the very narrow electron beam, SEM micrographs have a large depth of field yielding a characteristic three-dimensional appearance, useful for understanding the surface structure of a sample. A wide range of magnifications is possible, from about 10 times to more than 500,000 times, about 250 times the magnification limit of the best light microscopes.

Back-scattered electrons (BSE) are beam electrons that are reflected from the sample by elastic scattering. BSE are often used in analytical SEM along with the spectra made from the characteristic X-rays. Because the intensity of the BSE signal is strongly related to the atomic number (Z) of the specimen, BSE images can provide information about the distribution of different elements in the sample.

Characteristic X-rays are emitted when the electron beam removes an inner shell electron from the sample, causing a higher energy electron to fill the shell and release energy. These characteristic X-rays are used to identify the composition and measure the abundance of elements in the sample. SEM images of our samples were taken using JEOL JSM-6460 SEM in ACMR NIN and JEOL-A840 in Institute Néel, Grenoble.

2.3.2 Electron Probe Micro-Analysis

Electron Probe Micro-Analysis (EPMA) is a micro-analytical technique that utilizes a finely focused electron beam (like an electron microscope) to excite inner shell electrons of certain sample, and lead to the generation of characteristic X-ray. The X-rays may be detected either by a solid-state detector (EDS, Energy Dispersive Spectrometry), or by a gas-filled detector (WDS, Wavelength Dispersive Spectrometry). Boron microanalysis is difficult because of its very low energy (185 eV) and the associated long wavelength (67.6 Å), thus it is necessary to both consider the large mass absorption of the B $K\alpha$ X-ray by the material's matrix, and use a Bragg diffractor with a large lattice spacing. The development of layered synthetic crystals of large lattice spacing has lead to the ability to analyze the lower atomic number elements, such as Be, B, C, N, O.

2.3.3 Magneto-Optical analysis

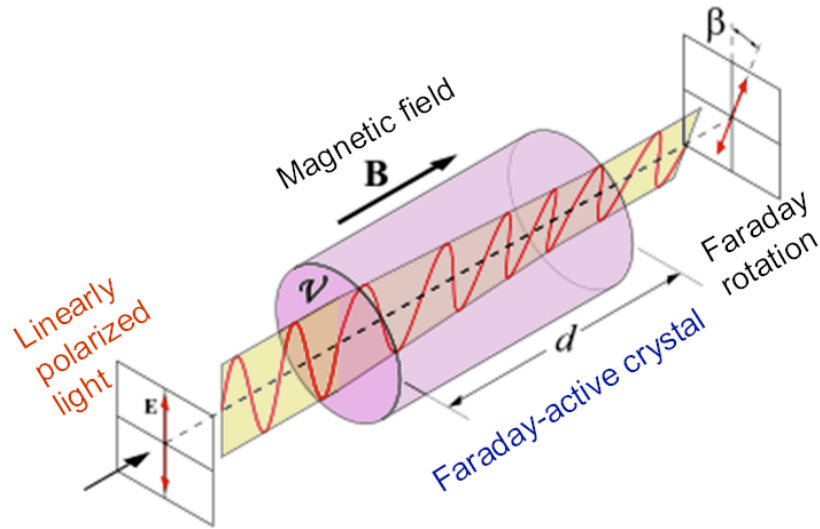


Figure 2-4 Sketch map of Faraday Effect

Magneto-optical phenomenon is based on the Faraday Effect, which is, an interaction between light and a magnetic field in a medium. The rotation of the polarization plane is proportional to the intensity of the component in the direction of the beam of light of the applied magnetic field. The sketch map of Faraday Effect is shown in Figure 2-4.

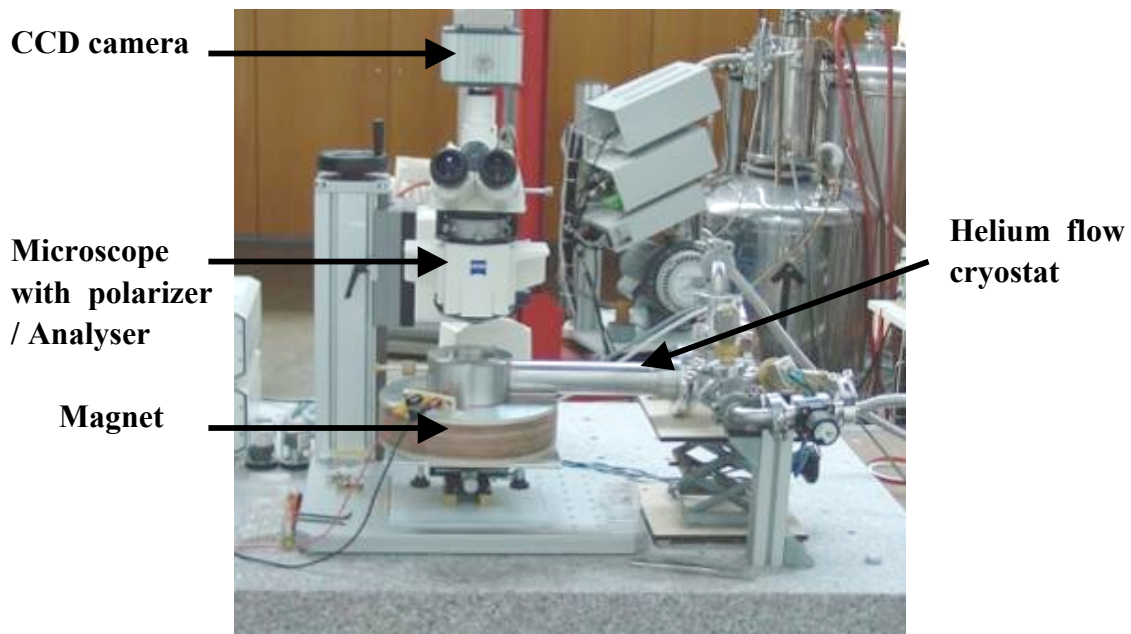


Figure 2-5 Photograph of Magneto Optical Equipment

The materials exhibiting the Faraday Effect that is used in the magneto-optical technique are commonly called the Magneto-Optical Layers (MOL). By detecting the rotation of the light polarization angles above the MOL, it is possible to determine the local field distribution below the MOL. As superconductor has a strong absorption coefficient, the MO measurements are generally taken in the reflection microscopy mode, the light being reflected from the sample or from a thin mirror. Figure 2-5 shows the picture of magneto-optical equipment, where each element of the system is indicated.

2.4 Characterization of superconducting properties

2.4.1 Magnetization measurement

Magnetic susceptibility measurements are also performed to determine the superconducting transition temperature on a Metronique instruments SQUID magnetometer. Two different ways, Zero Field Cooling (ZFC) and Field Cooling (FC) are usually employed to measure the magnetization of superconductor. In the ZFC case, the background magnetic field is firstly dropped to zero, and the sample is cooled down to a temperature below critical temperature. Then a small field, about 10 Oe is applied, and the magnetization measurement of superconductor can be performed. In contrast, in the FC case, the small field is firstly applied, then the sample is cooled down below the critical temperature.

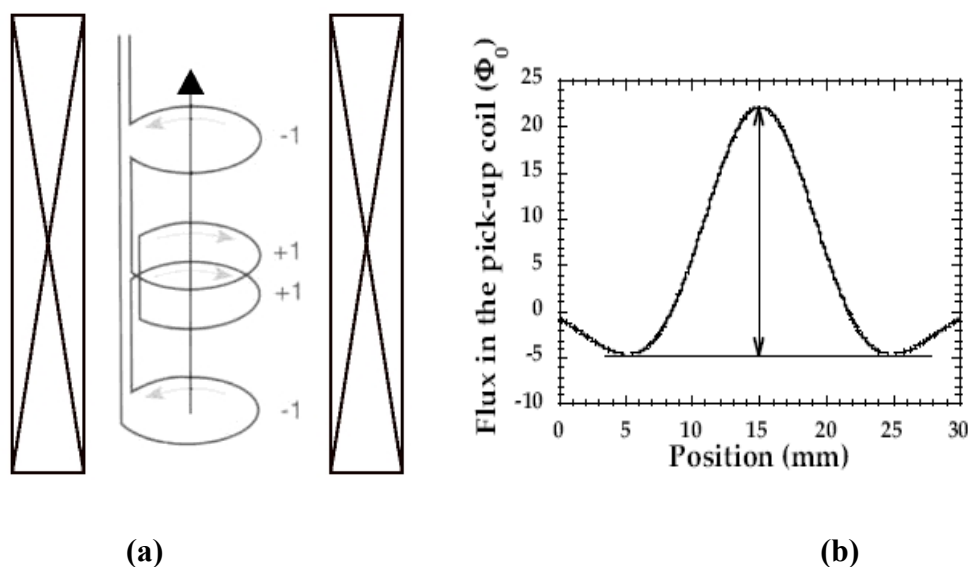


Figure 2-6 Design of the pick-up coil with the superconducting coil (a) and magnetic flux in the coil versus the position of the sample (b)

The principle of this SQUID magnetometer consists of measuring the change of the magnetic flux in a pick-up coil when the magnetized sample is moved throughout it. The sample is mounted at the end of a sliding rod and a steady magnetic field of the required magnitude is applied by means of a superconducting coil in the liquid helium bath. The pick-up coil is configured as a second-order gradiometer (Figure 2-6 (a)) and the magnetic flux versus the position of the sample is represented in Figure 2-6 (b). This design minimizes background noises of the superconducting coil and the environment.

The magnetic moment of the sample is proportional to the amplitude of the flux change, represented by the double arrow on Figure 2-6 (b). The pick-up coil is in a closed superconducting circuit constituting a flux transformer, which conveys the magnetic signal to an rf-SQUID connected to a control electronic and an integrator. The output voltage of this system is an image of the change of magnetic flux in the coil. The sample moves in a tube (not represented here) with a helium gas flowing whose temperature could vary between 1.7 K and 320 K. The applied magnetic field varies between 0 and 7.5 T. The sensitivity in magnetic moment is around 10^{-7} emu (10^{-10} SI) in low field and better than 10^{-5} emu (10^{-8} SI) in high field.

2.4.2 Resistivity measurement

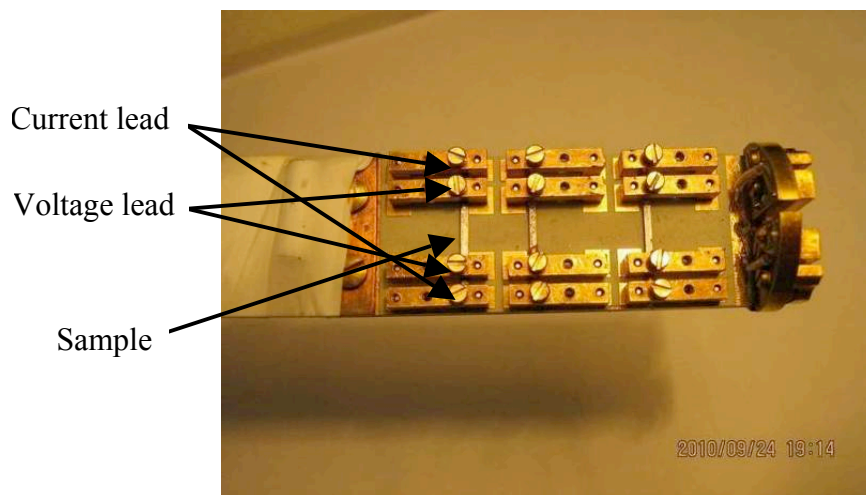


Figure 2-7 The sample holder for resistance measurement

Four point probe resistivity measurement was employed in various external magnetic fields from 4.2 K to 45 K in CRETA Grenoble. The applied DC current for resistivity measurement is 1 mA. The upper critical field (H_{c2}) and irreversible critical

field (H_{irr}) were determined as the 10% and 90% transition on the resistivity temperature ($R-T$) curves. The sample holder is shown in Figure 2-7. The space between current lead is 14 mm and voltage lead is 8 mm. Cu has to be removed using nitric acid measurement because the resistivity of Cu is too low and the superconductivity transition will not be very obvious.

2.4.3 Transport critical current measurement

Critical current density (J_c) is the most important property of superconducting wires or tapes for applications. It indicates the current-carrying limit of wires or tapes. The voltage-current characteristics of MgB_2 wires were measured by standard four point probe method at liquid helium temperature. Each short sample for transport measurement is about 30 mm in length. Four-probe method, which has been proved to be a convenient tool for superconducting current measurement, involves bringing four probes at known distance and geometry into contact with the material of unknown resistance. The wires are connected from four points which are collinear. Current and voltage leads are directly soldered to the surface of the sheath material with a distance of approximately 10 mm between them. Current is applied from the outer probes and voltage was measured from the inner probes as shown in Figure 2-8.

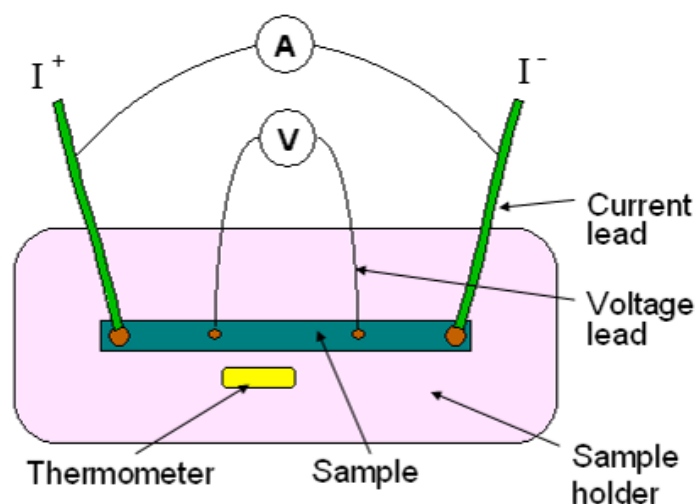


Figure 2-8 Schematic diagram of standard Four-probe method for the MgB_2 wires

The schematic illustration of the transport J_c measurement system is shown in Figure 2-9. The criterion for superconductivity is $1 \mu V/cm$. The capacity of the power supply is DC current 1200 A. During the examination, current ramping and cutting off

are controlled by a computer and the voltage-current ($V-I$) curves are recorded automatically. The background magnetic field is changed with the range from zero to 20 T.

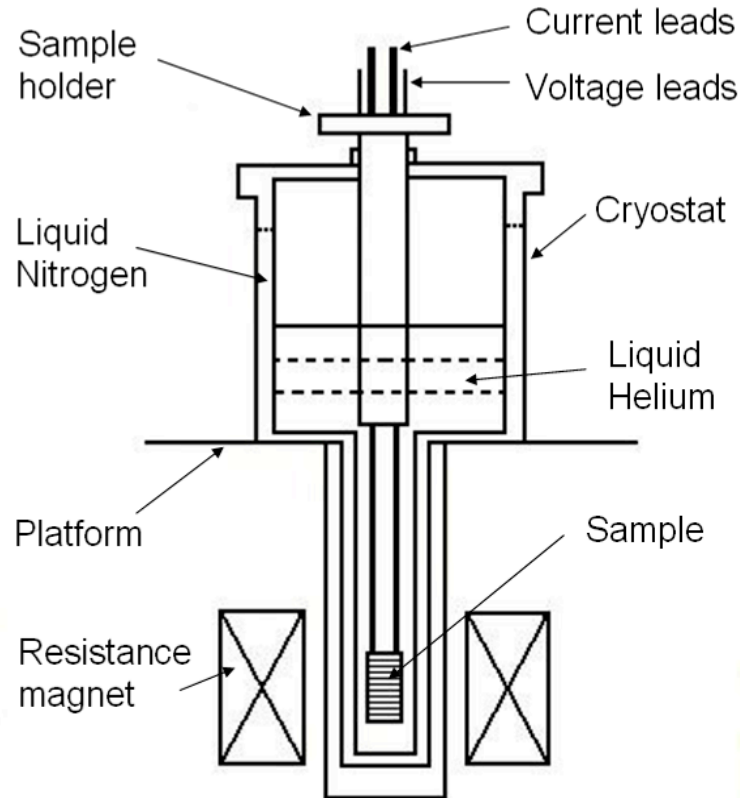


Figure 2-9 Illustration of the facility for transport current measurement

The critical current I_c is directly obtained by the four probe method. J_c is a function of temperature, magnetic field and other parameters, for the practical application, the critical current density J_c and engineering critical current density J_e is more interesting. The J_c and J_e were calculated from I_c with the following equations:

$$J_c = I_c / S_{\text{super}} \quad (2-1)$$

where I_c is the critical current and S_{super} is the superconducting cross-sectional area which carrying the current.

$$J_e = I_c / S_{\text{total}} \quad (2-2)$$

where I_c is the critical current and S_{total} is the cross-sectional area of the full conductor. S was measured with optical microscopy linked with image analysis software.

CHAPTER 3

THE PROPERTIES OF *IN-SITU* MONO-FILAMENTARY MgB₂/Nb/Cu WIRES

In this chapter, the effect of heat treatment temperature on the phase formation process, microstructures, and superconductivities of the mono-filamentary MgB₂/Nb/Cu wires was investigated. Especially the diffusion layer between Nb and MgB₂ core were studied.

3.1 Sample fabrication

Mono-filamentary MgB₂ wire was fabricated by conventional *in-situ* PIT method and the sheath material employs Nb/Cu composite tube with the outer and the inner diameters of 12 mm and 8 mm, respectively. The mixtures of Mg powders (-325 mesh, 99%) and B powders (Alfa, amorphous 99.8%) with stoichiometry of Mg:B = 1:1.9 were well mixed and grounded in agate mortar for 30 minutes in glove box under argon atmosphere. The precursor mixtures were packed into the Nb/Cu composite tubes. Then the filled composite tube was drawn to 1.0 mm wires in diameter. A deformation rate of no more than 10% per pass was used and no annealing was utilized during the whole mechanical deformation process. After the cold deformation, the composite wires were cut and heat treated at various temperatures from 600°C to 950°C for 2 hr in flowing argon, and then cooled to room temperature within the furnace.

3.2 Phase formation analysis of MgB₂/Nb/Cu wires

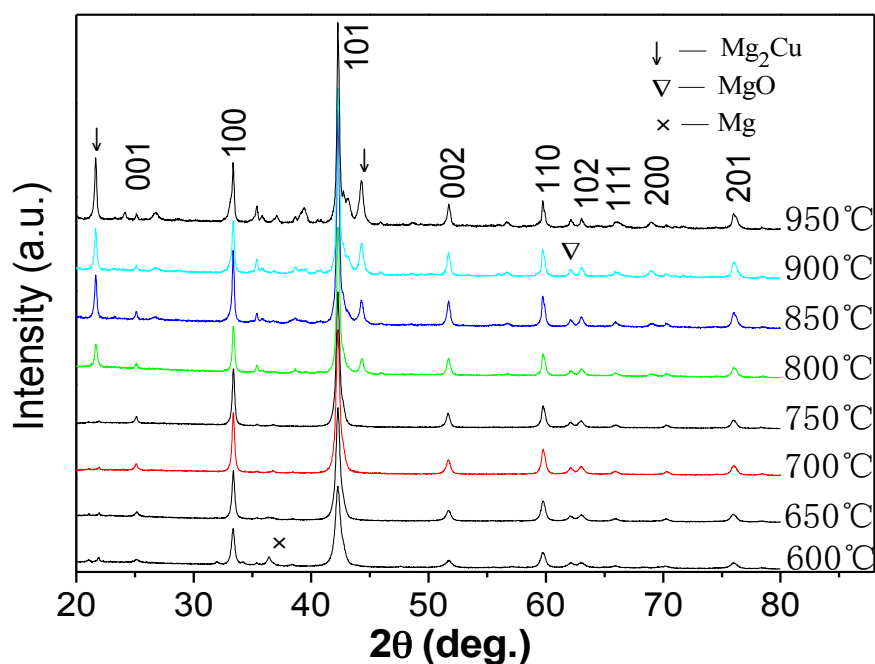


Figure 3-1 XRD patterns of superconducting cores of MgB₂ wires with various sintering temperatures

After mechanically peeling off the Nb/Cu sheath material and grinding the MgB₂ core into powder, phase composition analysis of the core of MgB₂ wires was carried out by powder x-ray diffraction (XRD). Figure 3-1 shows the XRD patterns of MgB₂/Nb/Cu wires at various heat treatment temperatures, 600~950°C. All the wires were sintering for 2 hours. The main phase of MgB₂ as well as the MgO impurities appears at all the samples. In the wire with heat treatment temperature of 600°C, the remnant Mg impurities exist, which means the reaction between Mg and B was inadequacy. And at higher temperatures above 800°C, there are more impurity phase such as Mg₂Cu and other Mg-B compound in presence. Mg₂Cu phase occurs mainly due to the reaction between Mg and Cu at two edges of the samples. When heat treated at 700°C and 750°C, high purity MgB₂ could be obtained except for a little MgO impurity which is inevitable.

Characteristic peaks (002) and (110) of the sample after heated at different temperature were compared in Figure 3-2. The angles of these two characteristic peaks show almost no change, but the values of full width at half maximum (FWHM)

decreases with increasing annealing temperature, indicating that the samples heat treated at higher temperature present higher crystallinity.

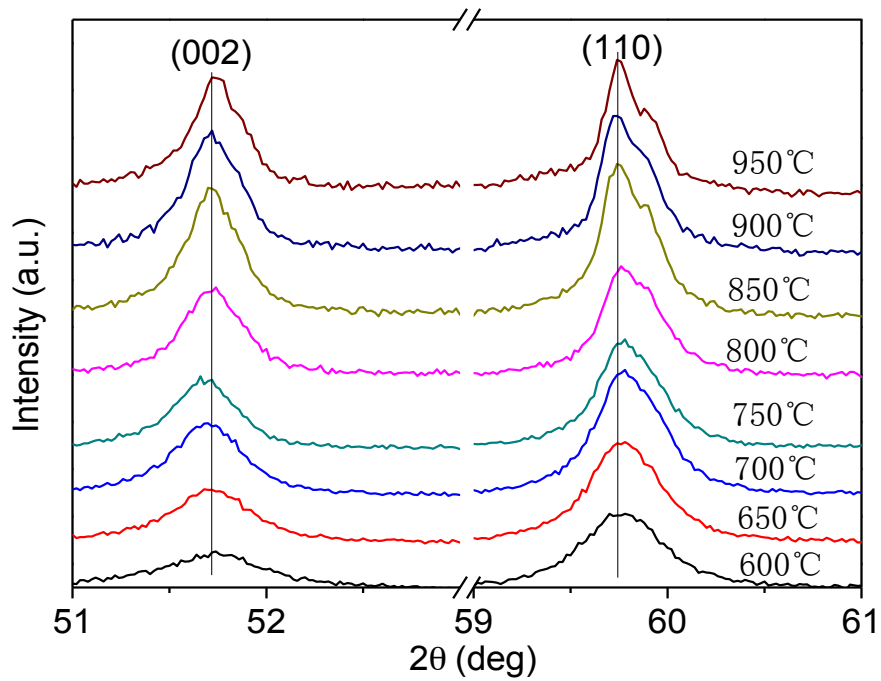


Figure 3-2 Comparisons of the characteristic peaks (002) and (110)

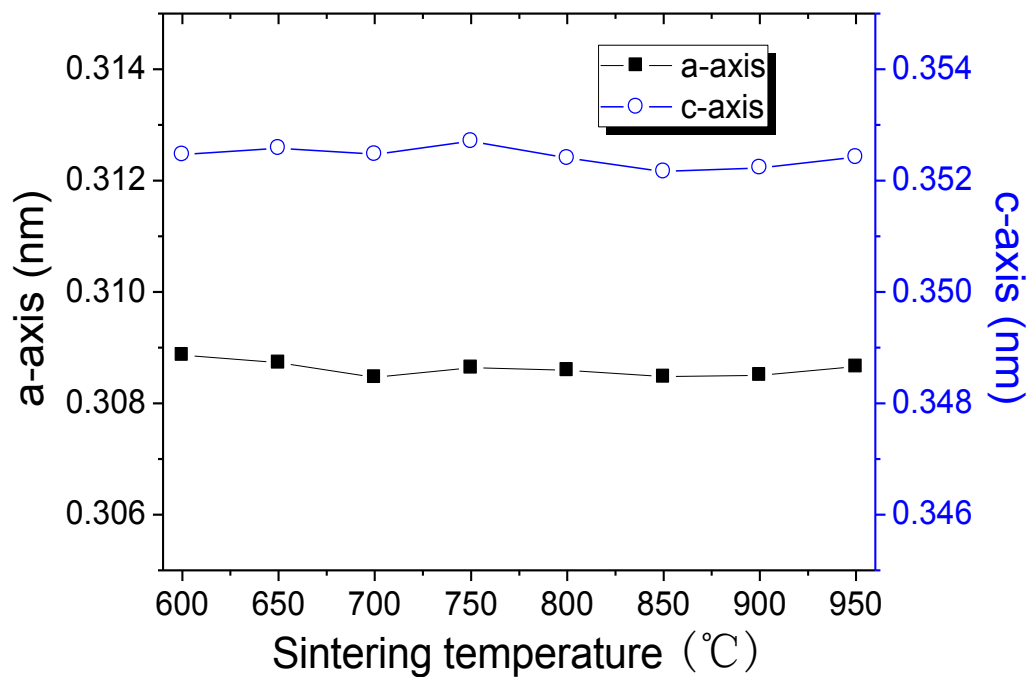


Figure 3-3 Lattice parameters of MgB₂ wires heat treated at different temperature

The lattice parameters of MgB₂ heat treated at different temperatures are shown

in Figure 3-3. We observed that both a - and c -axis lattice parameters did not change within the heat treatment range of 600 ~ 950 °C considering the accuracy of error. That is why the XRD spectra did not show any peak shifting in our samples

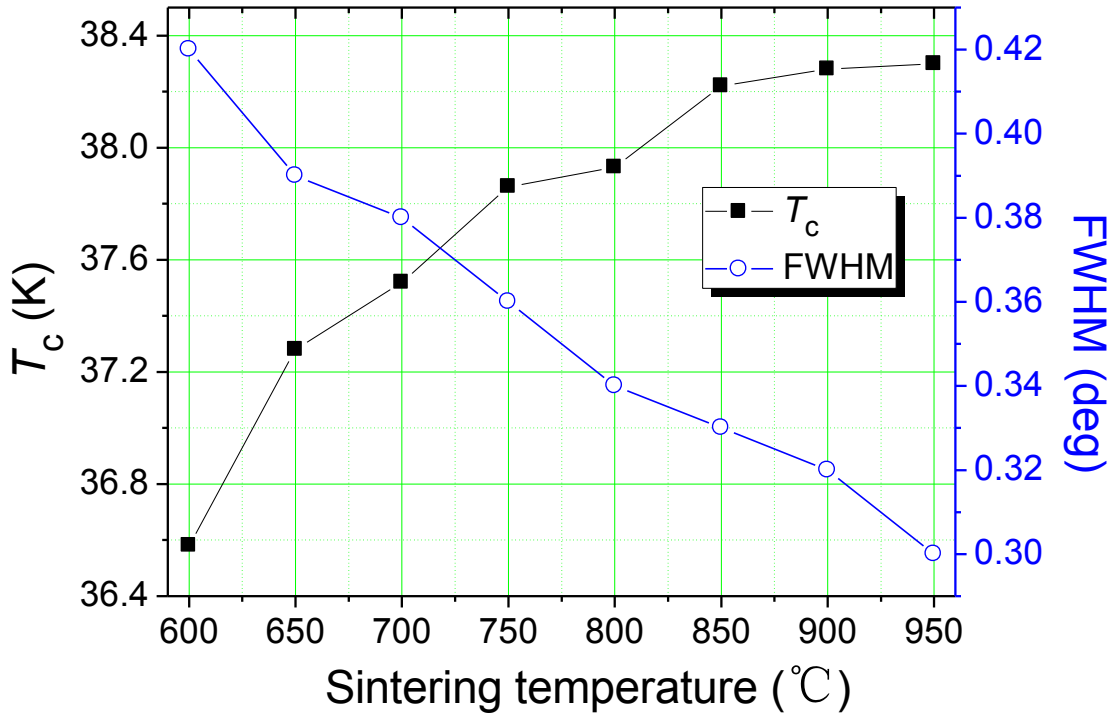


Figure 3-4 The FWHM value of MgB_2 wires heat treated at different temperature

Dependences of both T_c and FWHM on the sintering temperature of MgB_2 (1 1 0) peak are shown in Figure 3-4. Among the different XRD characteristic peaks, the FWHM of (1 1 0) is related to the in-plane crystallinity. An improvement in crystallinity also accompanies with good grain connectivity of the MgB_2 , resulting in the increased superconducting core density^[106]. The analysis of FWHM can provide considerable information on the crystallite sizes and micro/lattice strains that is present in the specimen. In this study, the FWHM decreased with increasing sintering temperature. According to Scherrer's formula, the FWHM value is inversely proportional to the grain size. Meanwhile, it was observed that the behavior of T_c had an opposite trend compared with FWHM. We see that we have a better crystalline and an increased of T_c . Improvement of crystalline accompanies good grain connectivity of the MgB_2 grains. The significant depression of crystallinity for MgB_2 sintered at 650°C resulted in the disorder in the crystal lattice, which is caused by various lattice defects such as intragranular precipitates and unreacted Mg.

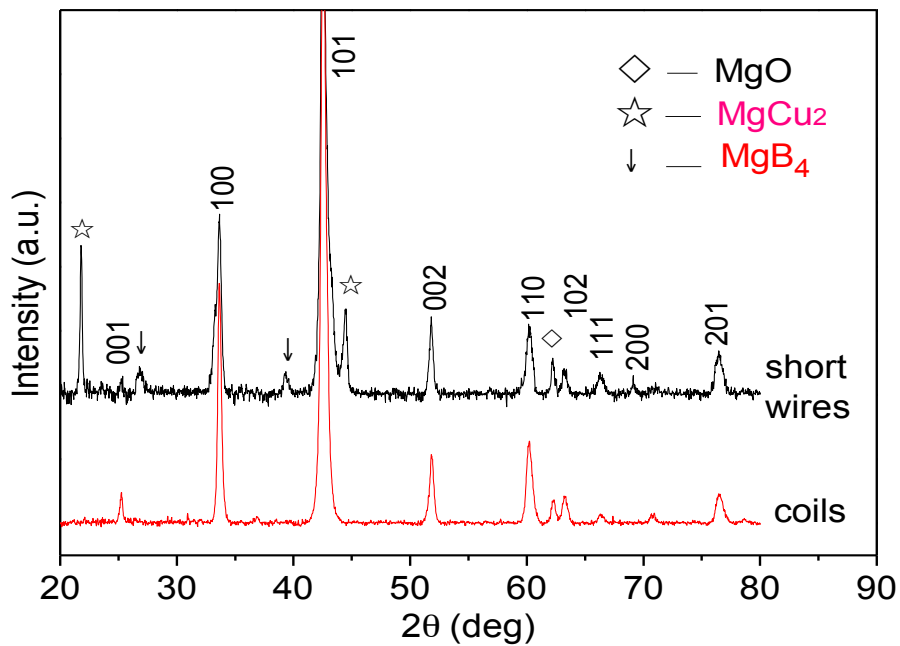
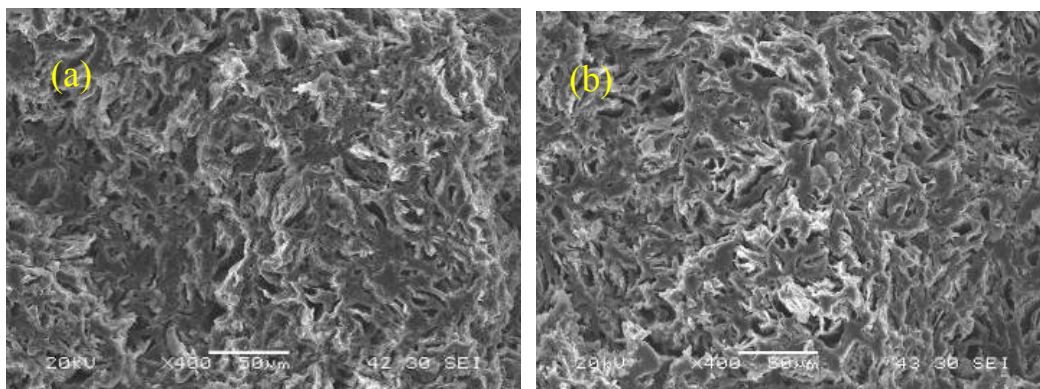


Figure 3-5 XRD patterns of short sample and long wires heat treated at 800 °C

The phase composition is more complex especially after heat treatment at high temperature. So a one-meter-length $\text{MgB}_2/\text{Nb}/\text{Cu}$ wires was wound on a solenoid with 30 mm in diameter and heat treatment at 800°C for 2 h. The only 10 cm length wire was cut from the center part of the sample for XRD measurement. The result is shown in Figure 3-5. There are lesser impurities in the long length sample, especially no MgCu_2 compounds existence. This result indicates that higher purity MgB_2 superconducting phase can be acquired by *in-situ* PIT process using Nb/Cu composite tube as the sheath.

3.3 Microstructure analysis of $\text{MgB}_2/\text{Nb}/\text{Cu}$ wires



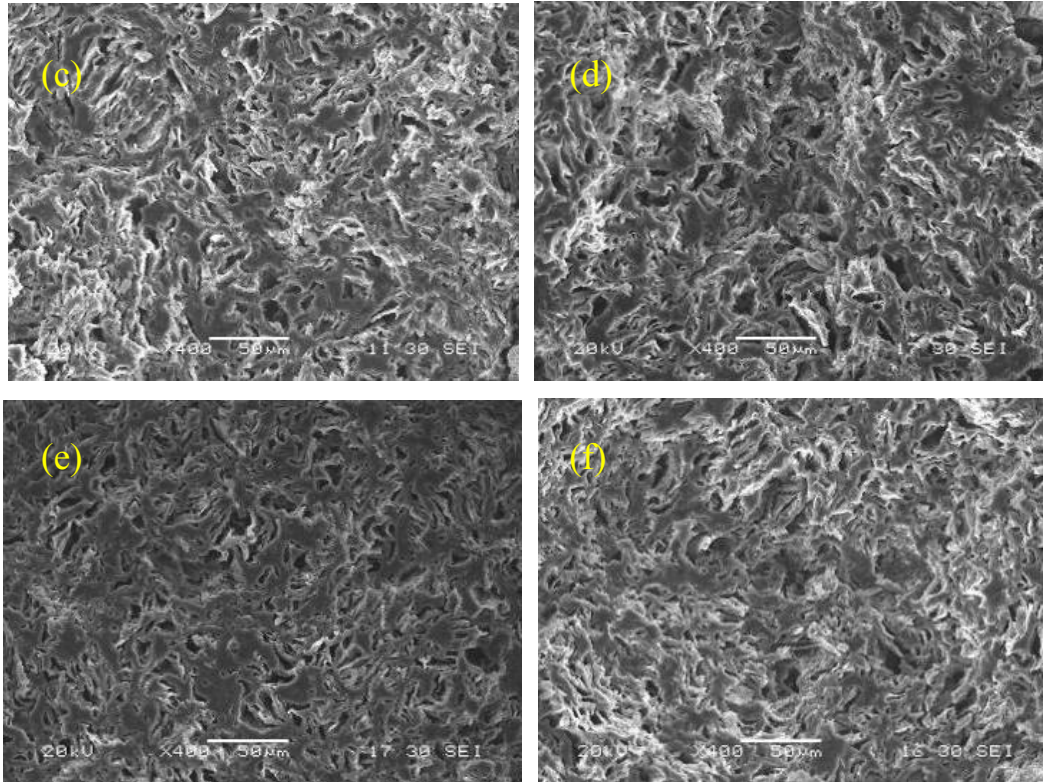
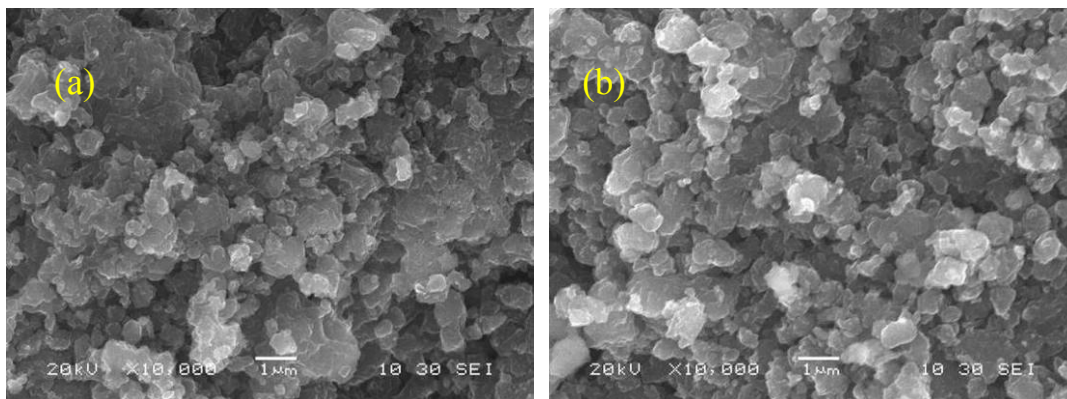


Figure 3-6 Microstructure of MgB₂ wires heat treated at various temperature of a) 650 °C, b) 700 °C, c) 750, d) 800 °C, e) 850 °C, and f) 900 °C

Microstructure images of MgB₂/Nb/Cu wires heat treated at different temperature is shown in Figure 3-6. The crystal topography presented that microscale holes exist in all the samples at lower magnification and the size of these holes increase with increasing sintering temperature. The reason for the presences of these holes may be due to the Mg diffusion into B and lead to the vacant appearances in initial Mg site ^[107]. On the other hand, Mg vapor pressure increased with increasing sintering temperature, so the Mg vapor also increased both the amount of holes and the size of holes with the increasing temperature.



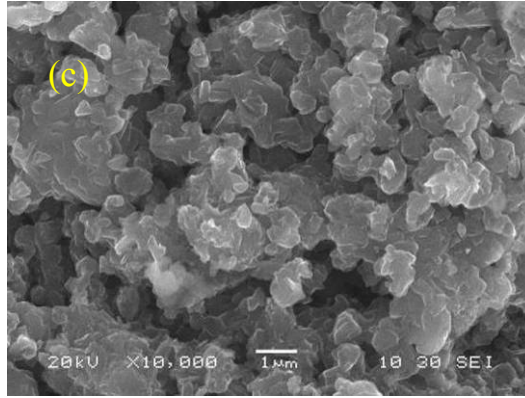


Figure 3-7 SEM pictures of MgB₂ wires at a magnification of 10000× times. a) 650 °C, b) 750 °C, and c) 850 °C

As shown in Figure 3-7, we can find some larger size MgB₂ grains when heat treatment at 850°C at larger magnification, which implies the further growth of MgB₂ grains at high temperature. As well known, MgB₂ is a typical type II superconductor, and the grain boundary is an effective flux pinning centers ^[108]. Obviously, the larger MgB₂ grains will reduce boundary areas, and weaken the flux pinning, which will decrease the $J_c(B)$ properties of the wires. Therefore, to avoid the overgrowth of the MgB₂ grains, we should select a moderate temperature as the final heat treatment temperature.

3.4 Superconducting performance of MgB₂/Nb/Cu wires

3.4.1 Critical temperature T_c derived by magnetization and resistance

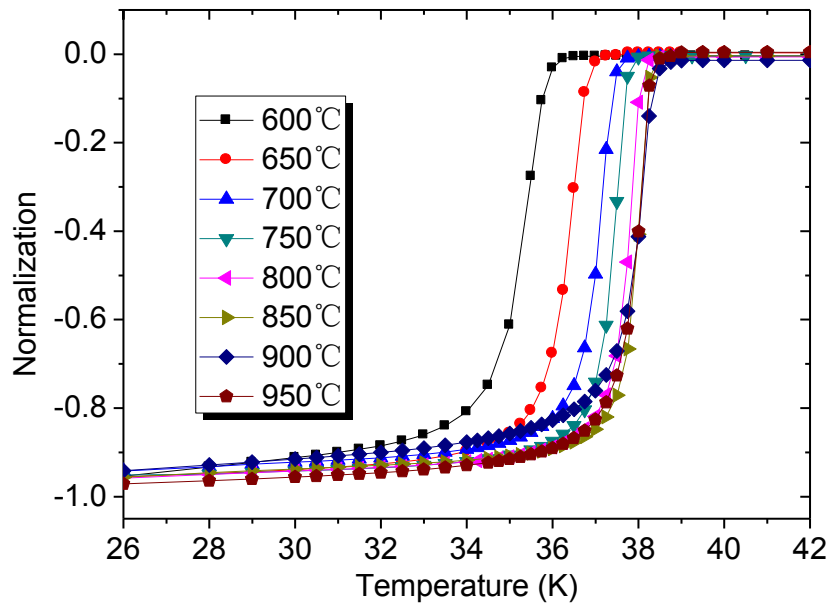


Figure 3-8 Magnetization curves of MgB₂ wires with various sintering temperatures

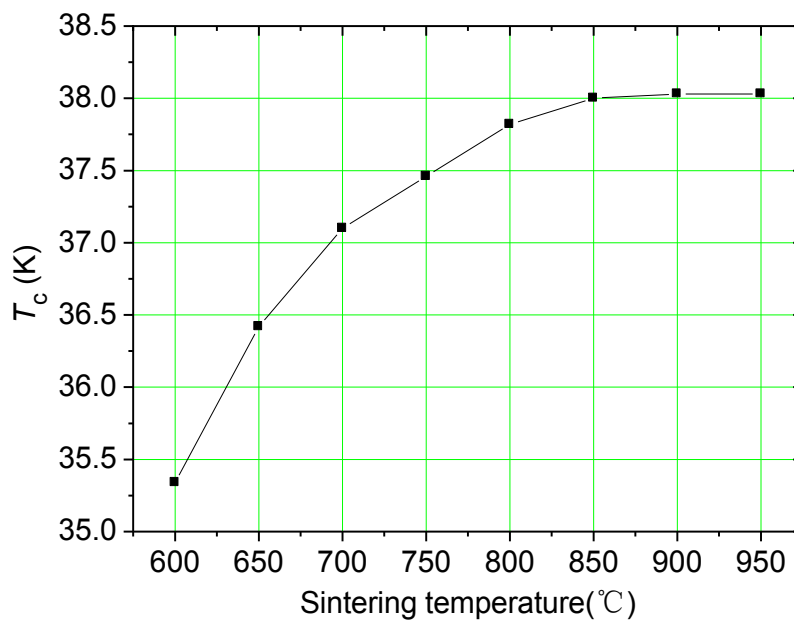


Figure 3-9 Sintering temperature dependence of T_c , T_c values obtained from the onset

of superconducting transition curves during the magnetization measurement.

Figure 3-8 shows the normalized DC magnetization dependence on the heat treatment temperature, and Figure 3-9 shows the heat treatment temperature dependence of T_c . The onset of transition temperature ($T_{c \text{ onset}}$) for the un-doped sample heat treated at 600°C was 36.1 K. It increased to 38.2 K with the heat treatment temperature increases to 900°C. Meanwhile, the superconducting transition width (ΔT_c) of the MgB₂ superconductor decreased with increasing heat-treatment temperature, which suggested that the enhancement of T_c can be explained by the improvement of crystallinity of pure MgB₂ core. On the other hand, the T_c values of the sample heat treated at 900°C slightly decreased due to the formation of non-superconducting phases as mentioned previously.

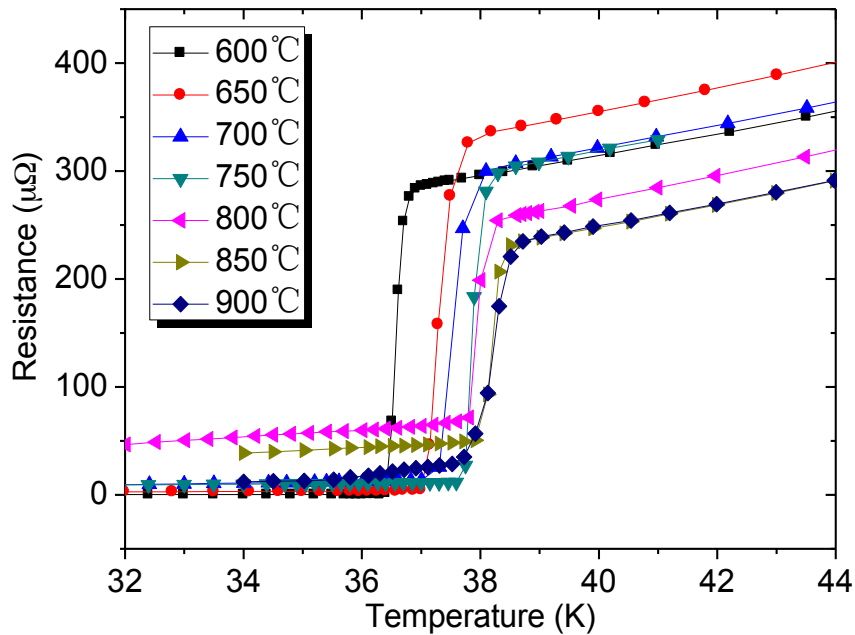


Figure 3-10 Resistance vs measurement temperature curves of MgB₂ wire heat treated at different temperatures

The critical temperature of the MgB₂ wires was determined by using the resistance and the magnetization measurement, respectively. Figure 3-10 displays the resistance as a function of the temperature for the wires sintered at different temperatures. The resistance measurements were done by the conventional four-probe method at self-field. Interestingly, the resistance of MgB₂ wire did not keep zero

below T_c while the heat-treatment temperature is higher than 700 °C, but for the lower temperature sintered samples, the result showed completely superconducting. In parallel, we see by magnetization measurement that MgB₂ is superconducting. These results combined with EDS and SEM observation. It was proposed that it may form a diffusion layer between Nb and MgB₂ core while heat treatment temperature is higher than 700°C. This diffusion layer is not superconducting, so there is partly current transfer through Nb sheath and produces a few resistances. This explanation will be further proved by the following results.

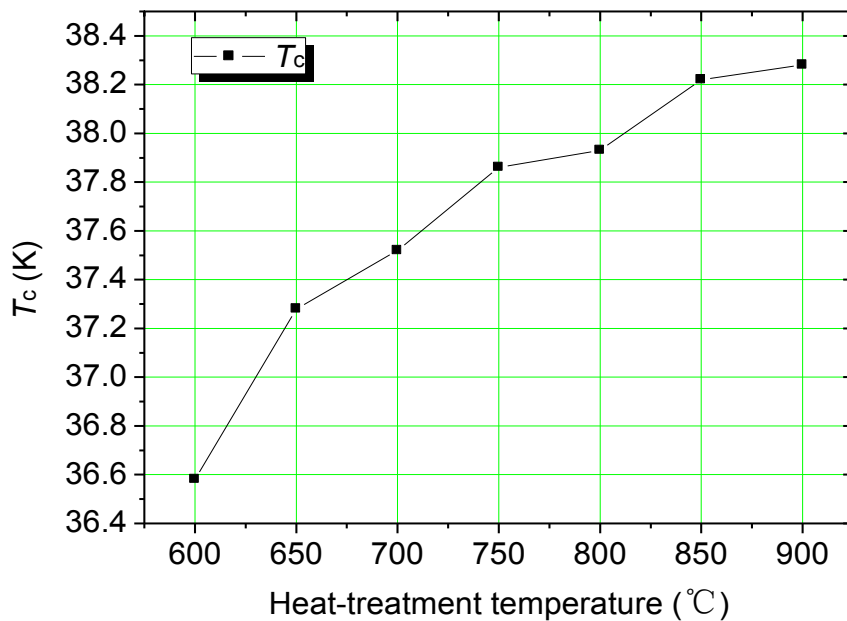


Figure 3-11 Relationship between the heat treatment temperature and T_c

Figure 3-11 displays the relationship between T_c and heat treatment temperature, T_c obviously increases with the increase of heat treatment temperature. It is because that the increase of heat treatment temperature will result in the enhancement of crystallinity and superconductivity of MgB₂ core due to the more complete reaction of Mg and B. The above explanation is consistent with the results of resistance measurement, as shown in Figure 3-8 and 3-9.

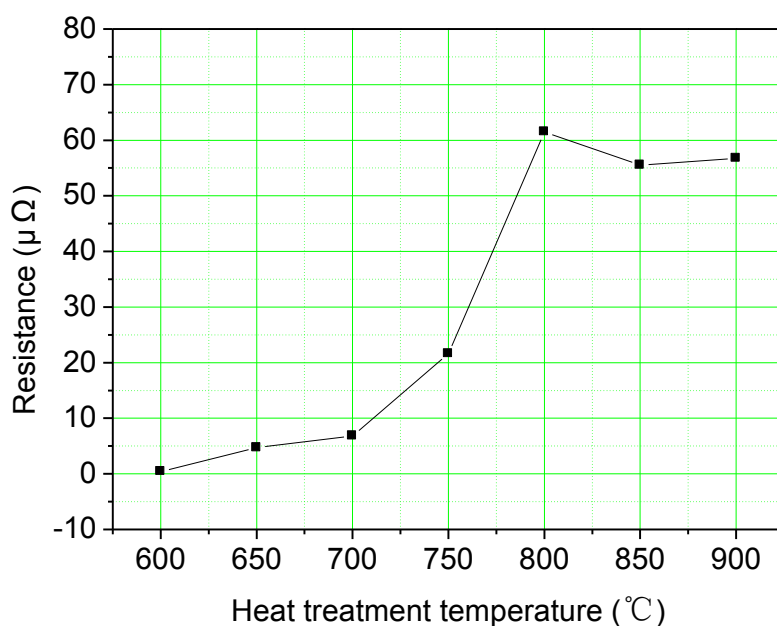


Figure 3-12 Residual resistance just below the transition point as a function of heat treatment temperature

Figure 3-12 shows the resistance below the transition temperature dependence on the heat treatment temperature. From this figure we can see the resistance was very small while the sintering temperature is below 750°C, and increased very fast when the heat treatment temperature went higher than 750°C. Both the results of magnetization and XRD measurement show that high purity MgB₂ phase can be obtained while heat treatment the sample at higher temperature. These results joint with EDS observation (see below paragraph 3.5.1), allow to conclude that the resistance is due to interface, as already observed by C R M Grovenor.^[109]

3.4.2 Transport critical current density J_c of MgB₂/Nb/Cu wires

3.4.2.1 Short length MgB₂/Nb/Cu sample

The heat treated sample was cut into about 3 cm in length. The short wire was emplaced on the sample holder with its axis perpendicular to the applied field. The current and voltage leads were then soldered on the surface of samples, keeping the distance between two voltage leads with 10 mm length. At last, the sample holder was put into the cryostat. The criterion of 1 μV/cm was adopted to determine J_c values of short sample. The testing magnetic field was in the range of 0~10 T. J_c is defined by

dividing the normalization of the critical current (I_c) to the cross-section area excluding that of stabilizing Cu and barrier layer Nb. The I_c values can be compared to the same kind of wires since these wires almost share the same area of MgB_2 cores. For practical application, it is necessary to have the data for engineering critical current density J_e which is the normalized I_c divided by the entire cross-section area of the wire. J_e is used to judge to the quantity of superconducting wires in engineering.

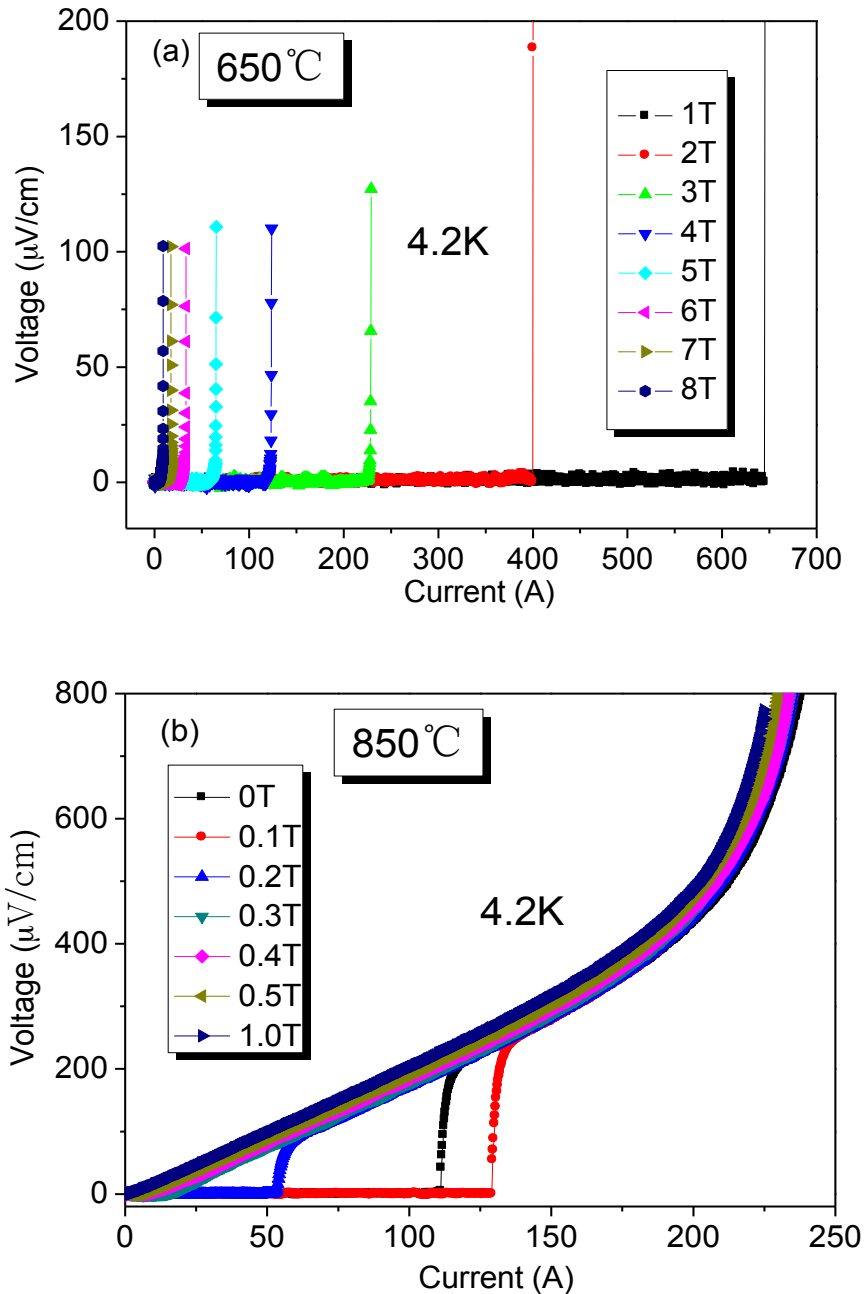


Figure 3-13 Voltage-Current Curves of the $MgB_2/Nb/Cu$ wires heat treated at (a) 650 °C and (b) 850 °C at 4.2K

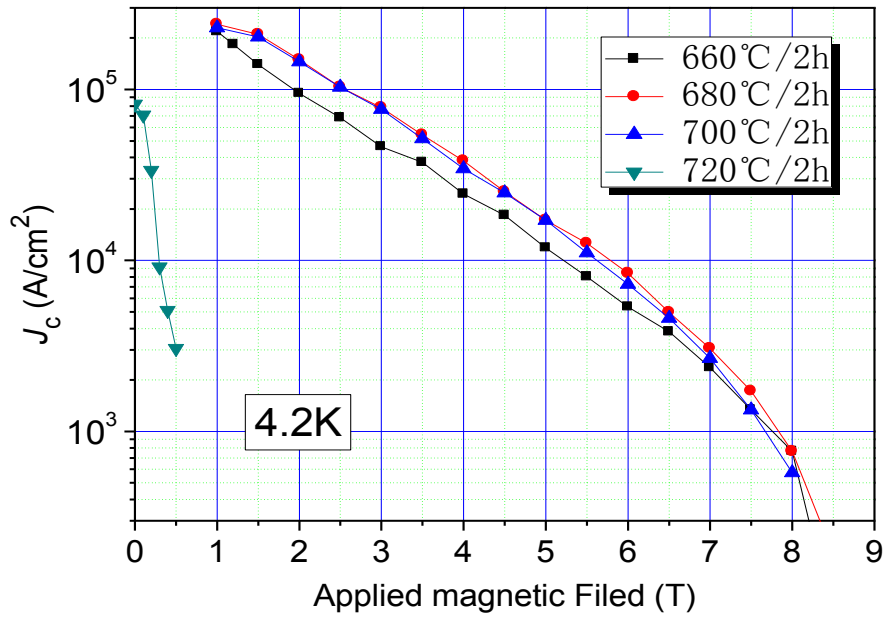


Figure 3-14 Transport J_c of short $\text{MgB}_2/\text{Nb}/\text{Cu}$ wires with different sintering temperatures at 4.2K

Figure 3-13(a) shows the V - I curves at 4.2 K with various applied fields up to 8 T of the MgB_2 wires after heat treatment at 650°C for 2 hours. It can be observed that the $\text{MgB}_2/\text{Nb}/\text{Cu}$ short wire shows a fine I_c - B performance. At 4.2K, 1T and 2T, the I_c values reach 645A and 400A, respectively. Furthermore, the superconducting transition curves for all the fields, up to 8T are very sharp, indicating the sample with a very perfect superconductivity. Figure 3-13(b) shows the results of V - I measurement of the wires with heat treatment at 850°C for 2 hours. Unexpectedly, the results of I_c measurement at this sample are very different. Comparing to the sample with heat treatment of 650°C , superconducting performance of the sample sintered at 850°C degrades seriously. At 4.2K and self-field, I_c of this sample is only 130A, much lower than that of the $650^\circ\text{C}/2\text{h}$ sample, and at 4.2K, 0.3T, the wire exhibits not-superconducting. The degradation of I_c of $\text{MgB}_2/\text{Nb}/\text{Cu}$ wire with the increase of heat treatment temperature should be attributed to the enlargement of the MgB_2 grain size, which will depress the current-carrying and flux pinning properties of MgB_2 superconductor, since the grain boundaries are thought to be the main effective flux pinning centers at MgB_2 .

Transport critical current (J_c) as a function of magnetic field for

monofilamentary $\text{MgB}_2/\text{Nb}/\text{Cu}$ wire heat treated at various temperatures is shown in Figure 3-14. It can be observed for the samples with heat treatment of 660 °C, 680 °C and 700 °C, the J_c - B properties were almost the same, but surprisingly while the heat treatment temperature increase up to 720 °C, the transport J_c performance degraded rapidly. It is completely different from the results of magnetization measurement in which the J_c - B properties of samples with heat treatment of 700 °C and 720 °C is not so different. For understanding the reasons, EDS, MOI characters of superconducting wires have been investigated, which will be discussed later.

3.4.2.2 J_c - B performance of $\text{MgB}_2/\text{Nb}/\text{Cu}$ coil

(1). Wind and Reaction $\text{MgB}_2/\text{Nb}/\text{Cu}$ coil preparation and measure



Figure 3-15 Coils with MgB_2 wires for transport current measurement

For the small coils measurement, Wind and React (W&R) method was employed in this paper. As shown in Figure 3-15, the monofilament $\text{MgB}_2/\text{Nb}/\text{Cu}$ wire with 1.2 meter in length is fixed on the sample holder and heat treated at various temperatures at flowing argon, and then the current leads and voltage leads were soldered on that. The sample holder consists of a thread groove and hollow cylinder of $\text{Ti}_6\text{Al}_4\text{V}$ with two copper rings attached for current contact. The size of the $\text{Ti}_6\text{Al}_4\text{V}$ hollow cylinder is 35 mm in height and 32 mm in outer diameter with U-shape groove. A graphite coating is sprayed on the $\text{Ti}_6\text{Al}_4\text{V}$ grooved surface before the holder is put inside of a vacuum furnace and sintered at 700 °C for 10 hours, in order to avoid the stick between wires and sample holder. The $\text{MgB}_2/\text{Nb}/\text{Cu}$ wire is then wound on the

graphite-coating groove surface prior to heat treated in a tubular furnace. The coil sample was set inside the tubular furnace which was then emptied with a vacuum pump. Ar gas was leaded through the furnace, keeping the ambient pressure during the heat treatment. The ramp rate for heating up was 600 °C/hr. The reaction temperatures of 660 °C, 680 °C, 700 °C, and 720 °C were adopted and holding 2 hours, respectively. After holding duration the samples were cooled down with furnace.

The heat treated coil sample was fixed on the testing support cane with its axis parallel to the applied field. The attached copper ends of the sample holder were soldered to the current leads of the support with braided tapes. The voltage lead on the testing sample support were soldered to the sample with the intervals of ~100 mm (1 turn) and 500 mm (5 turns). Two additional varnished Cu wires were also wound and soldered to the voltage taps with the winding direction identical to that of the helical superconducting wire, in order to produce an inductive anti-wise electric field to reduce noise. Then, the coil sample holder was put inside the cryostat, immersing it in the liquid helium bath. The current leads and voltage leads were connected before testing. During the transport current measurement, the voltage-current curves were recorded automatically and the applied field was up to 10 T. The criterion of 1 $\mu\text{V}/\text{cm}$ was used to determine the value of critical current I_c which was then divided by the MgB_2 area of the wire cross section to obtain the J_c values. According to the relation $F_p=J_c\times B$, the flux pinning force varied with the applied field can also be depicted from the J_c values.

(2). Result and analysis

Figure 3-16 shows the J_c as a function of applied magnetic field for MgB_2 coil after heat treated at 680 °C, 700 °C, and 720 °C, respectively. The J_c value is slightly lower than that in short sample with same heat treatment temperature. The higher J_c was reached at the heat treatment temperature of 700 °C. J_c - B curve moves upwards from 680 °C to 700 °C and reaches the highest values at 700 °C, especially at higher field; at 720 °C, the J_c value is a little decrease.

With the further increase of heat treatment temperature, the $\text{MgB}_2/\text{Nb}/\text{Cu}$ wires exhibit non-superconducting, which is similar the results in short samples, as shown in Figure 3-14. However, this result is not consistent with the previous measurement

results such as XRD and magnetization, in which these samples exhibited fine superconductivity at heat treatment temperatures from 600°C to 950°C, as shown in Figure 3-1, 3-8 and 3-11. One of the possible reasons is that the current only transports in Nb/Cu matrix but not in MgB₂ superconducting cores. It means maybe there have formed a diffusion layer between the Nb and MgB₂ while heating the sample at higher temperature and this diffusion layer is thicker and with poor electric conductivity.

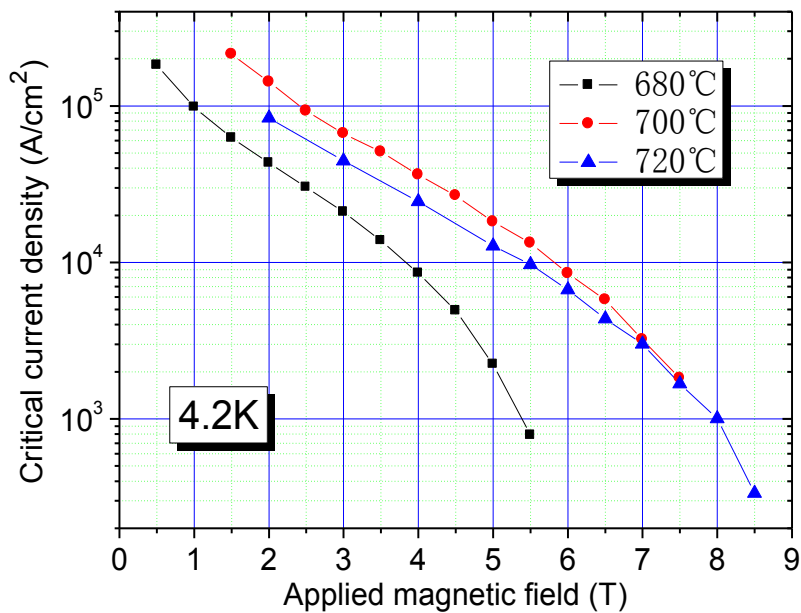


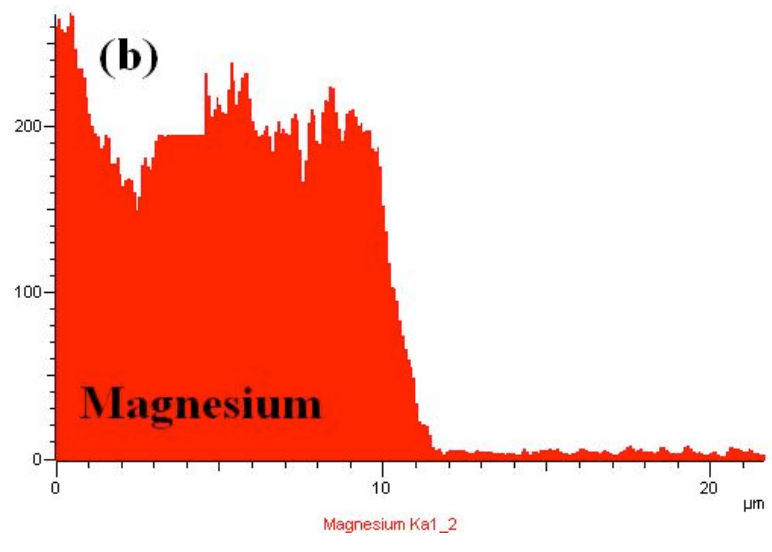
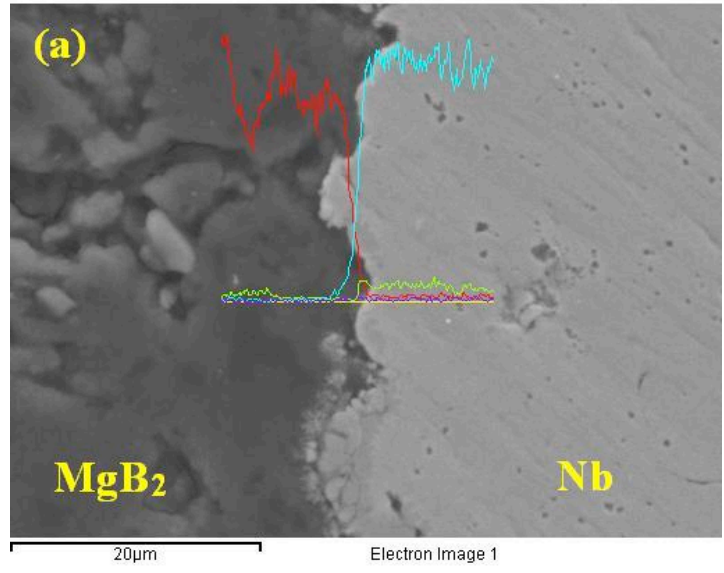
Figure 3-16 Transport J_c as a function of the field for MgB₂ coil at 4.2K

3.5. The interface between Nb and MgB₂ core

As mentioned above, it is found that while the heat treatment temperature increases up to a certain value, the magnetic field dependence of transport J_c for both short samples and long coils sharply drop. But strangely, for the samples with this different heat-treatment temperature the superconducting properties investigated by the resistivity and magnetization are not so various. A possible reason is the formation of a thick diffusion layer between the Nb barrier and MgB₂ cores at high sintering temperature. For testifying the above explanation, we further studied the phase formation, microstructures of the interface between Nb and superconducting cores by Energy Dispersive Spectrometry (EDS), Electron Probe Micro-Analyzer (EPMA),

and Magneto Optical Imaging (MOI).

3.5.1 EDS analysis of MgB₂-Nb interface



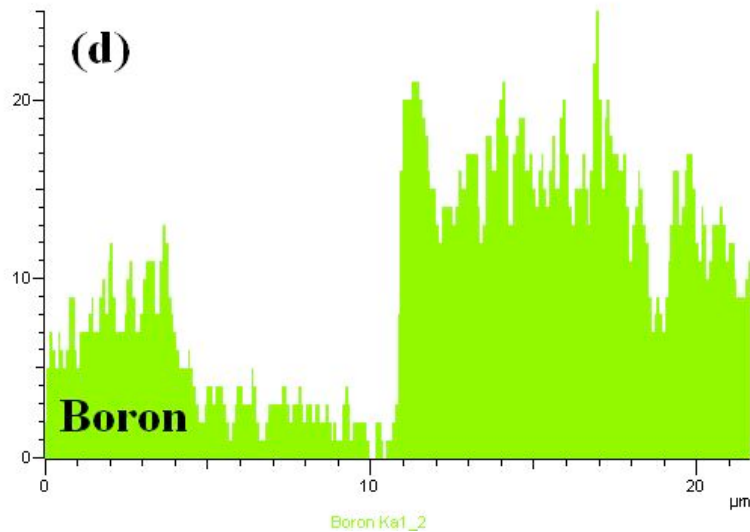
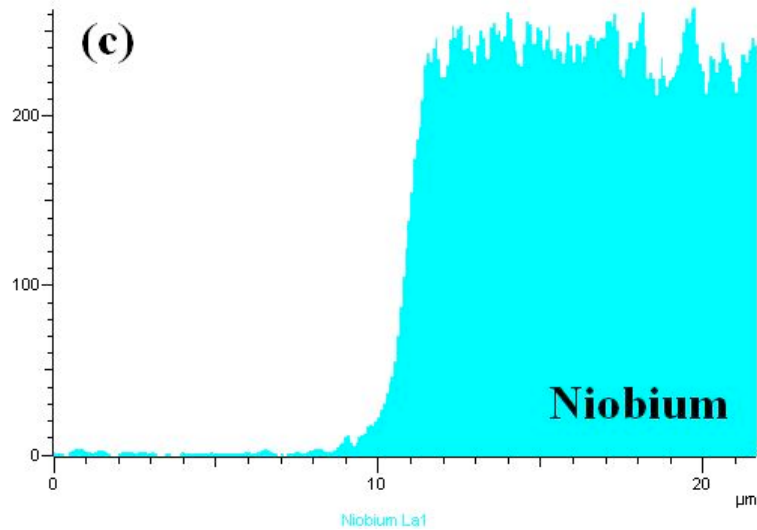


Figure 3-17 EDS Analysis of the interface layer between MgB_2 and Nb

Figure 3-17 shows the SEM image of the interface region and EDS map of Mg, B and Nb distribution. The left is the MgB_2 core and the right is Nb sheath in Figure 3-17(a). Figure 3-17 (b)-(d) is the EDS line scan curve of Mg, Nb and B, respectively. The obvious feature is that B content reduced in MgB_2 section. We can estimate that there is some B diffusion into the Nb side. The B content in Nb side is not precise due to the superposition of $\text{B-K}\alpha$ and $\text{Nb-L}\alpha$ peaks.

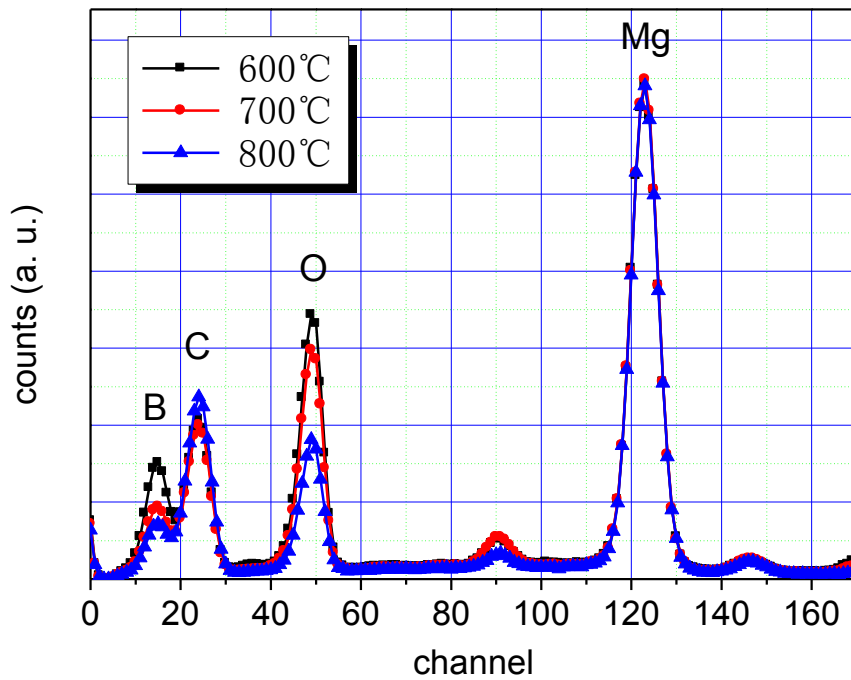


Figure 3-18 EDS analysis of MgB₂ superconductor filament

Figure 3-18 shows the EDS results of MgB₂ superconducting cores at different sintering temperature. The data is normalized to Mg peaks. It can be seen that with the increase of sintering temperature, intensity of the B peak drop gradually, as well as the peaks of O element. It indicates that the loss of B with the increase of heat treatment temperature is quite obvious. This result directly proves the diffusion of B to Nb at high sintering temperature, which agrees with the previous results and literature report ^[109]. Therefore, the lack of superconducting properties in this wire is the result of very rapid diffusion of B into the thick Nb sheath, and consequent severe depletion of B in the core. Meanwhile, there are original oxides impurities in the precursor powders, and high sintering temperature may result in O element substitution for B sites of MgB₂ lattices, and lead to the decrease of O impurities content.

3.5.2 Magneto-Optical Imaging analysis of the MgB₂-Nb interface



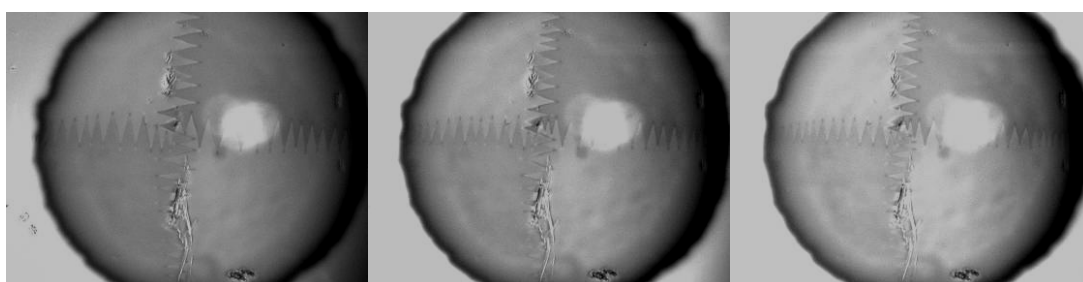
(a)



(b)

(c)

(d)



(e)

(f)

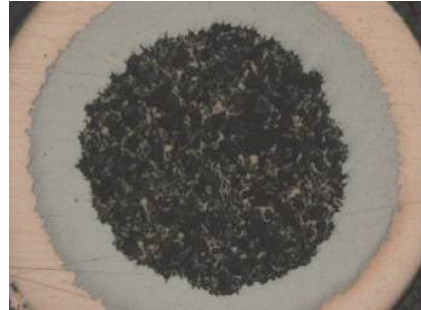
(g)

Figure 3-19 Magneto-optical image of MgB₂ wires heat treated at 650 °C under the magnetic fields from zero to 100 mT

To understand the interfacial diffusion behavior, the flux motion in these MgB₂/Nb/Cu wires was measured using Magneto-Optical Imaging (MOI) at various temperatures from 6 K to 40 K. The sample was Zero Fields Cooled (ZFC) down to 6 K (the lowest temperature limit of the equipment) and then a magnetic field up to 100 mT was applied parallel to the sample. The flux penetration was recorded during the field increasing and decreasing cycle.

The interaction between the Nb sheath and MgB₂ superconductor core with local

MO imaging for perpendicular applied fields was investigated. Such interactions are mainly visible in the case of the ZFC state and $H = 100$ mT. The typical MO images of MgB_2 wires heat treated at 650°C and 800°C are presented in Figure 3-19 and Figure 3-20, respectively.



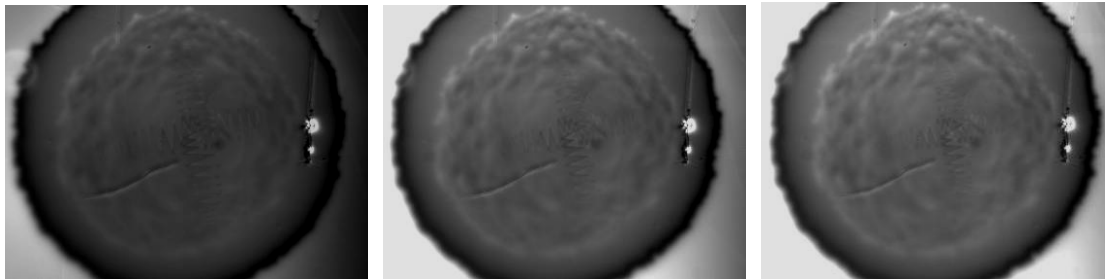
(a)



(b)

(c)

(d)



(e)

(f)

(g)

Figure 3-20 Magneto-optical image of MgB_2 wires heat treated at 800°C under the magnetic fields from zero to 100 mT

Figure 3-19 (a) is the optical microscope image. The dark zone in center is the MgB_2 , next to Nb sheath, and the outer layer is Cu stabilizer. Figure 3-19 (b)-(g) were taken after the sample was cooled down to 6 K and the applied magnetic fields were 0, 20, 40, 60, 80, and 100 mT, respectively. The bright regions correspond to the high flux density values, and the dark areas are in Meissner state. The dark scratches

and bright point are defects of the ferrite garnet reflection layer, which do not change their color when the external magnetic field is changed. The background brightened step by step with the external field increasing, which means the magnetic flux increased at the outer edge between the MgB₂ core and Nb sheath. There is no significant change in Nb layer, but the luminance of MgB₂ core was a little brightened with the field increased, which was due to the partly penetration of the magnetic flux lines into the MgB₂ superconductor, since the lower critical field (H_{c1}) of MgB₂ is very low of around 20-40 mT at 6 K,.

Figure 3-20 is MOI of MgB₂/Nb/Cu wires heat treated at 800°C. Corresponding with the Figure 3-19, the figures from (a) to (g) were optical microscope image, MOI at 0, 20, 40, 60, 80, and 100 mT at 6 K with ZFC, respectively. When the magnetic field increased, a blurry bright ring can be observed at the interface between the MgB₂ core and Nb, and becomes clearer with the further increase of field, Th. Schuster *et al.* [110] consider this bright ring should be due to the magnetic flux concentration at the interface between a weaker superconductor (Nb) and a stronger superconductor (MgB₂). Perhaps this is one of the reasons. However, we think that the ring maybe due to the non-superconducting layer between MgB₂-Nb interfaces. This idea can be confirmed by the magneto-optical images heat treated at different temperatures.

Meanwhile, the color of MOI in the internal MgB₂ area is not uniform, and there are some structural patterns especially when the external field is higher than 40 mT. This suggests that the flux lines penetrated into the MgB₂ cores and didn't distribute uniformly for the samples heat treated at high temperatures. We think it's likely that the flux behaviors are due to the weak flux pinning ability caused by the impurity phase concentration in the grain boundary as a result of the grain growth.

The effect of the sintering dwelling time on the interface of Nb and MgB₂ was also investigated. Figures (a), (b), (c), and (d) in 3-21 were the MOI of the wires heat treated at 800°C for 5, 10, 20, 30 hrs, respectively. During the experiment, for the clear observation of the interface between Nb and MgB₂, we cooled down the sample to 12 K first, then applied the field to 40 mT, continued to cool to the target temperature of 6 K with this field afterwards and finally took off this field. So, this process is Field Cooling (FC) for Nb and Zero Field Cooling (ZFC) for MgB₂. The trapped flux was kept in the sample after this process.

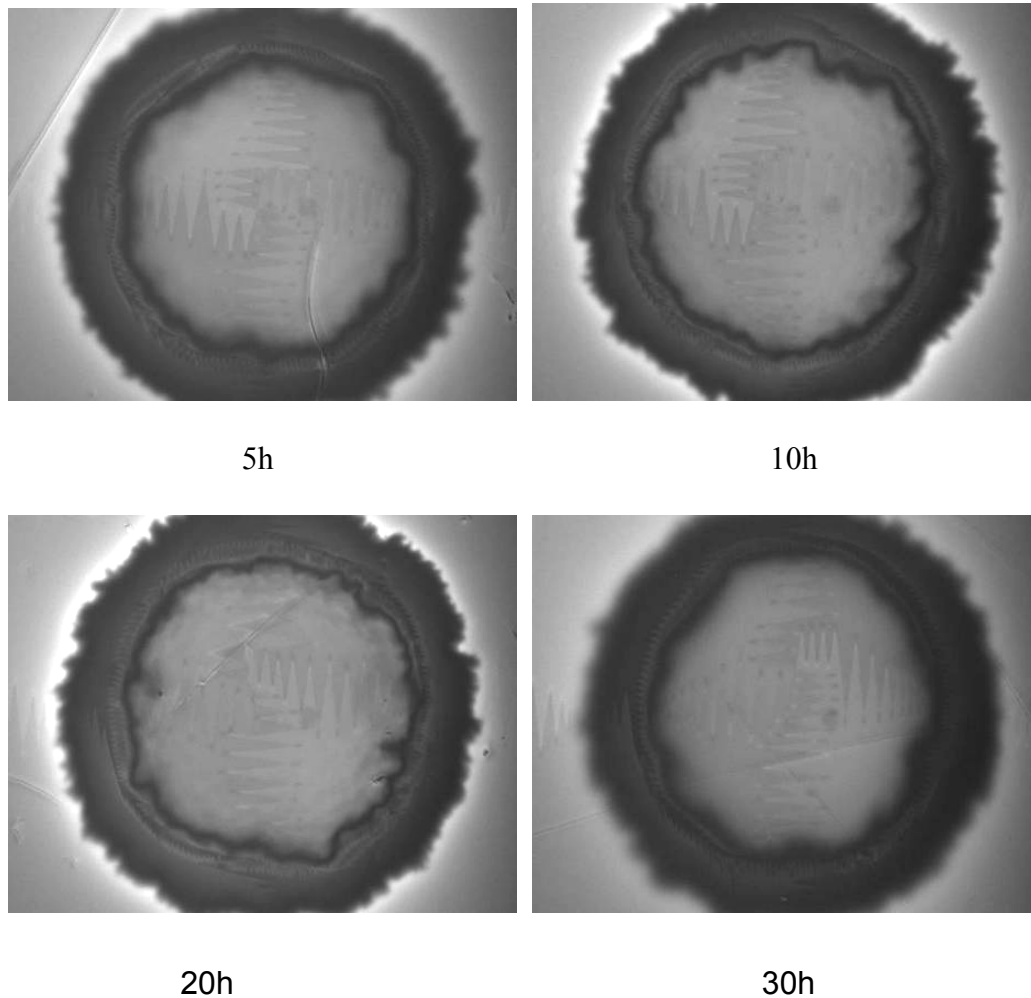


Figure 3-21 MOI of the samples heat-treated at 800 °C for different time from 5 hours to 30 hours

The results show that there is an obvious interface between Nb and MgB₂ core in each sample, but the difference among those images is not clear. This may be due to the rapid reaction of Mg-B system and MgB₂ formation at high temperature, thus there is no enough B left for Nb-B reactions while the dwelling time prolonged. The color of Nb ring is darker than that in the central region, which means the trapped flux density is higher in MgB₂ core than that in Nb layer. The bright ring in the outside region for each sample is also due to the magnetic field of the trapped flux in Nb and MgB₂.

3.5.3 Phase formation at MgB₂-Nb interface

There are six niobium borides phase (NbB₂, Nb₂B₃, Nb₃B₄, Nb₅B₆, NbB, and Nb₃B₂) based on the Nb-B phase diagram in Figure 3-22 ^[111]. They are all

stoichiometric proportion intermetallic compounds with fixed composition except NbB₂. NbB₂ is a nonstoichiometric proportion intermetallic compounds that has a range of compositions. Because the Nb-B atom ratio is not fixed, NbB₂ can contain from 66 at.% to 70 at.% B at approximately 1000 °C.

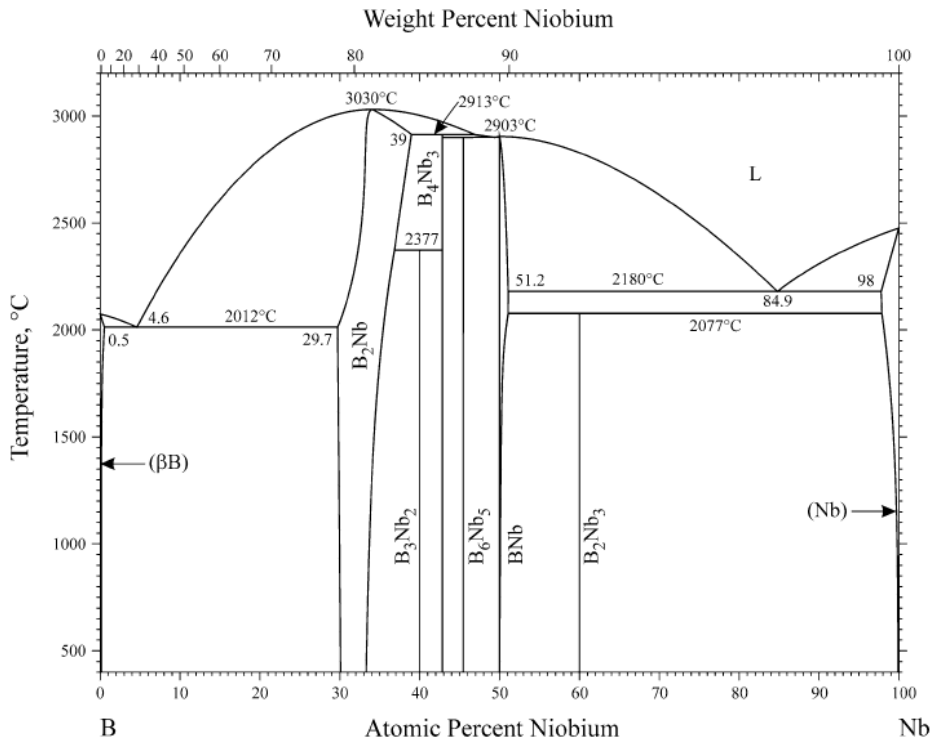


Figure 3-22 B-Nb phase diagrams

The mono-filamentary MgB₂ wire was rolled to a tape with 3.2 mm in width and heat treated at 950°C for 2 hours, and then mechanically peeling off the sheath material and remove the powder for the XRD measurement. As shown in Figure 3-23, the main phase of Nb sheath, as well as second phase of NbB, appears in the samples and the content of NbB is around 5%. That means there have formed the NbB phase while heat treated the sample at higher temperature such as 950°C. This diffusion layer is not superconducting phase and causes the current can not transfer to the MgB₂ cores.

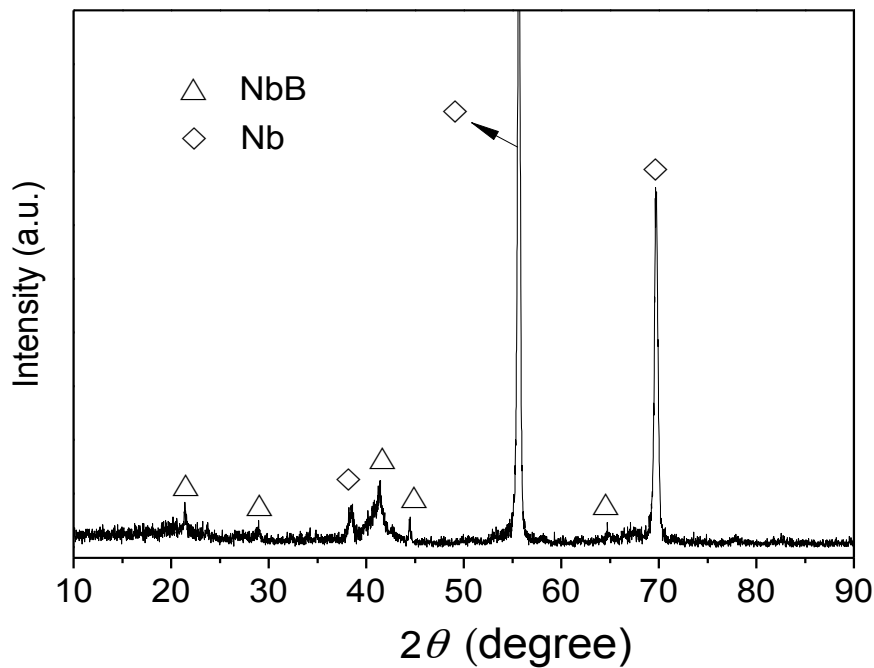
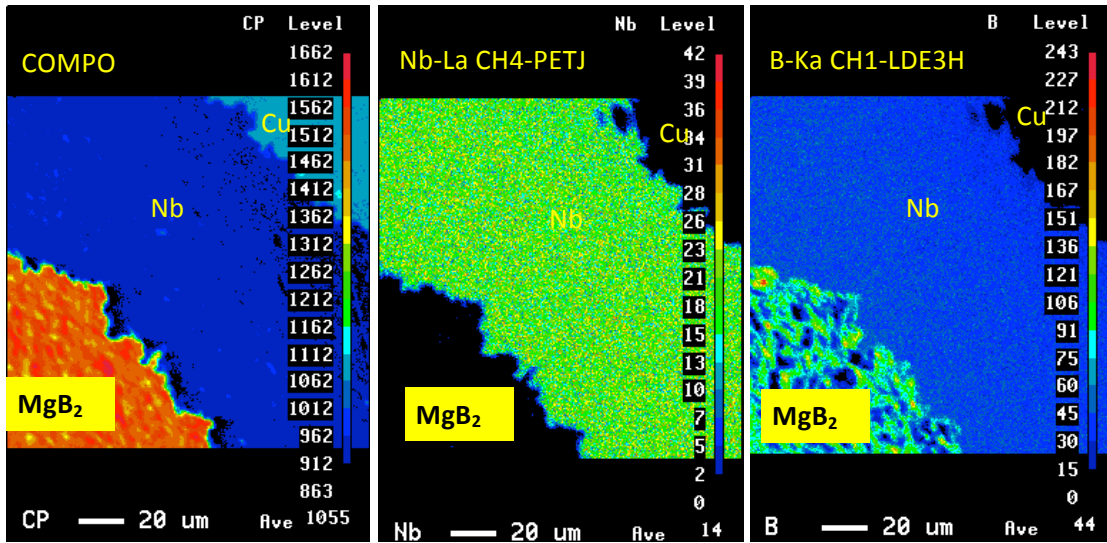


Figure 3-23 XRD pattern of MgB₂-Nb interface

3.5.4 Electron Probe Micro-Analysis of MgB₂-Nb interface

In this work, EPMA was used to analyze the chemical composition of MgB₂ wires. By EPMA, low amounts of B in Nb sheath were measured in the samples heat treated at higher temperature. The sample was prepared for EPMA by embedding in resin, and then it was grounded and polished. A Jeol Superprobe 8900R was used to analyze EPMA properties in Institut Neel, CNRS, Grenoble. The results are shown in Figure 3-24 and Figure 3-25.

Analyses of light elements (such as Be, B, C, N, etc) are the demanding task for the electron-beam techniques. In Electron Probe Micro Analysis (EPMA), peak shifts can occur between standard specimens and the samples due to the absorption of the K-lines of light elements by heavier elements, yielding to the modified acquisition conditions with respect to heavy elements^[112]. Moreover, porosity and surface roughness are detrimental factors to obtain reliable quantitative data.



(a)

(b)

(c)

Figure 3-24 EPMA element maps for niobium (b) and boron (c) of the MgB₂/Nb/Cu wires heat treated at 900 °C

Figure 3-24 shows the distribution maps of B, Nb and Cu in the interfacial region of MgB₂/Nb/Cu wires heat treated at 900°C. As mentioned above, this wire does not display transport critical current at all when the temperature is higher than 9.2 K which is the critical temperature of Nb. The decreased boron content can be seen in the Nb sheath in the Figure 3-24(c), which indicates there are at least a few atomic percents of B diffusion into Nb sheath and form the interfacial phase.

Figure 3-25 is the EPMA line scanning at the interfacial region, with the vertical axis is the weight percentage for each component elements. The content of Mg and B displays exponential type distribution in the diffusion direction. The result shows that the diffusion layer is just a few microns thick. The summation of each component element is show in Figure 3-25(b). Lower values exist at the interface because there are more holes and lack of the boron. The presences of these holes reduced the combination of the superconducting core and Nb sheath. Consequently, the transfer current decreased with increasing hole density.

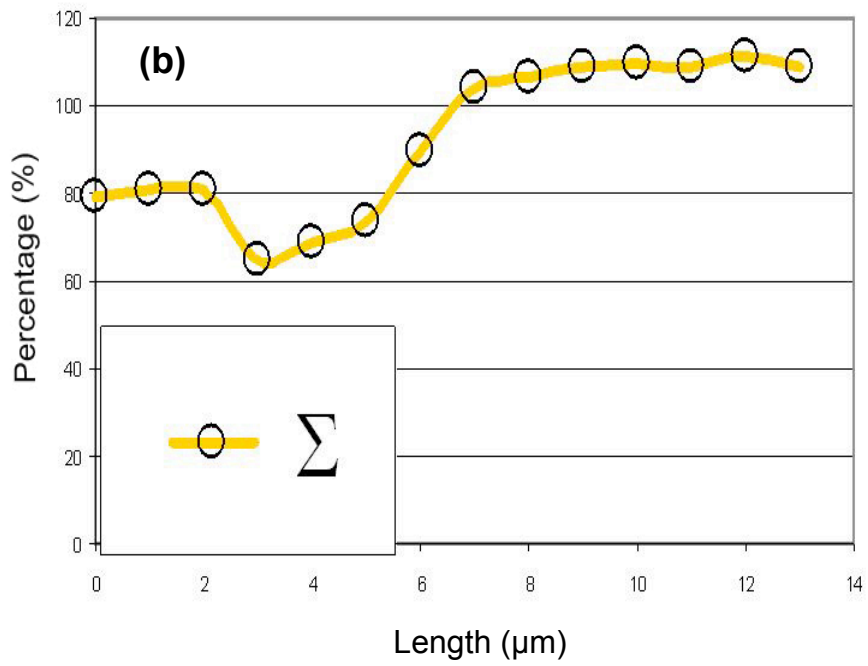
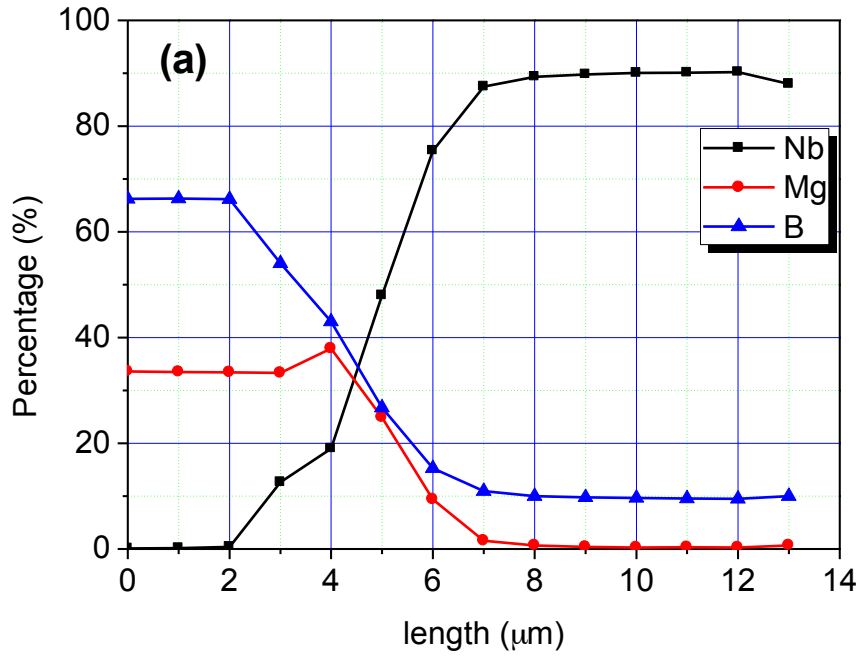


Figure 3-25 EPMA line scanning of MgB_2 -Nb interface in MgB_2 wires heat treated at $900\text{ }^\circ\text{C}$

3.6 Conclusion

In this chapter, the monofilament MgB_2 wires with Nb/Cu composite tube as the sheath are fabricated by *in-situ* PIT technique and heat treated from 600°C to 950°C for 2 hours. The influences of sintering temperatures on the superconducting properties of the $\text{MgB}_2/\text{Nb}/\text{Cu}$ wires have been systematically investigated. And the phase formation processes and microstructures of the diffusion layer between MgB_2 and Nb, which exhibited severe effect on the degradation of superconducting properties, have also been observed and studied. The XRD analysis show that all the samples heat treated at different temperature contain the MgB_2 phase as the main phase. The heat treatment temperature does not effect on the lattice parameter of MgB_2 , but the crystallinity increases with increasing heat treatment temperatures. Transport resistance test and the magnetization measurements also indicate that the wire is in superconducting state.

However, the transport critical current measurements did not show superconducting current of MgB_2 at all for the sample heat treated at 750°C or higher heat treatment temperature. Therefore, we carried out the study on the microstructures and phase formation process of the interface layer between MgB_2 superconducting core and Nb sheath. The results show that there is a diffusion layer at this region which is composed of non-superconducting phase for the sample heat treated at high temperature, and this diffusion layer obstructs the current transmission. This diffusion layer has obvious effects on the critical current of MgB_2 wires heat treatment at high temperature and the best heat treatment temperature for the MgB_2 wires with Nb as the barrier layer should be lower than 750°C . Further more, the presences of holes at the interface between MgB_2 core and Nb also reduced the current transfer from Nb/Cu sheath to MgB_2 core.

CHAPTER 4

EFFECT OF CHEMICAL DOPING ON MgB₂/Nb/Cu WIRES

Chemical doping has not been employed in High Temperature Superconductor materials (HTS) due to their high anisotropy and short coherence lengths. In contrast, MgB₂ has a relatively large coherence length (around 4 ~ 5 nm) and slight anisotropy, similar with the Low Temperature Superconductor materials (LTS). This suggests that chemical doping can be used in this material.

Remarkable improvements of the critical current density (J_c) in MgB₂ can be obtained through chemical doping with carbon (C) containing composites or compounds, such as SiC, C, B₄C, carbon nanotubes (CNT), hydrocarbons, carbohydrates, etc. The C atoms can enter the MgB₂ lattice by substituting boron (B) sites, thus J_c and H_{c2} can be significantly enhanced due to the increased impurity scattering in the two-band MgB₂.

Several groups have already studied the effects of carbon or carbide doping on the superconductivity of MgB₂. However, their results showed that higher sintering temperature and long sintering time are required. In this chapter, the amorphous carbon and TiC were used as the dopants with a low temperature (~ 700°C) sintering procedure.

This chapter aims to compare the results of the C dopant with that of TiC dopant and establish their advantage and disadvantage. This will help us to determine their viability for properties enhancement, hence build a base for the study of kilometer level long MgB₂ wires.

4.1 Sample preparation

MgB₂ wires were fabricated by *in-situ* PIT process with Nb as the barrier and Cu as the stabilizer. The Mg (-325 mesh), submicron amorphous B, and submicron C or TiC with stoichiometry of MgB_{2-x}C_x or MgB_{2-x}(TiC)_x were mixed, where $x = 0, 0.05,$

0.08, 0.10 and 0.15, and the samples were named as 1 to 5, respectively. The mixtures were well mixed in vacuum glove box under argon atmosphere and grounded in agate mortar for 30 minutes. the Nb/Cu composite tubes were densely packed with these mixtures, and drawn to 1 mm in diameter. There was no annealing during the fabrication process. After cold deformation, the composite wires were cut into short pieces around 10 cm in length and sintered at different temperatures in a tubular furnace with pure argon, then furnace-cooled to room temperature.

Phase composition analysis was investigated by X-Ray Diffractometer after mechanically peeling off the Nb/Cu sheath and grinding the superconductor core into powders. Microstructures on the cross section of MgB₂ wire was observed by Scanning Electron Microscopy (SEM) with an Energy Dispersive Spectrometer (EDS). The critical temperature T_c measurements were carried out by a SQUID magnetometer. The transport critical currents were measured on 35 mm length wire by the standard four probe method at 4.2 K in various applied magnetic fields in LNCMI, Grenoble.

4.2 Phase formation of chemical doping MgB₂ wire

4.2.1. Influence of doping content on the phase formation

To investigate the mechanism of the enhancement of J_c at higher fields of these doping samples, it is necessary to research the phase composition and microstructures of samples treated at different temperatures and doped with different doping content.

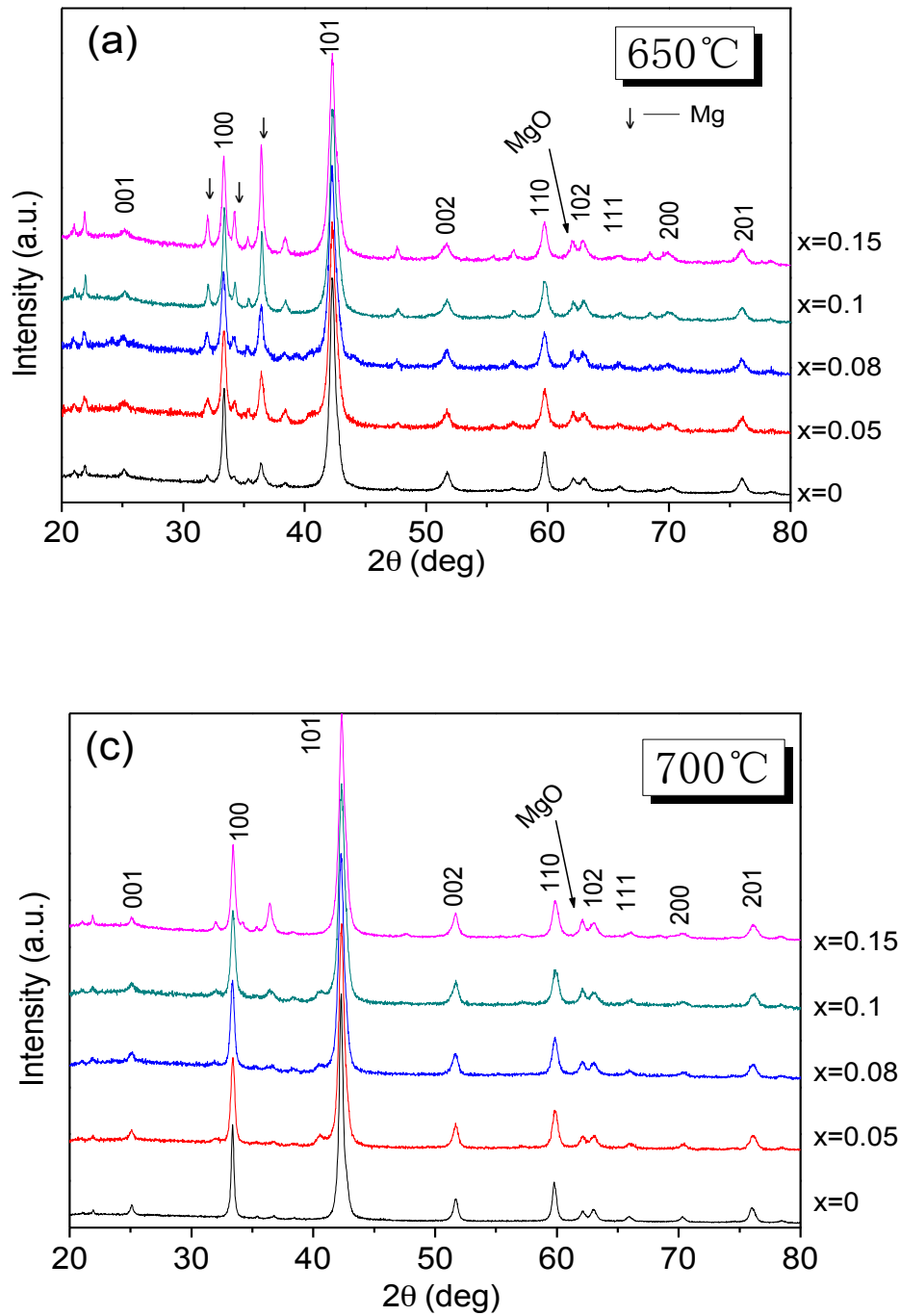


Figure 4-1 XRD patterns of MgB_{2-x}C_x (x = 0, 0.05, 0.08, 0.1, 0.15) wires heat treated at 650 °C (a) and 700 °C (b).

As can be seen from the XRD patterns, MgB₂ is the main phase accompanied with MgO as a second phase in all the *in-situ* reacted samples. Additional impurities Mg₂C₃ can be indexed in the doped samples. Some un-reacted Mg can always be

found in the samples treated at 650 °C. In addition, it can be noticed that the strongest peak ($2\theta = 42.412^\circ$) broadens with increasing the doping content, which indicates that the crystallinity of MgB_2 was depressed with increasing doping content.

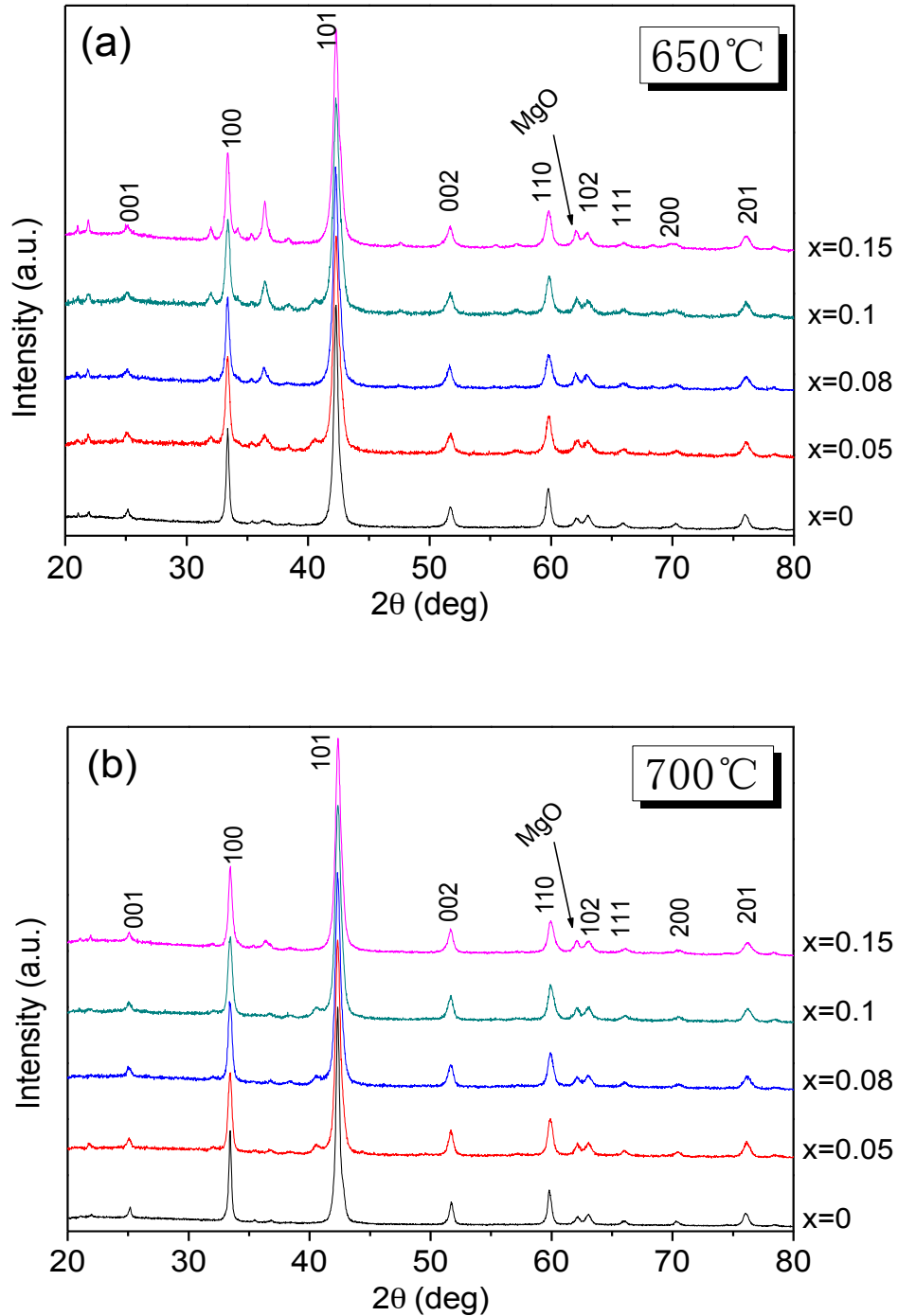
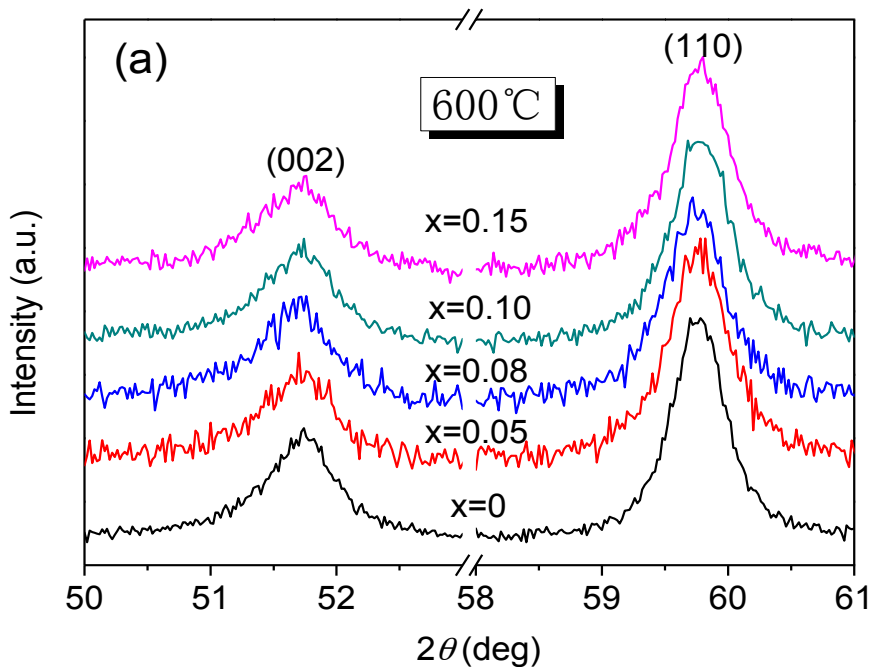


Figure 4-2 XRD patterns of $\text{MgB}_{2-x}(\text{TiC})_x$ ($x = 0, 0.05, 0.08, 0.1, 0.15$) wires heat treated at 650 °C (a) and 700 °C (b).

Figure 4.1 shows the X-ray diffraction spectra of $\text{MgB}_{2-x}\text{C}_x$ ($x = 0, 0.05, 0.08, 0.1, 0.15$) samples after heat treated at different temperatures. MgO and Mg contaminations are presented comparing with the as-received. Structural composition is possible changed by the different chemical doping. Figure 4-2 shows the XRD patterns of the reacted MgB_2 samples without or with TiC-doped at 650°C . As can be seen, all the samples show high-purity MgB_2 phase companied with MgO as a minor impurity phase. The samples sintered at 650°C display Mg similar as the C-doped samples at the same heat treatment. In samples 2~5, unreacted TiC can also be identified as impurities, especially in the samples sintered at 650°C .

The peak between $2\theta = 58^\circ \sim 61^\circ$ shifts towards higher 2θ values with increasing doping content, indicating the contraction of a axis in the crystal lattice. The peak between $2\theta = 50^\circ \sim 53^\circ$ remains unchanged with increasing doping content, which indicates that the distance between the B plane and the Mg plane would not be significantly affected by chemical doping. Figure 4-3 and Figure 4-4 show the negligible shift of (002) peak, which confirms the negligible change in the c -axis parameter.



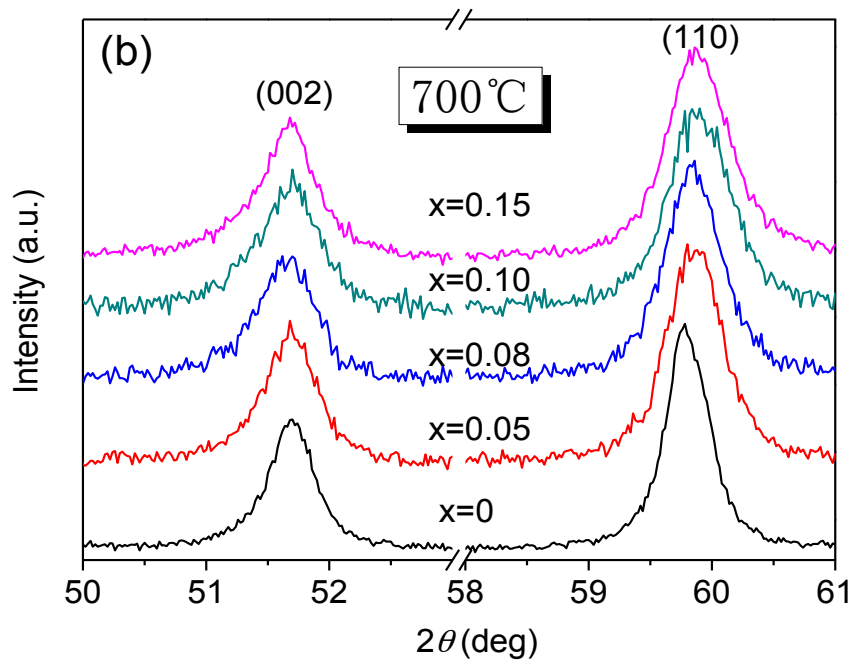
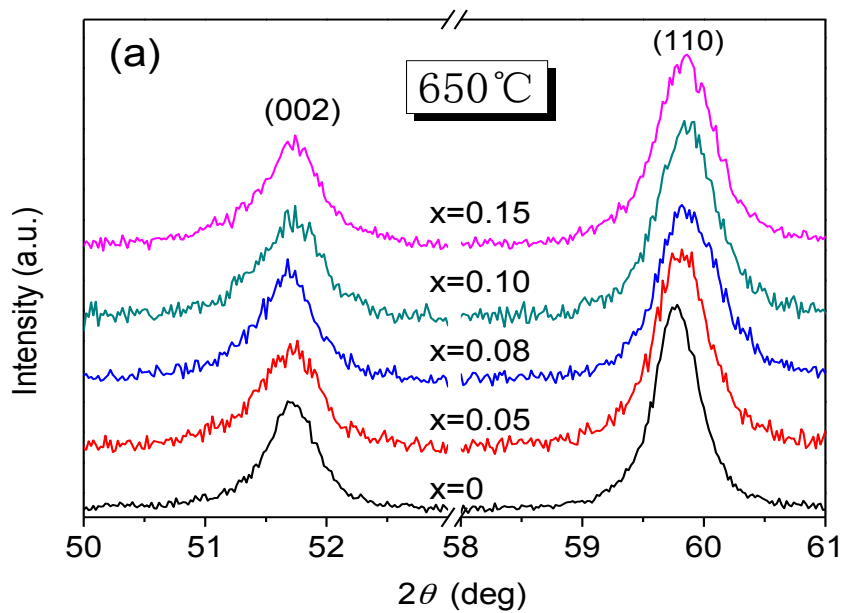


Figure 4-3 Comparison of (002) and (110) characteristics peak of MgB_{2-x}C_x wires

In Figure 4-3(a), there is not obvious shift of the (110) peak confirming the negligible decrease of *a* parameter. As the heat treatment temperature increased to 700°C, the shifting of (110) peak towards higher 2θ is easier than that of increasing doping content.



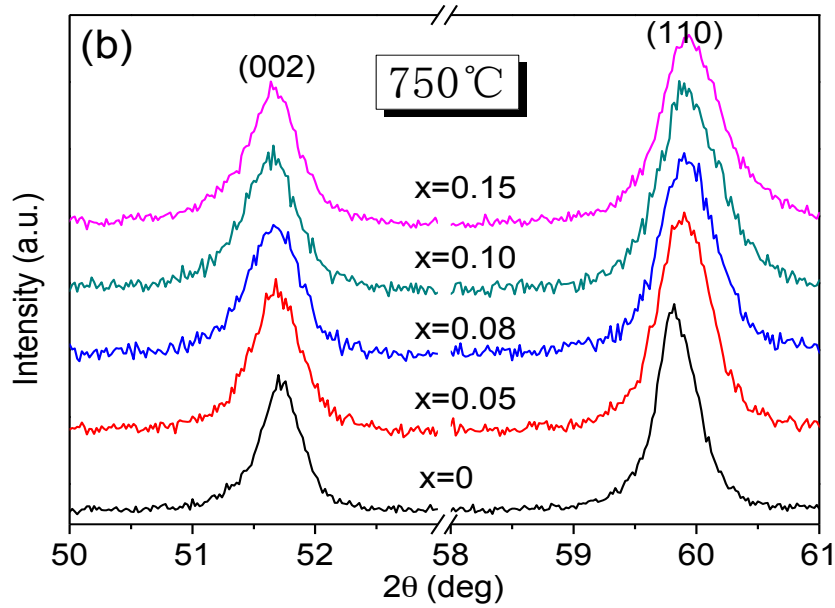


Figure 4-4 Comparison of (002) and (110) characteristics peak of $\text{MgB}_{2-x}(\text{TiC})_x$ wires

In Figure 4-4, the position of (002) peak is also not changed by TiC doping, whereas the (110) peak shifted to higher 2θ angle. In Fig. 4-4(a), obvious shifts of (110) peak can be observed towards higher 2θ value. Compared the shift of (110) peak, the shift in TiC-doped samples is easier to take place, which indicates that the optimal doping effect can be achieved by TiC doping at lower temperature.

Comparing the lattice parameters a and c of MgB_2 powders with C and TiC dopants, a decrease tendency of the lattice parameters with increasing doping content was observed. The values of the lattice parameters for ideal MgB_2 are $a = 3.083 \text{ \AA}$ and $c = 3.521 \text{ \AA}$. It can be seen that lattice parameters a and c of undoped sample in the reference are greater than the ideal values. This indicates that a large amount of vacancies exist in the undoped sample. The existence of these vacancies relaxes the lattice around them and increases both a and c lattice parameters. When the sintering temperature is 650°C , although C or TiC is doped into sample 4, lattice parameters a and c of the sample are still greater than the ideal values. From the XRD analysis, there is still some Mg existing, which results insufficient magnesium reacting with boron in the reacting process. The unreacted magnesium could be responsible for the vacancies. When the sintering temperature is higher than 650°C , lattice parameter a

becomes smaller than the ideal values for the C and TiC doping samples. It indicates that C atoms have replaced part of the boron atoms. Meanwhile, it can also be noticed that at the same sintering temperature and the same doping content, lattice parameters a in the TiC doping samples are smaller than that in the C doping samples. So the substitution for B by C coming from the decomposing of TiC is easier to take place in MgB_2 .

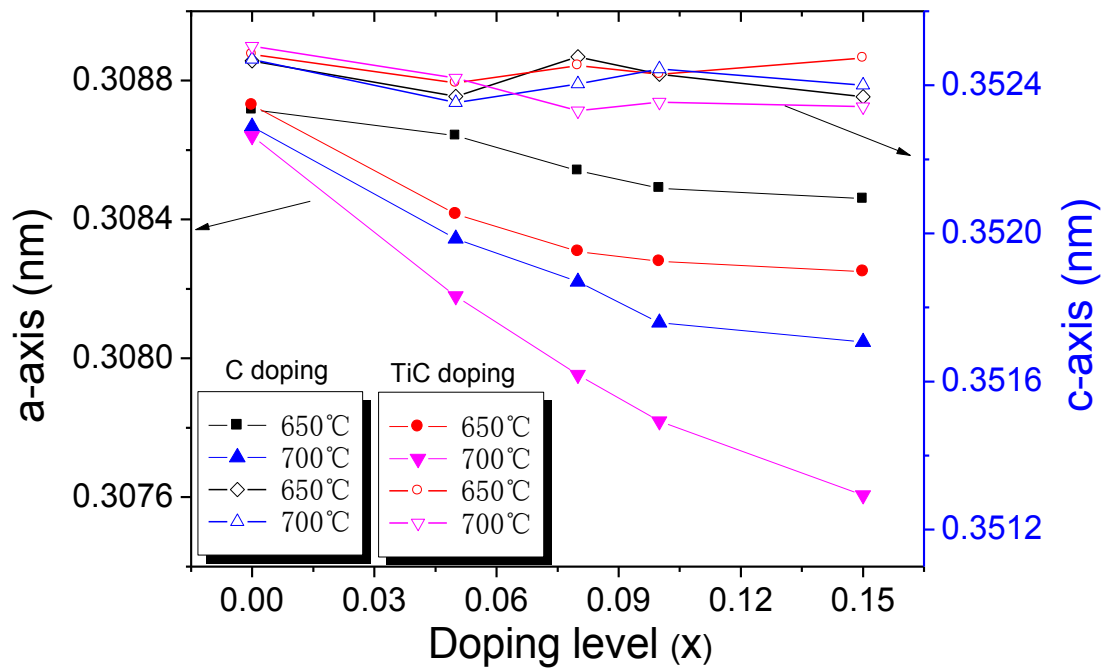


Figure 4-5 Crystal parameters of $\text{MgB}_2/\text{Nb}/\text{Cu}$ wires with TiC and C doping

4.2.2. Influence of sintering temperature on the phase formation

Reaction between Mg and B starts at the temperature below the melting point of Mg. With the increase of annealing temperature, Mg starts to react with B and MgB_2 can be obtained. The reaction between Mg and B powders starts at the Mg-B interface and a layer of MgB_2 forms firstly at the interface^[106]. At the reaction temperature Mg melts but remains as globules and exists as particles in liquid phase. Mg and B particles diffuse into the formed MgB_2 layers and MgB_2 grains grow larger, until the growth is pinned chiefly by pores.

The samples were heat treated with different sintering temperatures from 600°C to 950°C. Figure 4-6 shows the powder XRD spectra of $\text{MgB}_{1.92}(\text{TiC})_{0.08}$ samples synthesized for 90 minutes at different temperatures: 600, 650, 700, 750, 800, 850, 900 and 950°C.

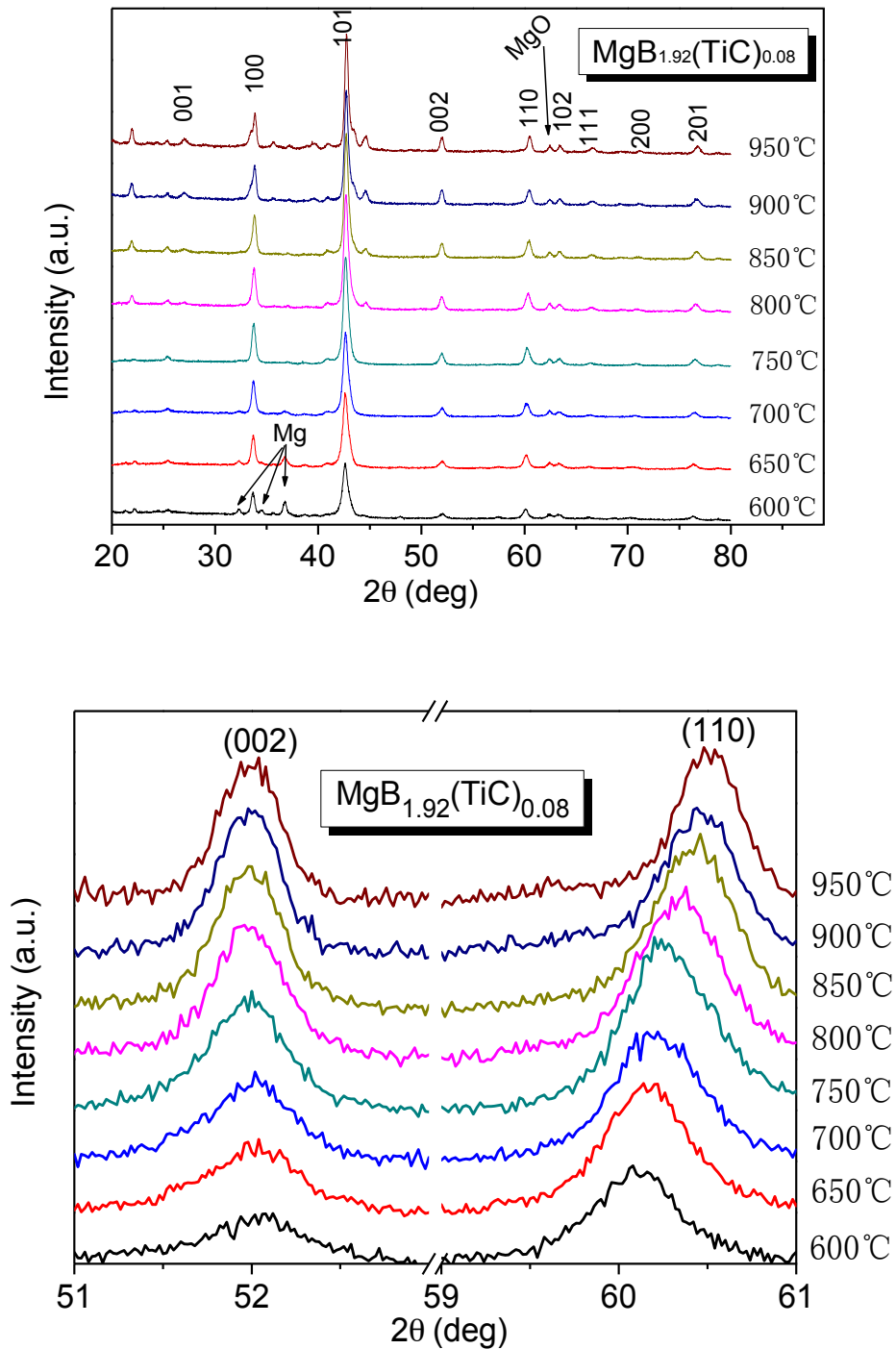


Figure 4-6 XRD pattern of $\text{MgB}_{1.92}(\text{TiC})_{0.08}$ heat treated at different temperatures

Figure 4-6 shows the X-ray diffraction patterns of the $\text{MgB}_{1.92}(\text{TiC})_{0.08}$ sample heat treated at different temperatures. MgB_2 phase forms at this temperature region. It is observed that the samples heat treated at 600°C and 650°C contained unreacted Mg, whereas traces of Mg are not visible in the XRD patterns of the samples treated at 700°C to 950°C . However, impurity MgB_4 and other amounts of unidentified impurity phases increased with increasing synthesis temperature. So it does not need for the synthesis temperature to be too high temperature for the fabrication of MgB_2 . It is suitable to fabricate MgB_2 wires at temperature lower than 800°C .

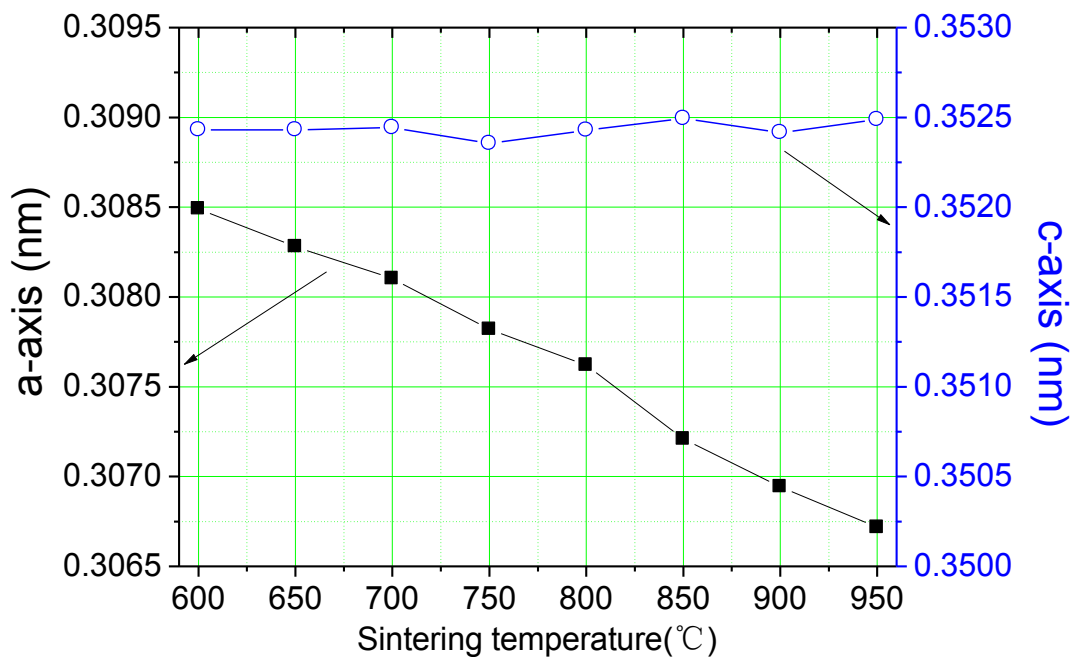


Figure 4-7 Lattice parameter of $\text{MgB}_{1.92}(\text{TiC})_{0.08}$ wires heat treated at different temperatures

The unit cell volume of MgB_2 is calculated according to the refined lattice parameters a and c . The refined results are listed in Figure 4-7. The lattice parameter a decreases obviously with increasing synthesis temperature at the same doping content and the change of a is an evidence of C substitution for B in MgB_2 lattice. It indicates that the increasing temperature improves the intergrain connectivity, and reduces the vacancies.

4.3 Microstructure of chemical doping MgB₂ wire

The microstructure of the sample is shown in Figure 4-8. Densely stacked MgB₂ is observed in the fractured cross sections, as seen from the left image. In the right image, a large fraction of white points are present, indicating that C atoms distribute in the MgB₂ matrix homogeneously.

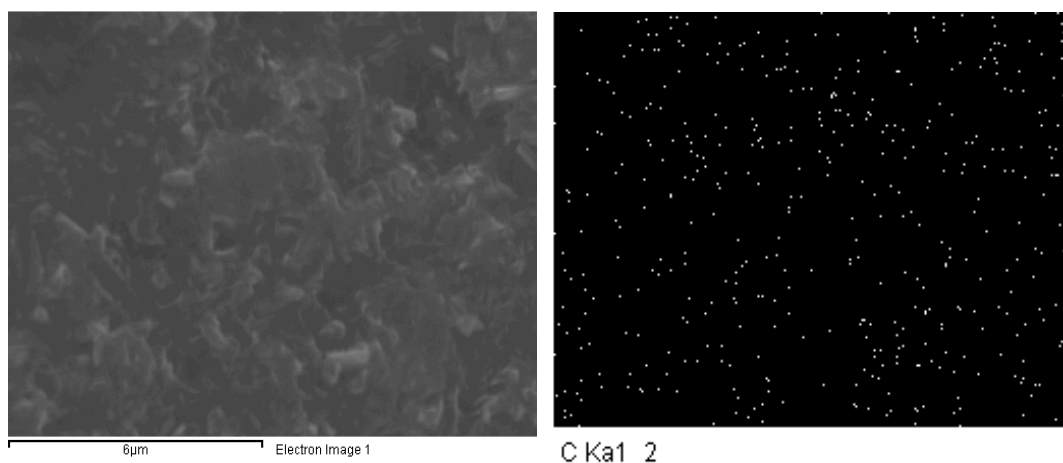


Figure 4-8 Second electron image of MgB_{1.92}(TiC)_{0.08} wires heat treated at 700 °C

4.4 Superconductivity of chemical doping MgB₂ wire

4.4.1 The *M-T* performance of chemical doping MgB₂ wire

The magnetization properties of the samples measured using SQUID shows the variation the superconducting transition temperature. In order to optimize the sintering temperature, samples doped from 0.05 to 0.15 were heat-treated between 600 °C to 950 °C and compared to pure sample.

Figure 4-9 shows magnetization for sample with 0.08 doped. According to this result, the critical transition temperature T_c decreases when the annealing temperature increases to 950 °C. The T_c decrease might be a result of increased impurity phases introduced by increasing temperatures. Therefore, the results of XRD measurements are in agreement with the *R-T* measurements. The sample heat-treated at 700 °C and 750 °C shows a sharper transition than that annealed at any other temperature, indicating a good homogeneity of the sample annealed at 700 °C and 750 °C. This

demonstrates that the synthesis of the samples at 700 °C and 750 °C is useful for enhancing the quality of MgB₂. Hence, there is an optimal sintering temperature between 700 °C and 750 °C.

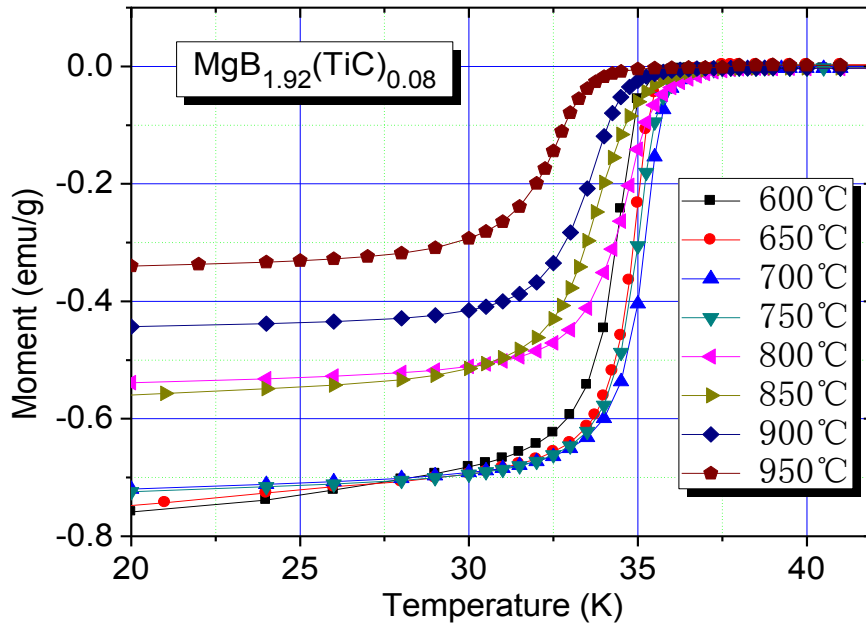


Figure 4-9 Magnetic moment as a function of temperature on MgB_{1.92}(TiC)_{0.08} wires heat treated at different temperatures

The effects of the annealing temperature on the critical transition temperature and the doping content on the critical transition temperature are shown in Figure 4-10. Figure 4-10(a) demonstrates the T_c dependence of the sintering temperature. It can be seen that as the temperature increases, T_c of the pure samples become high, whereas, T_c of the doped samples decrease with the nominal TiC content increasing. Figure 4-10(b) shows the T_c dependence of the doping content. The overall trend observed was a decrease in T_c with the doping content increasing. So the optimum selection for preparation MgB₂ wire is the middle sintering temperature and the middle doping content.

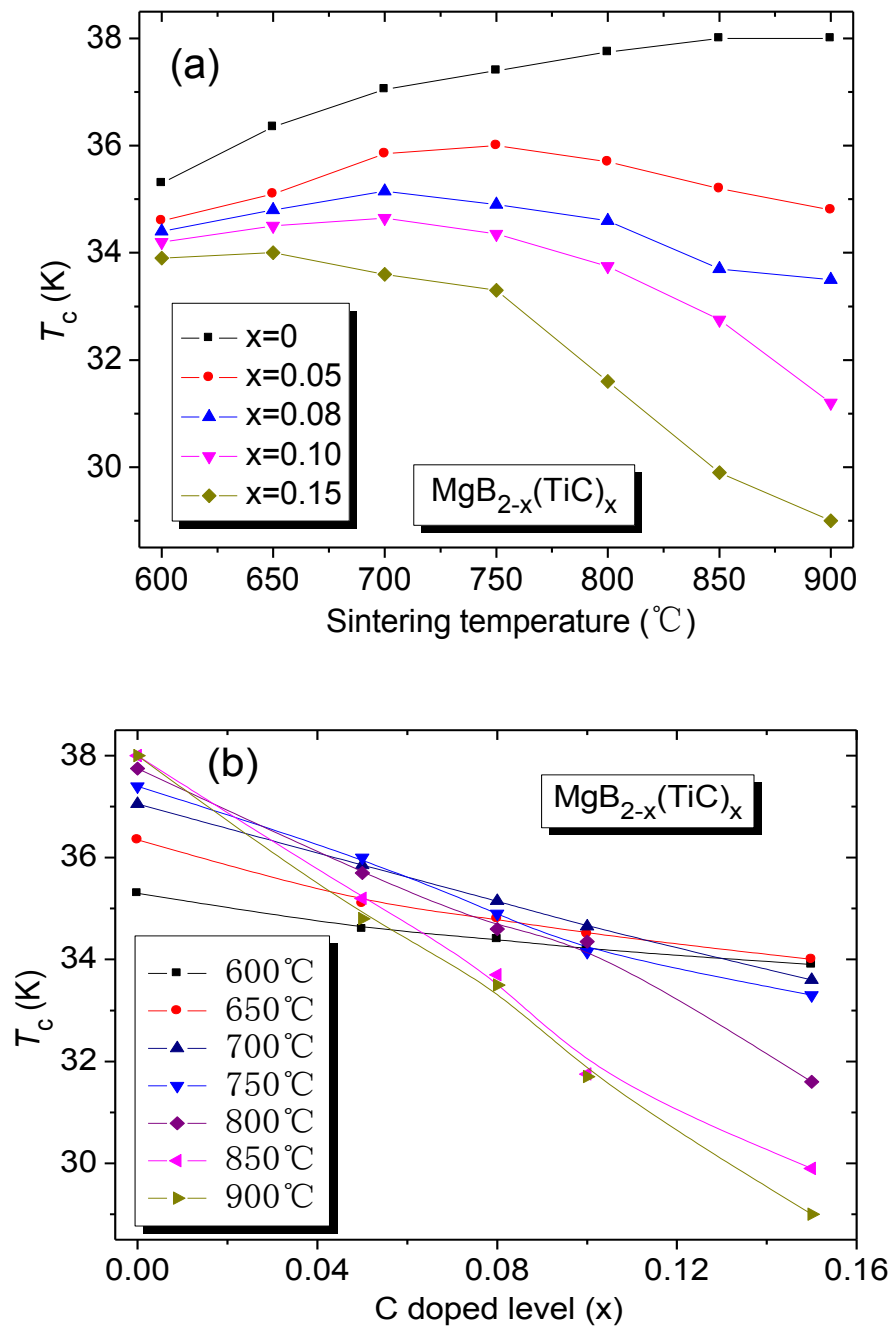


Figure 4-10 Critical temperature as a function of doping content on $\text{MgB}_{1.92}(\text{TiC})_{0.08}$ wires heat treated at different temperatures

4.4.2 The R - T performance of chemical doping MgB_2 wire

In addition to proper phase formation, it is important to know if the phases formed have the expected superconducting properties within the grains and that the grains are substantially connected. To prove this, resistive T_c measurements were

performed using the four probe technique. The transition width is correlated to the purity of the sample, and a complete transition to the superconducting state for these polycrystalline samples indicate some content of connectivity.

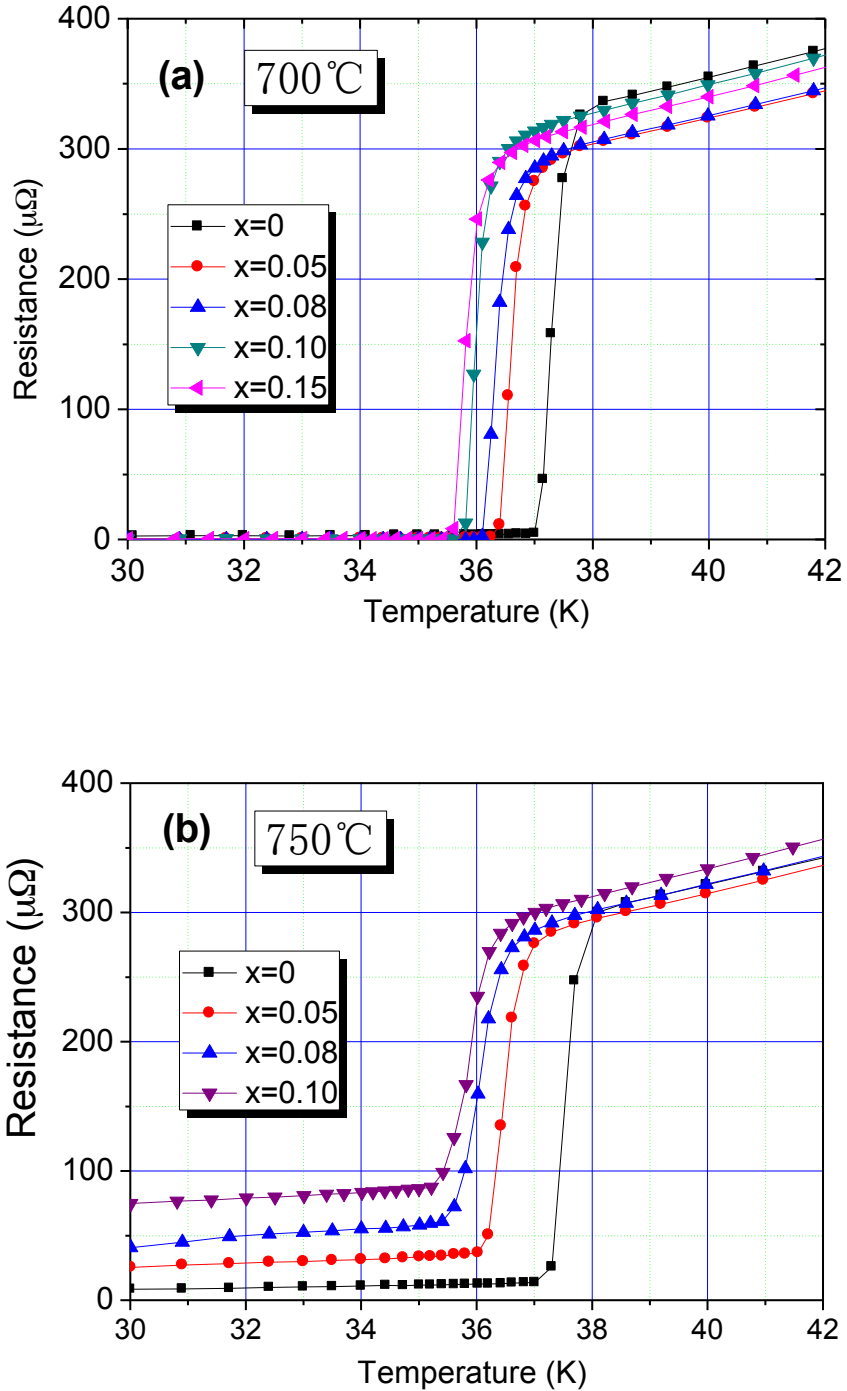
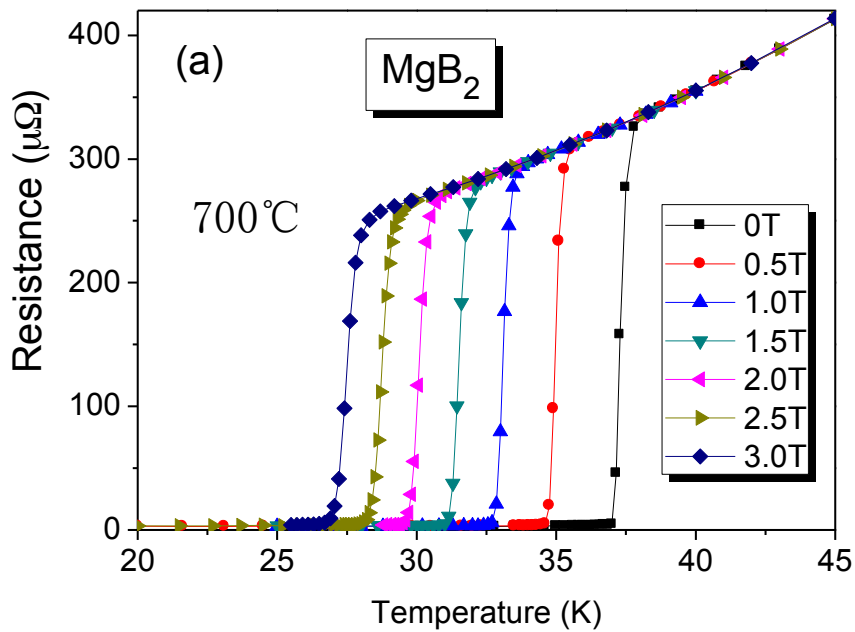
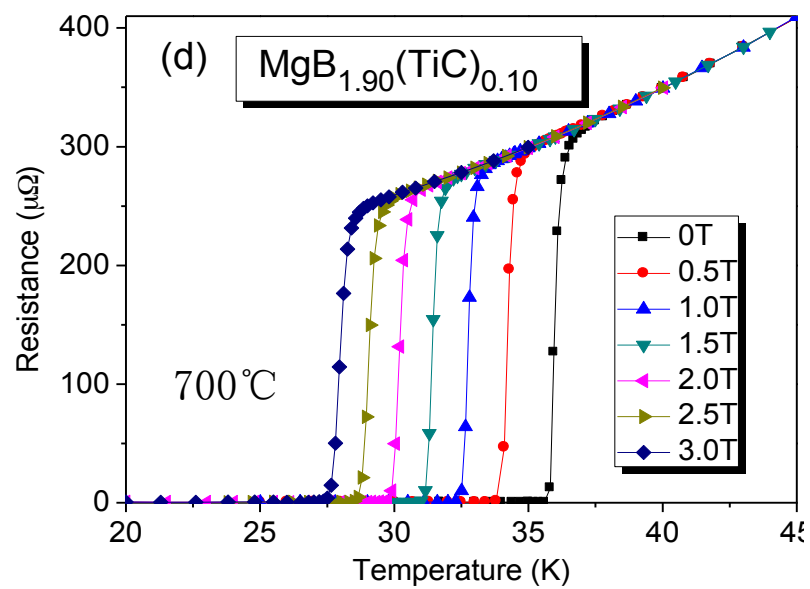
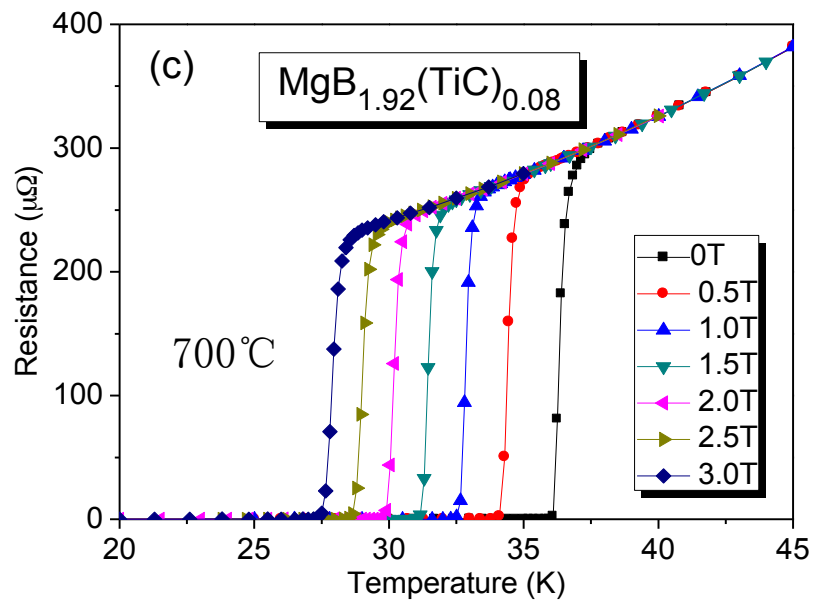
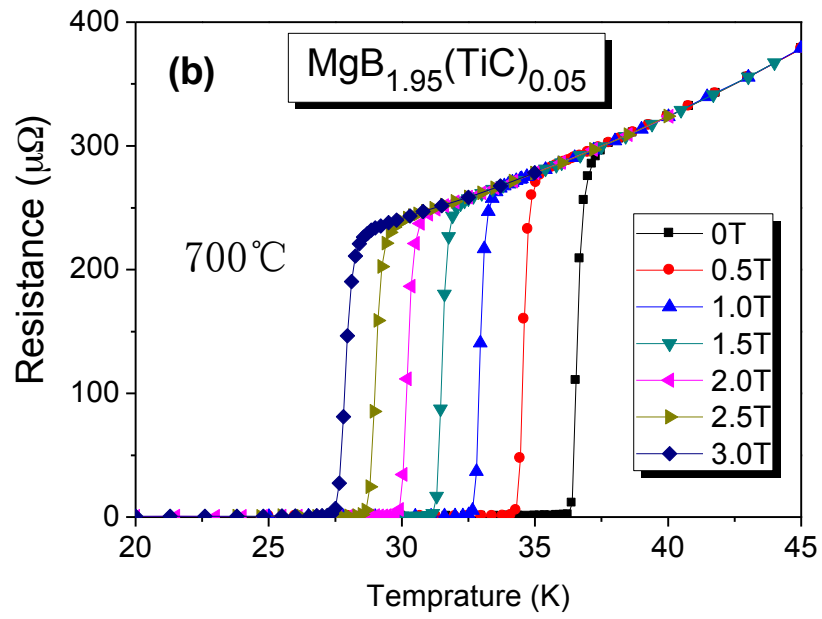


Figure 4-11 Resistance depend on the temperature of MgB_{2-x}(TiC)_x wires heat treated at 700 °C (a) and 750 °C(b).

Figure 4-11 shows the resistivity of the composite materials ($\text{MgB}_{2-x}(\text{TiC})_x$) as a function of doping content. The critical temperature of the undoped sample sintered at 700°C for 90 minutes were measured as $T_{c \text{ onset}} = 38.2 \text{ K}$, and $T_{c \text{ zero}} = 37.4 \text{ K}$. The T_c value of sample 5 decreases to 35.85 K with the increasing nominal TiC content. It can be concluded from Figure 4-11 that T_c decreases with increasing the doping content. This decrease of T_c is the sign of depressed crystallinity. With the sintering temperature further increase to 750°C , the critical temperature increases unmarkedly. Sample 4 annealed at 700°C shows a sharper transition with a narrow width of 0.9 K than that annealed at 750°C . This indicates that the crystallinity is much better in the sample heat treated at 700°C .





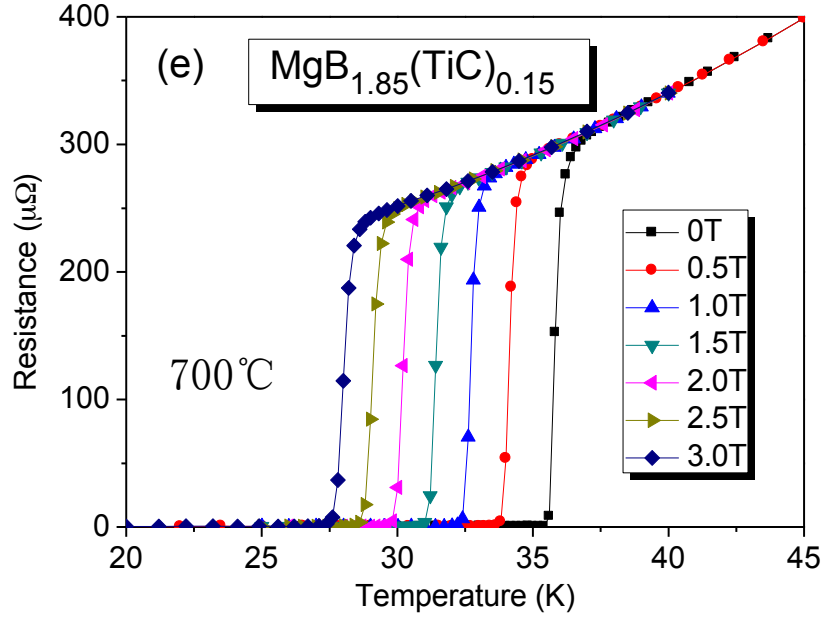


Figure 4-12 Field dependence of the R-T curves of the $\text{MgB}_{2-x}(\text{TiC})_x$ wires in 3.0 T, 2.5 T, 2.0 T, 1.5 T, 1.0 T, 0.5 T and 0 T from left to right in perpendicular fields

Figure 4-12 shows the T_c curves under different magnetic fields for the samples with various doping contents heated at 700°C . The T_c value of the pure samples varies from 27 to 37.5 K with the field increase from 0 to 3 T. Even though T_c is slightly lower than 39 K, Sample 1 under 3 T still exhibits a sharp superconducting transition within the ΔT value of 1 K. With different doping contents, the overall resistivity of a series of wires does not change drastically. Meanwhile, T_c values slightly decrease with increasing the doping content. ΔT_c in all the samples is sharp, with a width of ~ 1 K. This indicates that the MgB_2 phase is significantly homogeneous in all these wires.

The critical temperature T_c values under different magnetic field for the MgB_2 doped with different contents were analyzed. The reported T_c value for MgB_2 undoped is 39 K, however, the contaminations by oxygen or other elements or compounds can lead to the decrease of T_c value, in addition to some syntheses processes.

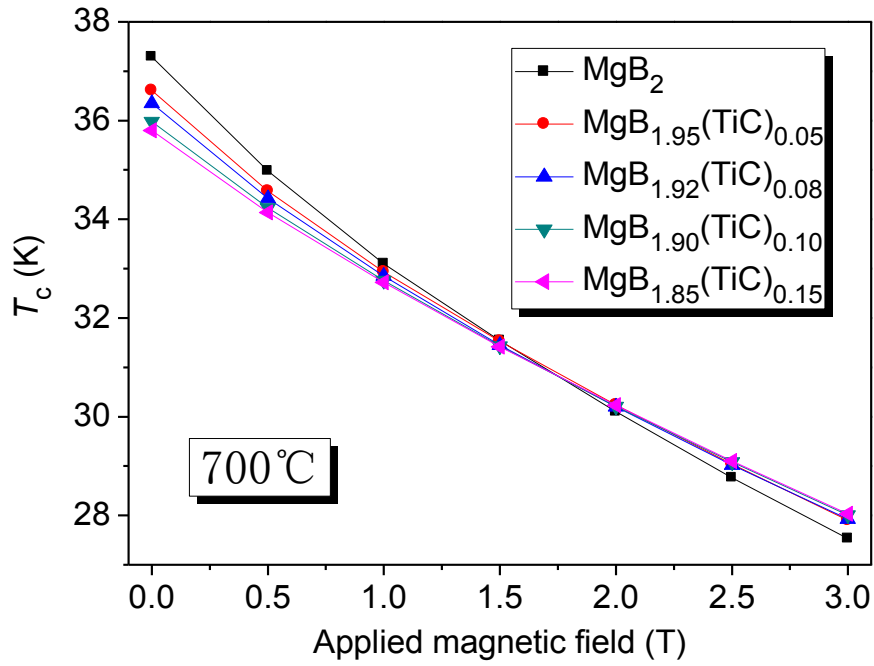


Figure 4-13 T_c versus magnetic field of MgB₂ wires with TiC doping

Figure 4-13 shows the graph of T_c versus magnetic field for MgB₂ samples with different contents. The overall trend was a decrease in T_c values with increasing external field. While the effect of different doping contents on T_c values is not obvious under the same fields.

4.4.3 The M - H performance of chemical doping MgB₂ wire

Figure 4-14 shows the magnetic hysteresis loops obtained at different temperatures. Figure 4-15 shows the field dependent magnetic $J_c(H)$ curves for the MgB_{1.92}(TiC)_{0.08} samples. The circular cross sections of the MgB₂ wires are 1 mm in diameter and the lengths of the wires from 7.5 mm to 10 mm. The magnetic J_c of the samples was calculated with the formula from the Bean critical state model as follow

$$J_c = \frac{30\Delta M}{v \times d} \quad (4-1)$$

where ΔM is the width of the hysteresis loop in emu; v is the volume of the MgB₂ superconductor in cm³; d is the diameter of MgB₂ superconductor perpendicular to the field direction in cm.

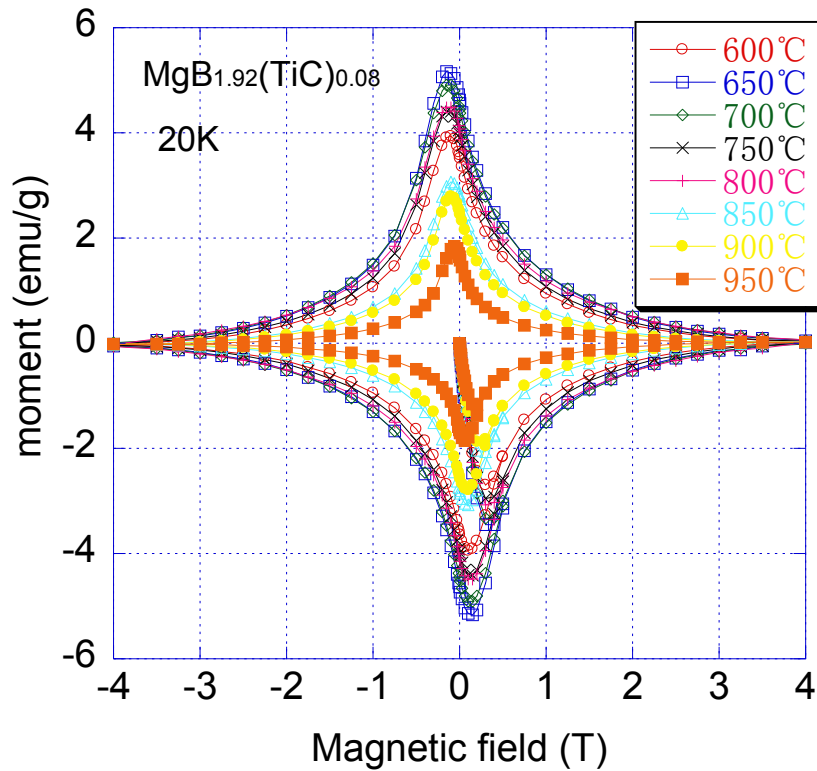


Figure 4-14 M - H curves of the $\text{MgB}_{1.92}(\text{TiC})_{0.08}$ wires heat treated at different temperatures

The variation of magnetization with applied field and the sintering temperature for these samples strongly suggests that the processing temperature has a significant effect on the critical current density due to enhancement of grain boundary by small grain size or defects/dislocations created by carbon substitution. The M - H curves measured at 20 K clearly show that the high sintering temperature depresses magnetization substantially in the whole field range from -5 T to 5 T. Sintered at 850, 900 and 950°C, magnetization decreases of about 40%-50% comparing with the value of the sample sintered at 650°C, indicating that increasing heating temperature does not enhance J_c , even in the high field region.

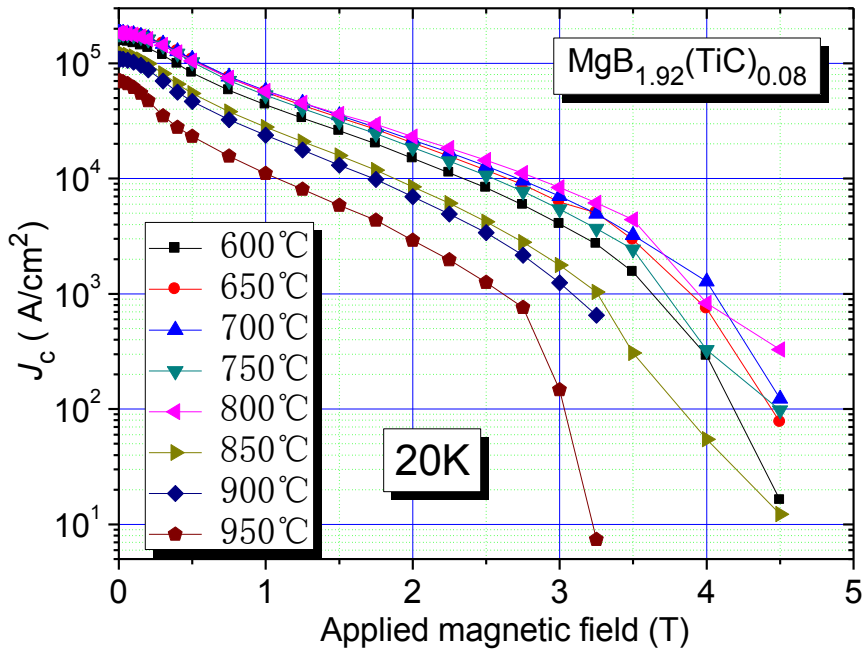


Figure 4-15 Magnetic J_c versus applied field for the $MgB_{1.92}(TiC)_{0.08}$ wires at different temperatures

It is clear that the sample sintered at $800^\circ C$ exhibited the maximum J_c at the field less than 3.75 T at 20 K, followed by the sample sintered at 700, 650 and $750^\circ C$. This means that sintering temperature low than $800^\circ C$ is the optimum heating condition in current processing conditions.

The J_c curves were also used to calculate the flux pinning force for these samples by the formula as follow

$$F_p = \mu_0 J_c(H) B \quad (4-2)$$

where μ_0 is the magnetic permeability in vacuum.

Figure 4-16 shows the dependence of reduced flux pinning force ($F_p/F_{p,max}$) of all the doped samples at different sintering temperatures. Flux pinning curves for the doped samples are shifted to higher magnetic field while compared with pure sample MgB_2 . This suggested a significant improvement in flux pinning force for TiC-doped samples in comparison to the undoped one.

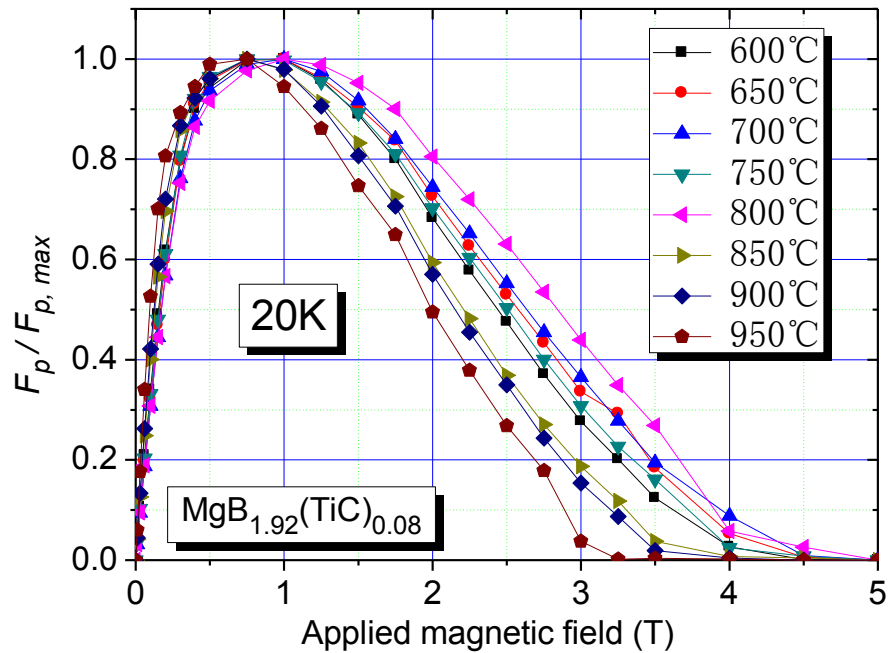


Figure 4-16 Normalized flux pinning force as a function of magnetic field at 20 K for the pure and TiC doped samples sintered at different temperatures.

Flux pinning curves for the samples sintered at the temperature lower than 950°C are shifted to the right comparing with the sample sintered at 950°C. This indicates the significant improvement in flux pinning forces for the samples sintered at temperature lower than 950°C in comparison to the sample sintered at 950°C. The samples sintered at lower temperature have more effective pinning center. More nanodomain structures were formed due to the substitution of C at B site at the suitability sintering temperature.

4.4.4 The J_c - B performance of chemical doping MgB₂ wire

Figure 4-17 shows the magnetic field dependence of J_c for undoped and TiC-doped samples. It can be seen that doping has strong effects on the improvement of J_c . At 4.2 K and 6 T, sample 4 shows one order of magnitude improvement. J_c of the pure sample drops more rapidly at higher field. Moreover, the parameter a of the TiC-doped sample is obvious smaller than that of the pure sample. So lattice distortion has a significant influence on the J_c behavior.

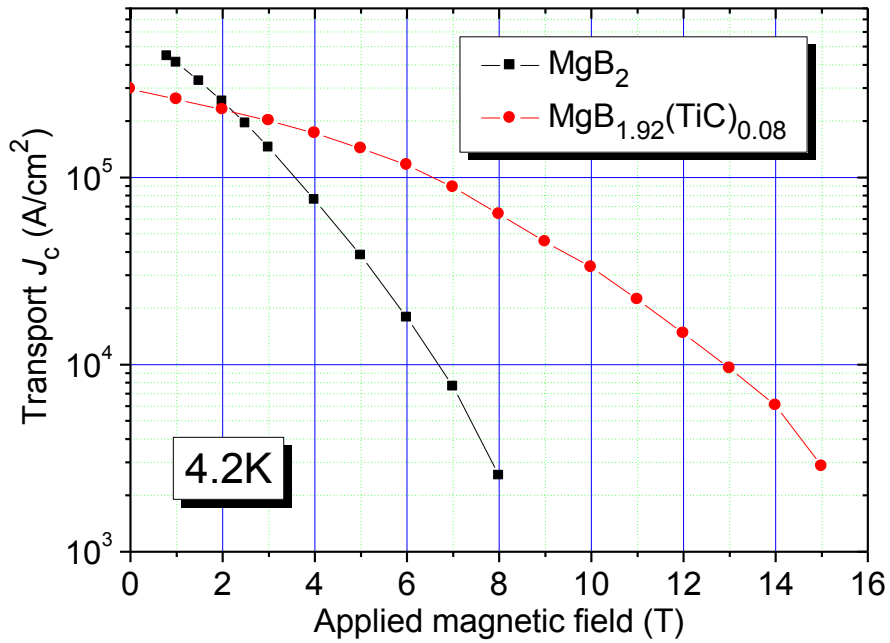
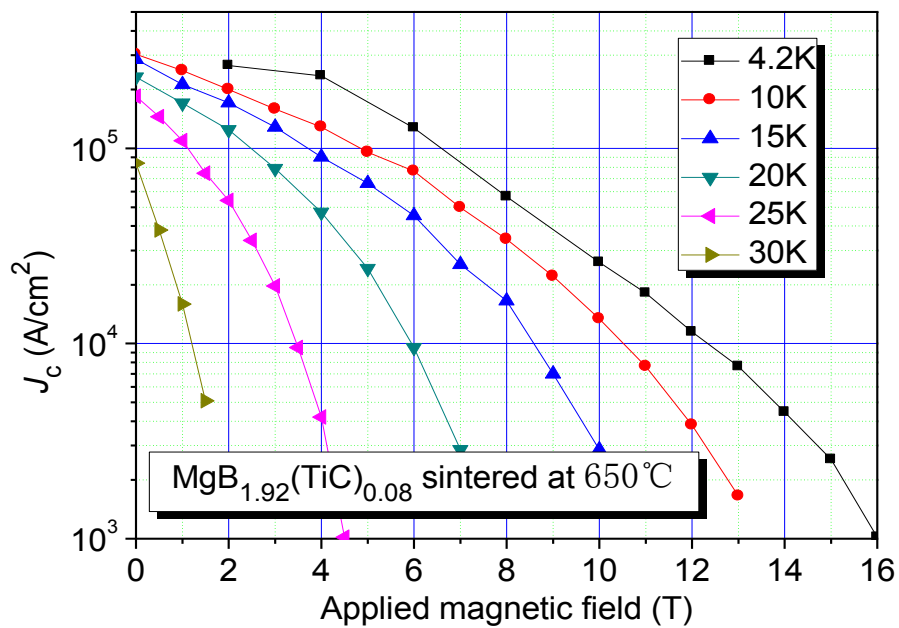


Figure 4-17 Transport J_c of MgB₂ and MgB_{1.92}(TiC)_{0.08} at 4.2K with the magnetic field up to 16 T

The best heat treatment temperatures 650°C and 750°C for the reaction have been selected. Their transport properties were compared. Transport J_c were measured on both MgB_{1.92}(TiC)_{0.08} and MgB_{1.92}C_{0.08} at temperatures ranging from 4.2-30 K.



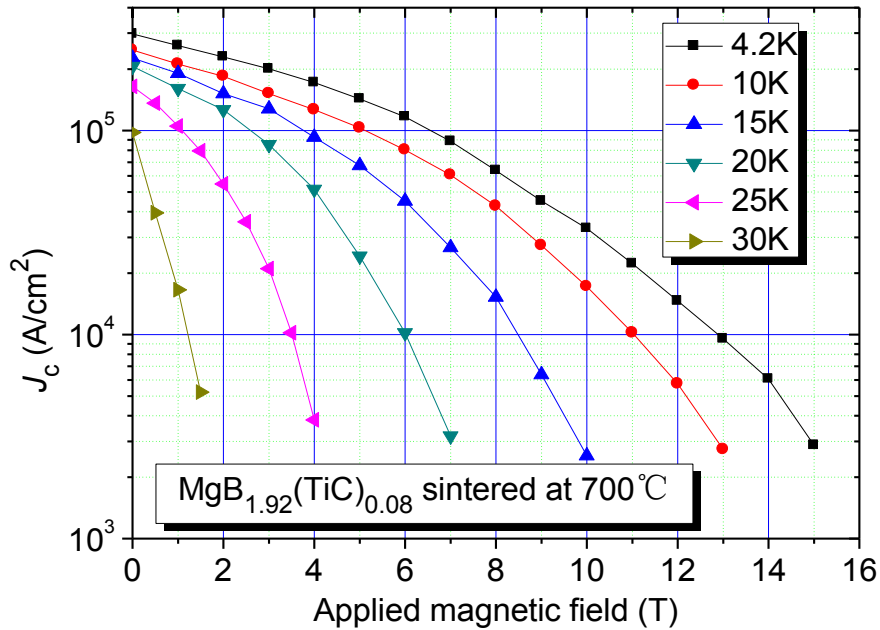


Figure 4-18 Transport J_c of $\text{MgB}_{2-x}(\text{TiC})_x$ with the field up to 16 T at different testing temperatures.

Fig. 4-18 shows the $J_c(H)$ curves for both C and TiC-doped samples sintered at 650°C and 700°C, respectively. The J_c dependence on applied field of $\text{MgB}_{1.92}(\text{TiC})_{0.08}$ is slightly improved than that of $\text{MgB}_{1.92}\text{C}_{0.08}$ in contrast to the different sintering temperatures.

4.5 Conclusion

In this chapter, MgB_2 monofilament wires were fabricated with C and TiC doping. The effect of doping on lattice parameters a and c , critical transition temperature (T_c), critical current density (J_c) and magnetic flux pinning was investigated under a wide range of processing conditions. Improved $J_c(H)$ performance is found in both C and TiC-doped MgB_2 superconductor. T_c is reduced by doping, but can still remain reasonably high above 36 K with different doping contents in zero field. It is found that TiC doping can result in a small depression in T_c . J_c can be obviously affected by both the doping content and the sintering temperature. From the magnetic critical current density measurement, $\text{MgB}_{1.92}(\text{TiC})_{0.08}$ with the

sintering temperature of 800°C exhibits the highest J_c at 20 K. While from the transport critical current density measurement (so called “the four-probe technique”), J_c exhibits the highest and steadiest value at the doping content of $x = 0.08$ with TiC-doped when the sintering temperature is fixed at 700°C. This basal work has provided an effective way to fabricate kilometer level long length MgB₂ wires.

CHAPTER 5

FABRICATION AND PROPERTIES OF MULTICORE MgB₂ WIRES WITH Nb REINFORCEMENT

Aiming at potential alternating current (AC) and direct current (DC) applications, technical MgB₂ wires need a multifilament composite structure with small filament diameters. To stabilize the wire at cryogenic temperatures against thermal runaway, a sheath component with high electrical and thermal conductivity is desirable. At present, stabilization in the high current regime (low field, low temperature) is still insufficient due to the reaction between sheath and superconductor filament interface, the large filaments size with irregular geometrical shape and the inhomogeneous microstructure.

In this chapter, 6-, 12-, and 36-filamentary multi-core MgB₂ wires with Nb/Cu composite tubes as sheath were designed and fabricated by *in situ* PIT method. The mechanical properties and superconductivity were investigated, respectively.

5.1 Conductor structure design and the sample fabrication

The purpose of this part is to investigate the effect of the conductor structure designs on superconductor properties of MgB₂ wires as a function of field and temperature,

Only round wires are considered in our study, tape conductors used in electric power applications will be investigated in the future work. Aiming at the practical applications, the filamentary size of MgB₂ wires and tapes is required for consideration. If the filamentary size is too big, there will be strong flux jump instability which results in the reduction of critical current density. While if the filamentary size is too small, the fabrication process is very difficult due to the poor plasticity of Mg during the *in-situ* PIT process.

As the stabilizer, Cu has been successfully used in lower temperature superconductor (LTS) such as NbTi and Nb₃Sn due to the excellent ductibility and lower resistivity. It has also been used in MgB₂ superconductor act as both the sheath

and stabilizer, but the reaction between Cu and Mg cannot be neglected. The reaction could be controlled and reduced to minimum by decreasing the sintering temperatures and shortening the sintering time. However, in practice, these methods are difficult to be applied in the PIT process, therefore the products always containing Mg-Cu alloy phase. As copper has high thermal and electrical conductivity, and is extremely low in cost, it should be one of the best candidates for the sheath material for MgB₂ if the reaction between Cu and Mg can be controlled or significantly confined to a thin interface layer. In turn this would enhance J_c to the level required by practical applications. This problem has been solved by Sumption *et al.* by the use of a thin layer of Nb as the diffusion barrier between Mg powders and Cu stabilizer^[113].

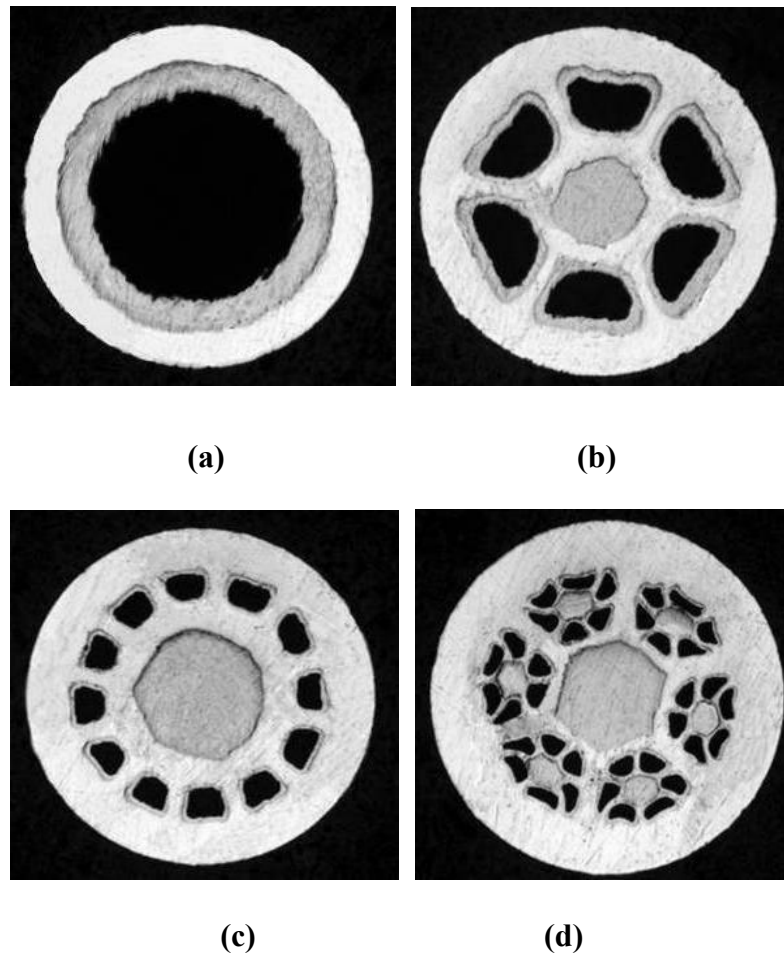


Figure 5-1 Cross section of the MgB_{1.92}(TiC)_{0.08}/Nb/Cu wires with different filament. (a) mono-filamentary, (b) 6-filamentary, (c) 12-filamentary and (d) 36-filamentary

The precursor mixtures were densely filled in the Nb/Cu composite tube. Then, the composite tube was rotary-swaged and drawn to a predetermined size to obtain the

Nb/Cu sheathed monofilament wires. For the 6-, 12-, 36-filament construction, the pre-achieved round filaments, which have been cleaned in advance, were cut into the same length and restacked into another seamless Cu tube, subsequently the tube was in turn swaged and drawn to the final size. Finally, heat treatment was performed at different temperatures under argon, followed by a furnace cooling to room temperature. The characteristics and typical cross-sectional view for the wires are given in Figure 5-1, respectively.

Table 5-1 Volume percent of Cu, Nb and MgB₂ phase in MgB_{1.92}(TiC)_{0.08}/Nb/Cu wires with different conduct structure.

Phase	% (volume percent)			
	1-filament	6-filament	12-filament	36-filament
MgB ₂	38.17	21.89	15.08	13.95
Nb	25.32	23.61	21.97	20.97
Cu	36.51	54.50	62.95	65.08

From Table 5-1, it can be seen that comparing with these multi-filamentary MgB₂ wires, a higher superconductor filling factor appears in 6-filamentary wire, which implies a better J_c value. Moreover, in 6-filamentary, the proportion of Nb is higher. It may be beneficial to the mechanical strength of 6-filamentary, and have a positive effect on the filament densification.

5.2 Mechanical properties of Nb reinforced multi-filamentary MgB₂ wires

5.2.1 Stress-strain analysis of multi-filamentary MgB₂ wires

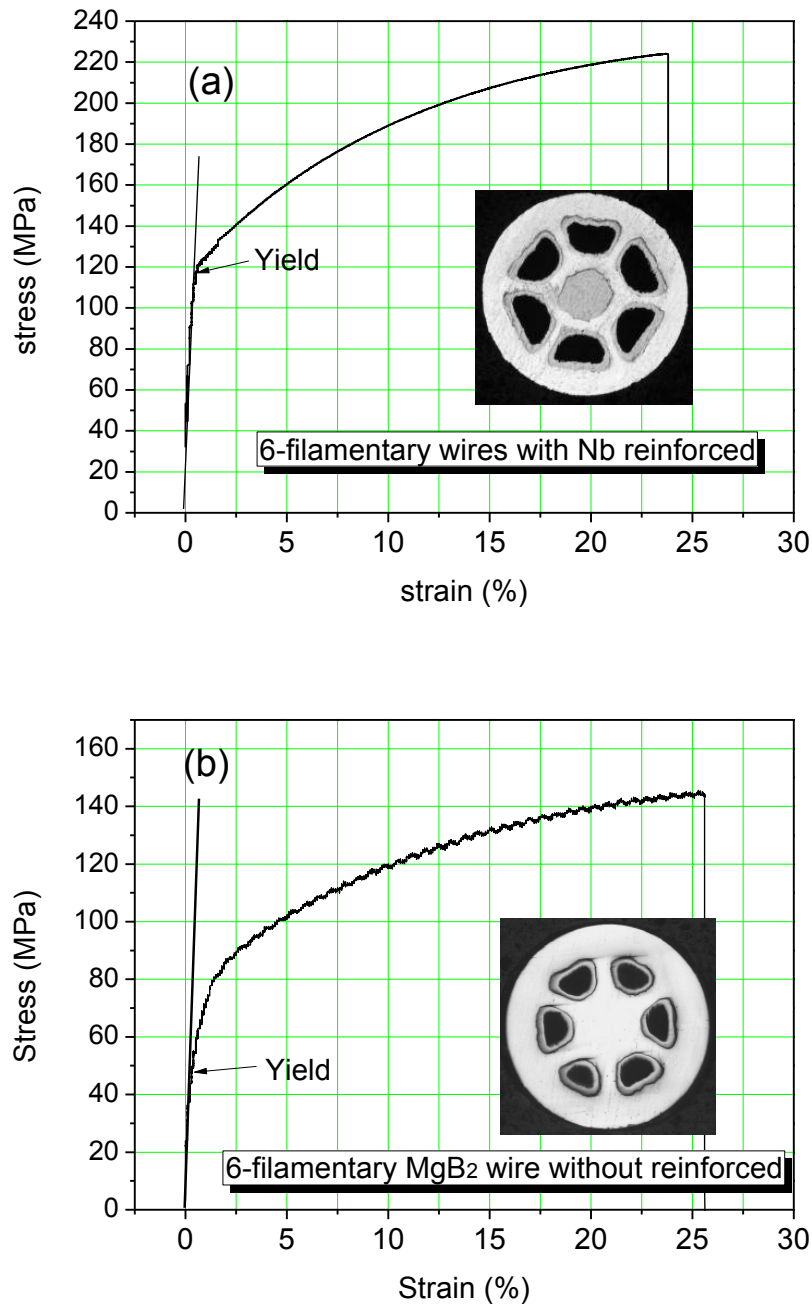


Figure 5-2 Tensile stress vs strain curve of 6-filamentary MgB₂ wires with (a) or without (b) Nb reinforcement after heat treated at 680 °C for 1.5 hours.

Mechanical performances play an important role during the practical applications of MgB₂ conductors. The testing of the mechanical properties at room temperature can make a basic reference for the application of MgB₂ wires. Standard stress-strain experiments applying axial stress were performed at room temperature.

Figure 5-2 shows the comparison between the stress-strain properties of 6-filamentary MgB₂ wires heat treated at 680°C for 1.5 hours with or without Nb reinforcement, where the insert picture is the metallographic image of transverse cross section of MgB₂ wires. The sample with Nb reinforced exhibits higher Young's modulus and higher ultimate tensile strength of ~224 MPa, which reached a plastic strain of about 23.5%. The yield strength of the reinforced sample is around 118 MPa and only 50 MPa for the wires without reinforcement. This indicated that the reinforcement with Nb could remarkably enhance the mechanical property of the 6-filamentary MgB₂ wires.

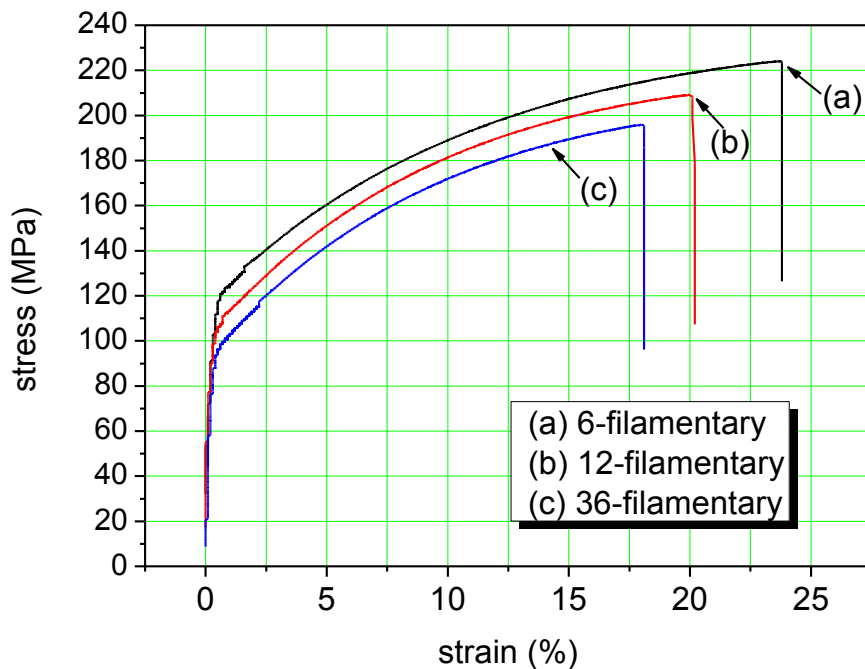


Figure 5-3 Room-temperature stress-strain curves of 6-, 12- and 36-filamentary MgB₂/Nb/Cu wires

Figure 5-3 shows a comparison of mechanical properties between the different filamentary MgB₂ wires heat treated at 680°C for 1.5 hours. The yield stress decreases

with increasing quantity of MgB₂ filament. The detailed mechanical properties of MgB₂ wires with different filament numbers are listed in Table 5-2. The 6-filamentary wires possess the highest room temperature mechanical performances, which maybe due to higher Nb proportion in 6-filamentary wires than the others.

Table 5-2 Mechanical properties of multi-filamentary MgB₂/Nb/Cu wires

Sample	Yield stress/ kN	Yield strength $\sigma_{0.2}$ /Mpa	Tensile force/ kN	Breaking strength σ_b /Mpa	Elongation percentage/%
6-filamentary	0.151	118.1	0.314	224.12	23.8
12-filamentary	0.132	103.5	0.293	208.98	20.1
36-filamentary	0.118	93.7	0.274	195.47	18.1

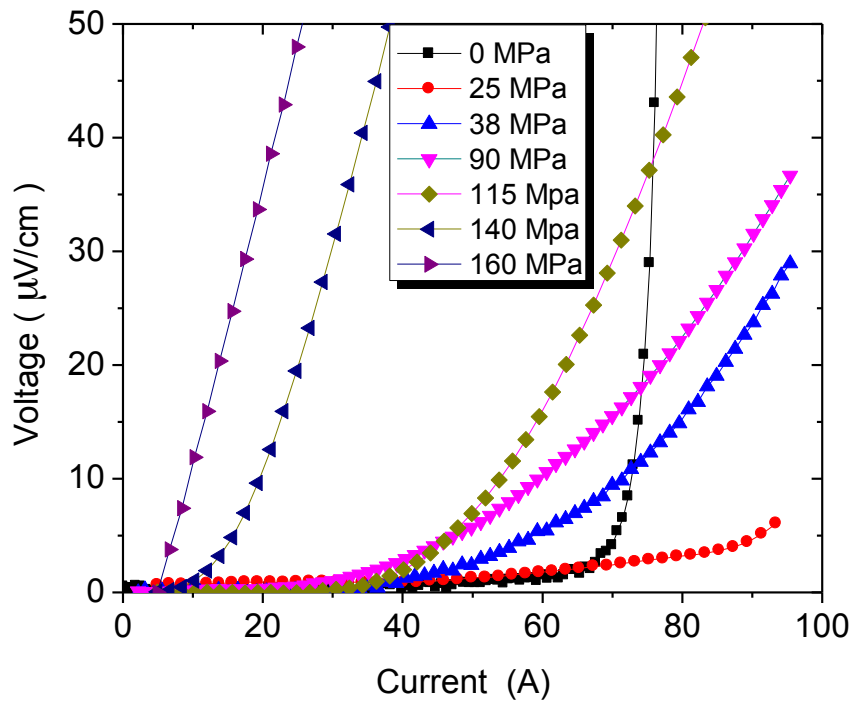


Figure 5-4 Current dependence of voltage of 6-filamentary MgB₂ wires with different stress at 25K

Figure 5-4 is the voltage vs current curves of MgB₂ wires with different tensile strength at 25K with zero fields. It can be seen from the figure that with 25 MPa stress the transport property can be enhanced, because the stress during drawing increases the defect density, and these defect act as the flux pinning centers. With the further increase of stress from 25 MPa to 115 MPa, the critical current decreases. And the critical current dropped very fast while the stress was high than 115 MPa. The poor grain connectivity as a result of the large applied stress can be responsible for the reduced I_c values. This result shows that the cracks appearing with large stress force were fatal for the current carrying properties of MgB₂ wires.

5.2.2 Bending strain analysis of mono- and multi-filamentary MgB₂ wires

For technical applications, the mechanical stability of MgB₂ wires to withstand applied stresses and strains is required as well as thermal stability and magnetic stability reported in Refs.^{[114].[115]}. The potential strain sources involved in applications are winding strains, thermal stresses and Lorentz forces depending on the specific situation. J_c can be degraded due to the mechanical stresses. So far, only a few papers on the mechanical behavior of MgB₂ composites have been reported. Kitaguchi *et al.*^[116] reported the effect of tensile and compressive strain on the critical current of MgB₂. A linear increase and steep degradation of I_c was observed with the strain change from -0.4% to 0.4% and exceeding 0.5%, respectively. Kovac *et al.*^[117] studied the mechanical behavior of MgB₂/Fe wires. They concluded that the reversible strain has the limit in the range of $\varepsilon_{irr} = 0.2-0.5\%$. In this part, we mainly investigated the mechanical properties and critical current density change of Nb/Cu sheathed MgB₂ multi-filamentary wires with different strains formed by bending on framework with variable diameters or drawing with a spring balance.

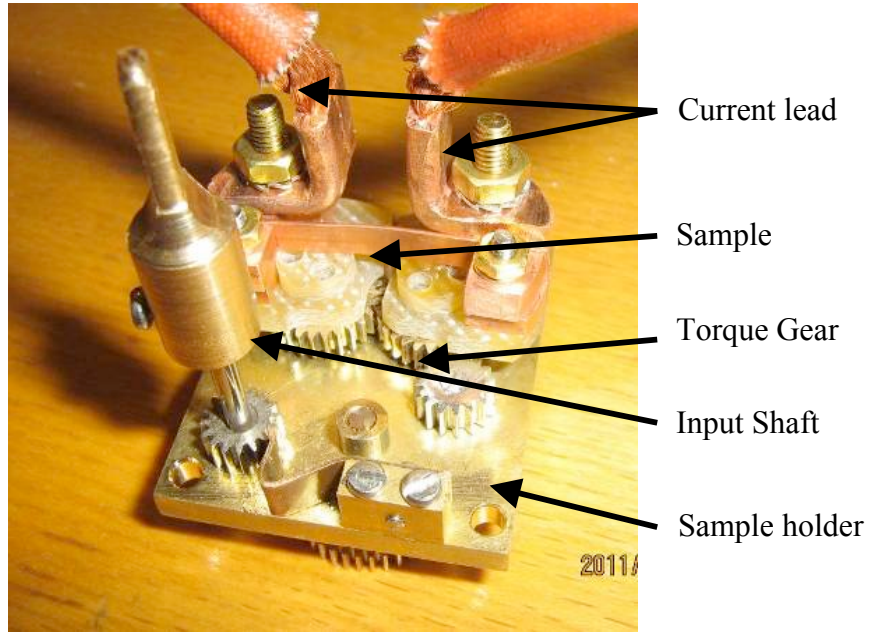


Figure 5-5 Bending strain measurement holder

A bending device was designed and tested our MgB_2 wires and tapes successfully. As shown in Figure 5-5, a series of gears with different ratios are moved by rotating torque arms through an input shaft controlled outside the dewar. The MgB_2 wires and tapes are mounted on a support beam and a groove is placed on the neutral axis of the beam to produce pure bending effect on the strand. The minimum bending radius of 6 mm can be achieved.

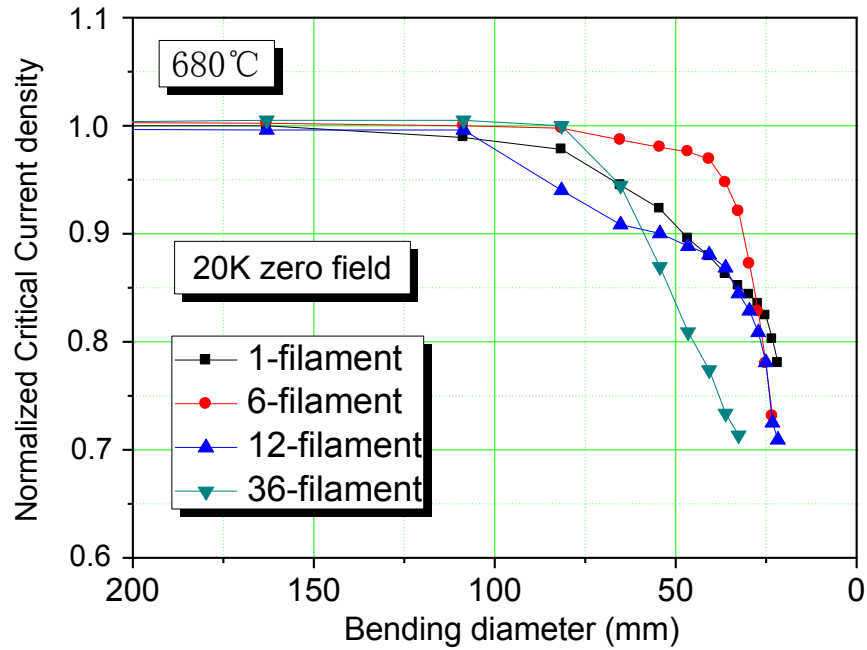


Figure 5-6 Critical current declines dependent on the bending radius of different filamentary wires

Figure 5-6 shows that direct bending tests were done with different diameters from 250 to 30 mm. In all wires, when the bending diameter is more than 108 mm, no degradation occurs to J_c . While the bending diameter is less than 108 mm, an evident degradation of J_c can be observed. Comparing these wires with different conductor structures, 6-filamentary wire can withstand the largest deformation. The current carrying capacity in this wire cannot be affected until the bending diameter is less than 81 mm. When the bending diameter is 54.32 mm, 1.98%, 7.69%, 9.96% and 13.07% current degradation was occur to 6-, 1-, 12- and 36-filamentary wires, respectively. It can be noticed that the decline in the J_c of 36-filamentary wire is 6.6 times higher than that of 6-filamentary wire with the bending diameter of 54.32 mm.

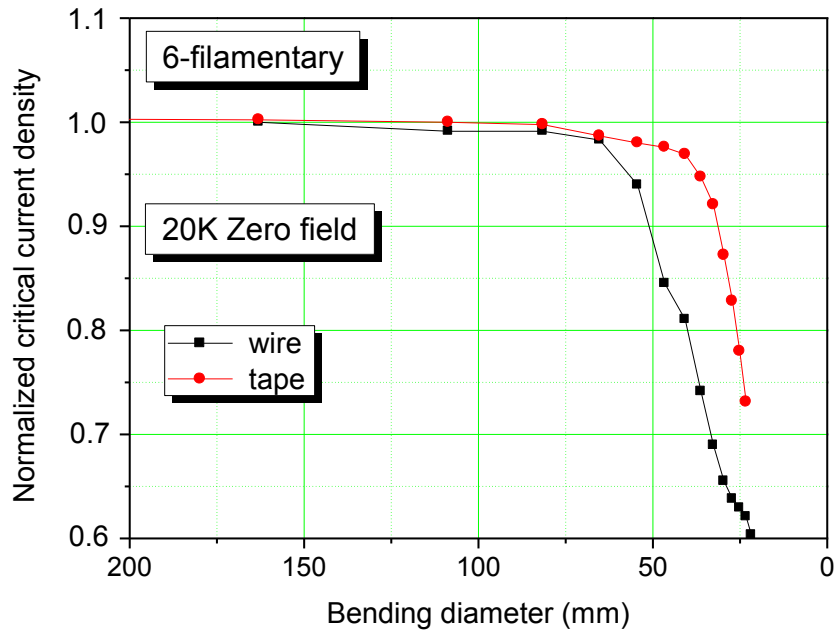


Figure 5-7 Comparison of the J_c degradation with the bending of 6-filamentary wires and tapes

Based on the above data, it can be found that 6-filamentary wire has the best current carrying capacity and mechanical properties. The 6-filamentary composite tube was drawn to a round wire with the diameter of 1.44 mm step by step with the section reduction of 10% per step. This wire was subsequently rolled with the thickness reduction of about 10-12% per step. The final tape was obtained by rolling the wire to a tape with the thickness of 0.4 mm and width of 3.2 mm. It has been noticed that in the same test condition, the performance of tape is better than that of wire, which agreed with Ref. [118]. The reason might be attributed to the rolling enhanced densification and thus the restoration of its connectivity. This process results in drastic J_c growth. Such an effect of rolling might be due to the differences in powder flowing process inside the round and flat-shaped channels.

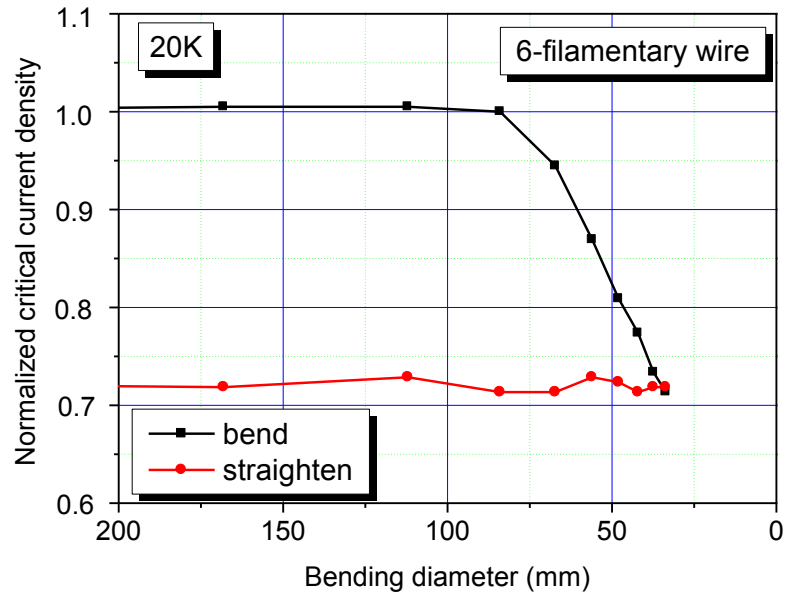
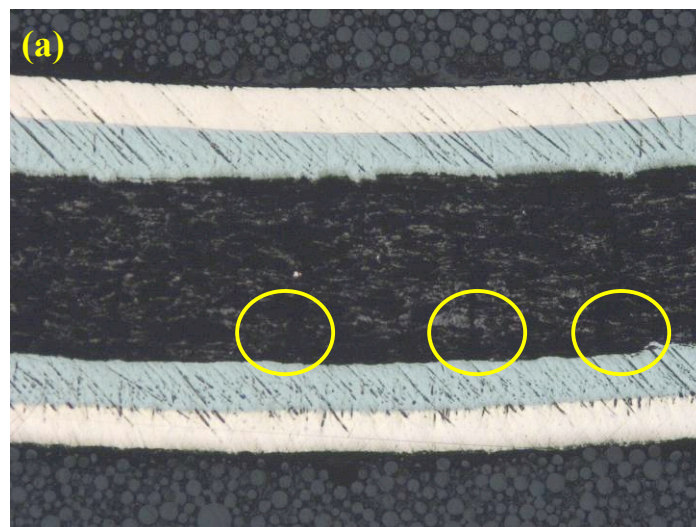


Figure 5-8 Critical current I_c change with the bending and straighten of the wires

We have discussed the change of critical current I_c of 6-filament wire with variable bending diameters in Figure 5-6. In Figure 5-8, we show the critical current I_c of 6-filament wire change with the whole process (including bend and straighten). During the bending process, the I_c values rapidly decline, when the bending diameter is less than 84 mm. About 29% reduction of I_c occurred when the sample was bent to 34 mm in diameter. Then at this bending diameter, the wire was straightened gradually. The I_c value basically remains at this degraded level.



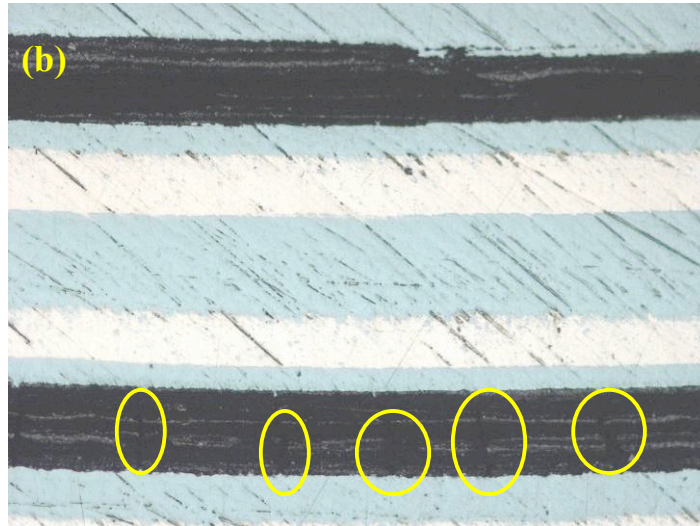
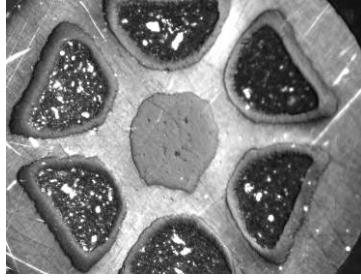


Figure 5-9 Cracks in mono-filamentary (a) and 6-filamentary (b) MgB₂ wires heat treated at 700 °C

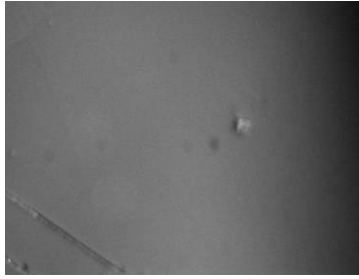
Figure 5-9 shows the photomicrographs of the longitudinal cross section of 1-filamentary and 6-filamentary MgB₂ wires after the heat treatment at 700°C. Cracks can be observed on both of these two wires. Meanwhile, it can be observed that both the interfaces between the Nb and MgB₂ core and between Nb and Cu are very smooth. It suggested that there is no non-superconductive layer formed during the sintering process. When the samples are bent to the same diameter excess the maximal strain about 10%, in 1-filamentary wire, there will be a large deep crack appeared, while in 6-filamentary wire, there may be a small crack appeared due to center Nb/Cu rod acting as the reinforcement.

5.3 Magneto-optical analysis of multi-filamentary MgB₂/Nb/Cu wires

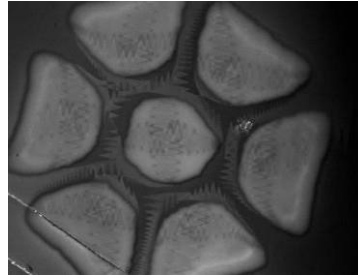
To understand the interfacial diffusion behavior in multi-filamentary wires, the flux motion in these MgB₂/Nb/Cu wires was measured with Magneto-Optical Imaging (MOI). The interaction between Nb sheath and MgB₂ superconductor core with local MO imaging under perpendicular applied fields was investigated. Such interactions are mainly visible in the case of ZFC state with the applied field of $H = 100$ mT. The typical optical microscopy image and MO images for a polished surface of the 6-filamentary MgB₂ wires heat treated at 800°C are shown in Figure 5-2.



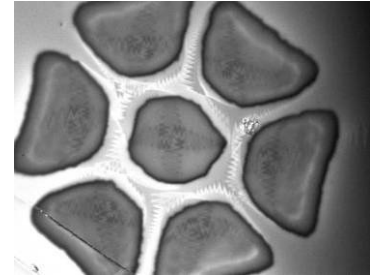
(a)



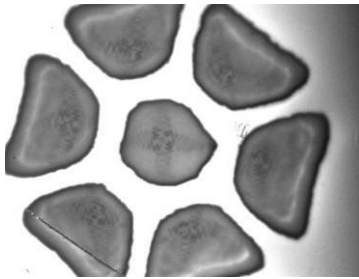
(b) 0 mT



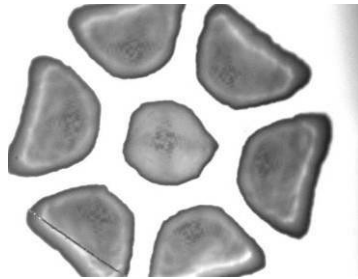
(c) 20 mT



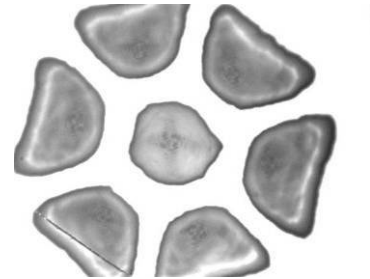
(d) 40 mT



(e) 60 mT



(f) 80 mT



(g) 100 mT

Figure 5-10 Optical microscopy image (a) and Magneto-optical image (b-g) of 6-filamentary MgB_2 wires at 6 K with a perpendicular applied field from 0 to 100 mT

The porous microstructure was confirmed in Figure 5-10(a). Magneto-optical images were taken under zero field cooling (ZFC) conditions. Bright contrast in the images taken in ZFC mode represents the flux-penetrated regions, while dark contrast corresponds to the well screen regions. The flux penetrated much further into the sample with increasing field, and a blurry bright ring forms at the interface of the MgB_2 and Nb in each filament. This ring becomes clearer with larger applied field. As mentioned above, the bright ring is due to the non-superconducting layer between MgB_2 -Nb interfaces. The MO contrast is uniform in each filament, indicating the homogeneously distributed screening currents.

5.4 Superconductivity of the multi-filamentary MgB₂ wires

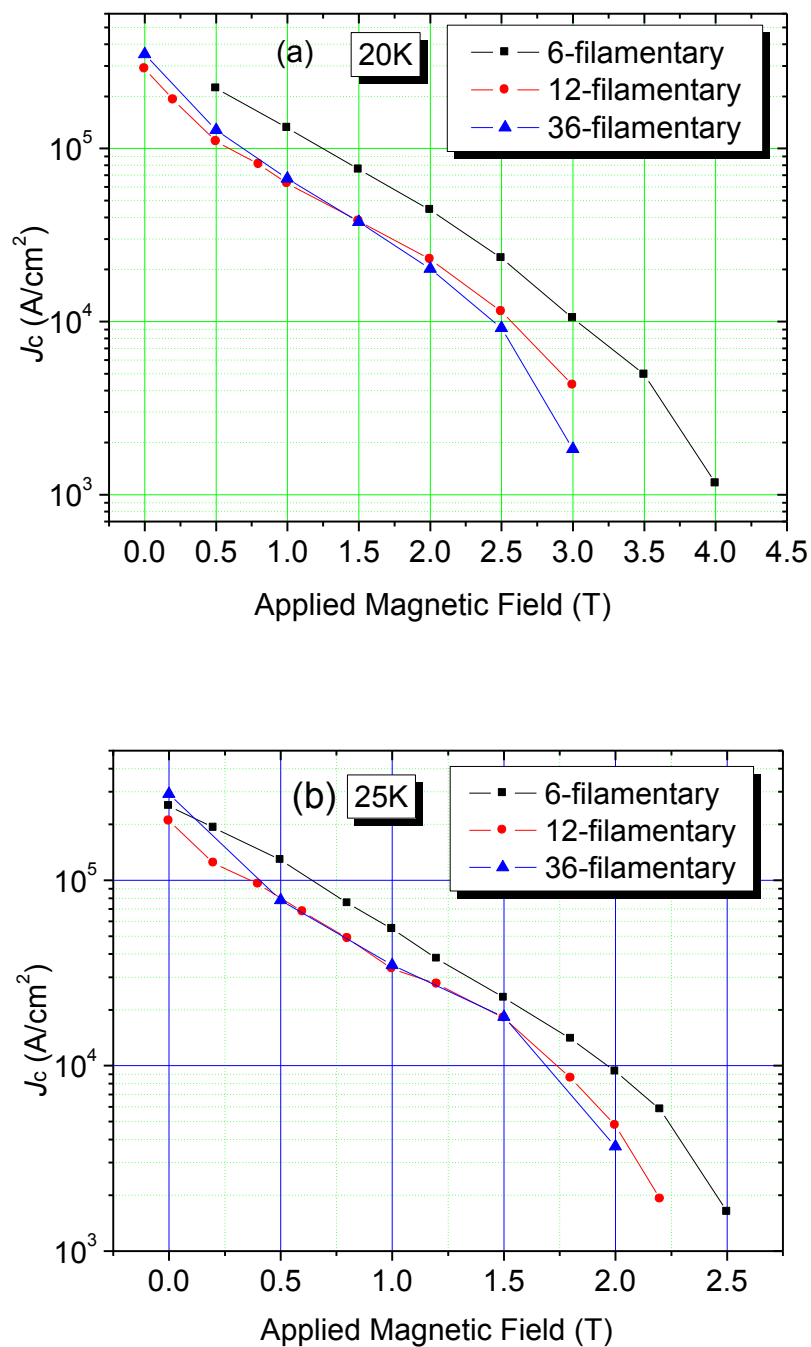


Figure 5-11 Transport J_c as a function of magnetic field on MgB_{1.92}(TiC)_{0.08} wires with different filaments

Four-point transport J_c measurements were performed from 4.2 K to 30 K. The samples were 30 mm in length, with a gauge length of 10 mm. The J_c criterion was 1

$\mu\text{V}/\text{cm}$. Figure 5-11 compares the J_c values of the 6-, 12- and 36-filamentary wires with the same doping level and heat treatment temperature (680°C for 90 min) at 20 K and 25 K, respectively. It can be observed that the 6-filamentary wire exhibited the best $J_c(B)$, while the 12-filamentary result is similar to that of the 36-filamentary wire. Compared Figure 5-11 (a) and (b), at the same applied field of 2 T, $J_c(B)$ values of $4.36 \times 10^4 \text{ A}/\text{cm}^2$ in Figure 5-11 (a) and $0.94 \times 10^4 \text{ A}/\text{cm}^2$ in Figure 5-11 (b) was obtained with the temperature of 20 and 25K respectively for the 6-filamentary wire. It shows that the applied temperature has important effect on the transport property of MgB_2 .

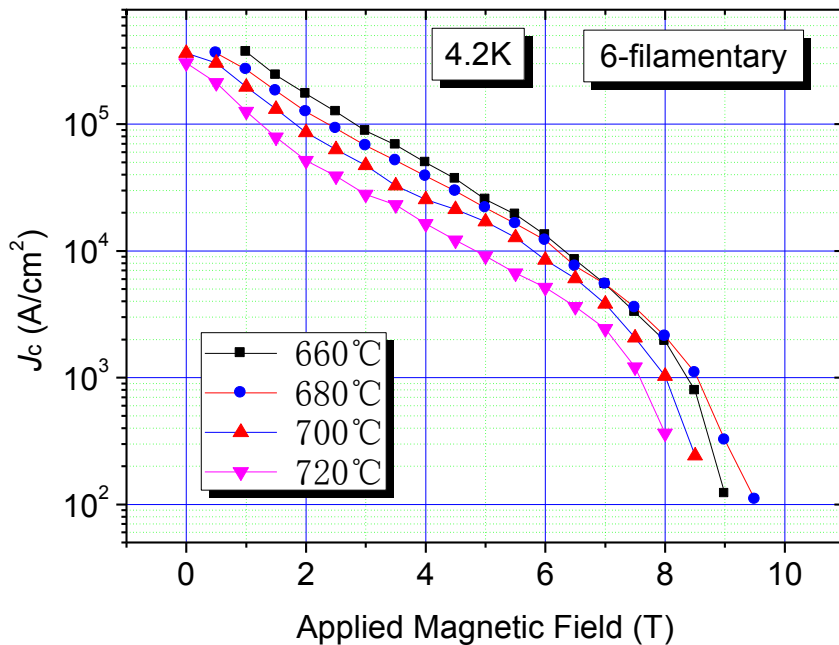


Figure 5-12 Transport J_c as a function of magnetic field on 6-filamentary $\text{MgB}_{1.92}(\text{TiC})_{0.08}$ wires at 4.2 K with the field up to 10 T

Figure 5-12 shows the comparison of J_c values of the 6-filamentary wires at different temperatures. It is noticed that J_c of the sample sintered at 660°C is better than that those sintered at other higher temperatures with the applied field of 0-6 T. While with the applied field increased over 6 T, the maximum J_c was obtained in the sample sintered at 680°C . This may be due to the better intergrain connectivity. The J_c values in the sample sintered at 700 or 720°C shows a lower value. This is because

under the higher sintering temperature, the non-superconducting diffusion layer tends to growth thicker and this diffusion layer obstructs the current transmission.

From aforementioned results, it is found that the J_c property of 6-filamentary wire is better than that of other multi-filamentary wires. The transport J_c of the sample was measured at temperatures ranging from 4.2 K to 30 K.

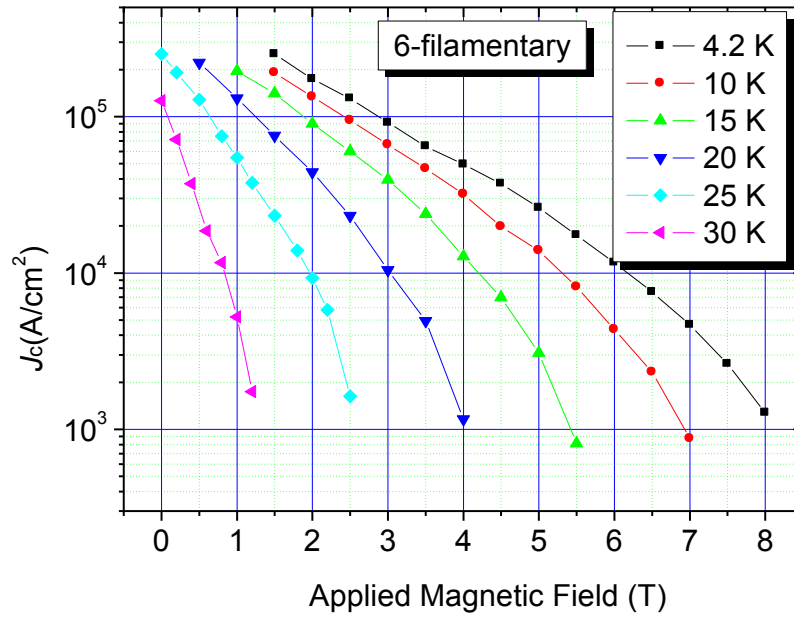


Figure 5-13 Transport J_c as a function of magnetic field on 6-filamentary $\text{MgB}_{1.92}(\text{TiC})_{0.08}$ wires at different temperature

Figure 5-13 shows the current density J_c versus magnetic field (H) at different temperatures. As shown in Figure 5-13, the J_c value of the 6-filamentary wire is higher than 10^4 A/cm^2 at 4.2 K, 6 T. The J_c value of the 6-filamentary wire is $\sim 10^4 \text{ A/cm}^2$ at 20 K, 3 T. These results confirmed that it is promising for producing high-quality MgB_2 superconducting wires for practical applications.

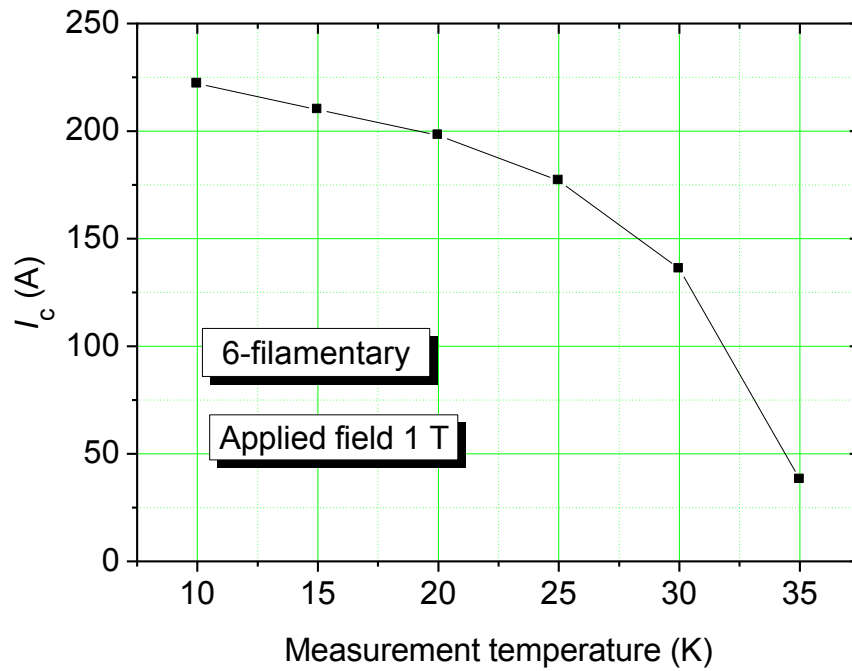
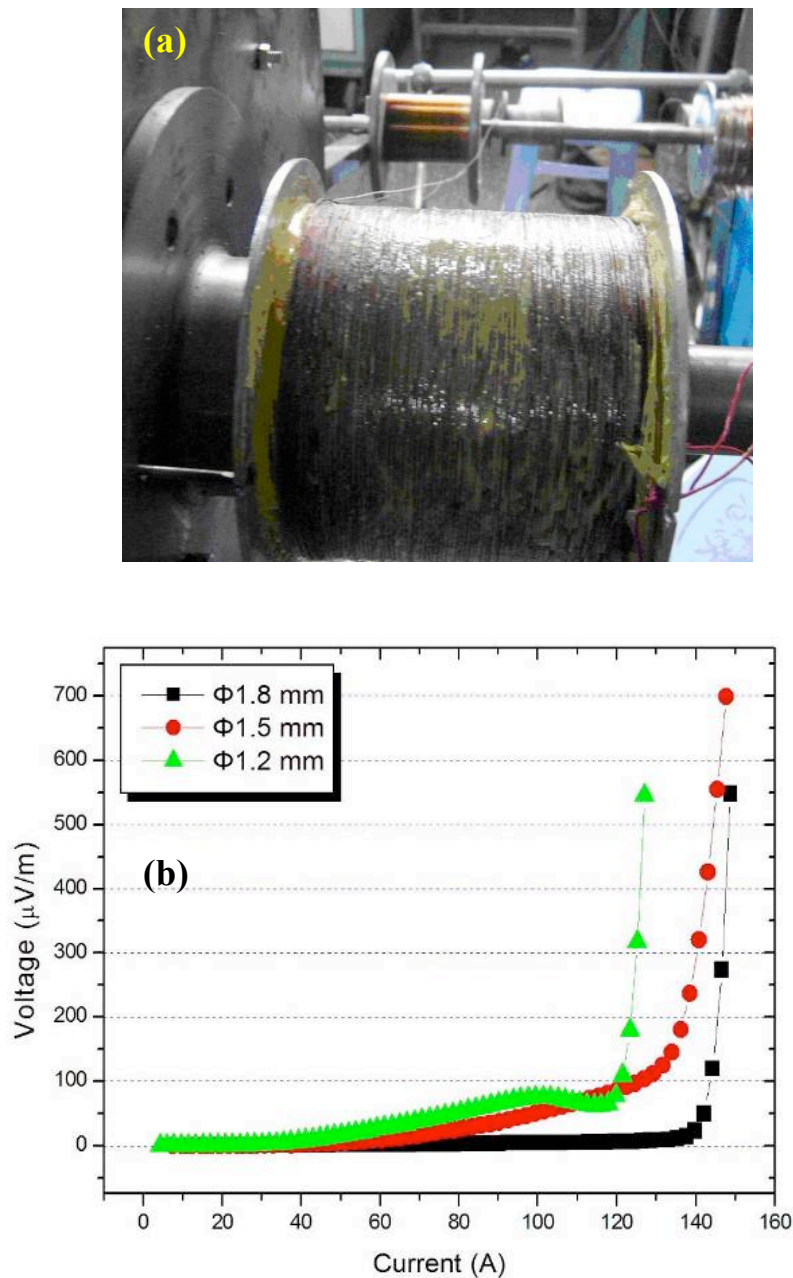


Figure 5-14 Critical current I_c as a function of temperature on 6-filamentary $\text{MgB}_{1.92}(\text{TiC})_{0.08}$ wire

Figure 5-14 shows the temperature dependence of critical current at 1 T for the $\text{MgB}_{1.92}(\text{TiC})_{0.08}$ wire heat treated at 680°C for 90 minutes. I_c values decreased with increasing measurement temperature, and the decreasing rate change faster when the measurement temperature is higher than 25 K. This indicates the optimal operating temperature of these wires should be lower than 25 K.

5.5 Critical current of 100 meter $\text{MgB}_2/\text{Nb}/\text{Cu}$ wires



reaches 144 A for 1.8 mm wire and 120 A for 1.2 mm wire by the voltage criterion of 100 $\mu\text{V}/\text{m}$. But the J_{ce} increases with decreasing wire diameter. The J_{ce} value reaches $1.1 \times 10^4 \text{ A}/\text{cm}^2$ for 1.2 mm wire, which is $5.7 \times 10^3 \text{ A}/\text{cm}^2$ for 1.8 mm wire. This result indicates that the dense MgB_2 core in multi-filamentary wires is a key factor to enhance the critical current density. Furthermore, the effects of the Nb core at the center of these multi-filament wires on the reinforcement and densification of MgB_2 filaments should be further investigated in the future.

5.6 Current homogeneity on 6-filamentary MgB_2 wires

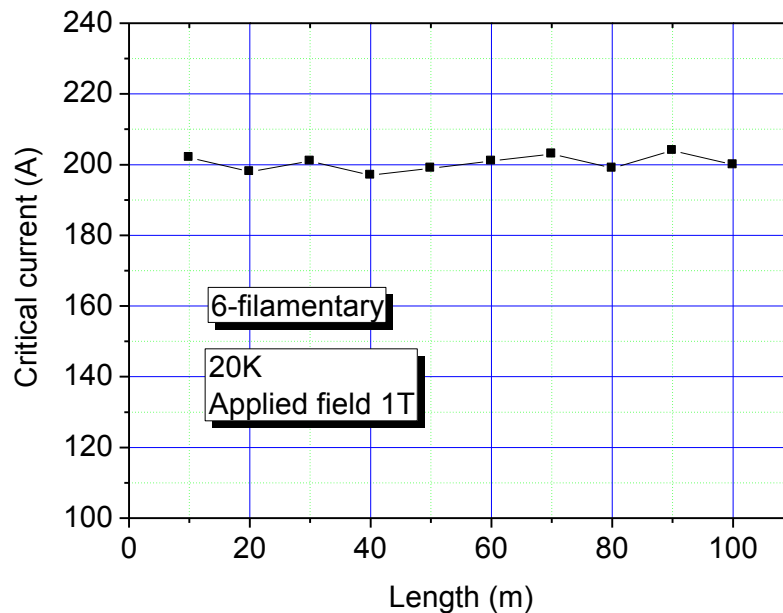


Figure 5-16 Homogeneity of critical current of MgB_2 wire (20K, 1T)

100 meters of 6-filamentary MgB_2 wires with the diameter of 1.0 mm were sintered at 680°C for 90 minutes. The heat treated wires were cut into 10 pieces and 10 m long for each piece. The short sample in 3 cm was cut from each piece, and this short sample was then mounted on the sample holder with its axis perpendicular to the applied field. After soldering the current leads and voltage leads on the sample with the division between the two voltage leads of 10 mm, the sample was put into the cryostat and the critical current was measured at 20K with the applied field of 1 T. Related results are shown in Figure 5-16, the difference between maximum and

minimum critical current is smaller than 5%. Therefore, the good homogeneity of I_c distribution of this 6-filamentary MgB₂/Nb/Cu wires has been proved.

5.7 Conclusion

The Cu-clad 6-, 12-, and 36-filamentary MgB₂/Nb/Cu wires with Nb reinforcement have been fabricated with *in-situ* PIT method. In order to improve the strength of wires, the Nb-core was used as the central filament. The stress-strain, bending properties, microstructures, and superconductivity properties were analyzed, respectively. The results confirmed that the yield stress decreases with increasing quantity of MgB₂ filament. The bending measurement shown that when the samples are bent to the same diameter excess the maximal strain about 10%, in 1-filamentary wire, there will be a large deep crack appeared, while in 6-filamentary wire, there may be a small crack appeared due to center Nb/Cu rod acting as the reinforcement. Therefore, the good homogeneity of I_c distribution of 6-filamentary MgB₂/Nb/Cu wires with the length in 100 meters has been observed. That means the *in-situ* PIT technique with the Nb as the reinforcement can be used to produce a certain long length MgB₂/Nb/Cu wires. The superconducting filaments of MgB₂/Nb/Cu composite tubes have well workability suitable for the long length and multi-filament MgB₂ wires.

CHAPTER 6

SUMMARY

Since the discovery of superconductivity in 2001, MgB₂ with a critical temperature (T_c) of 39 K has been believed to be a promising candidate for the engineering applications within the temperature range of 20-30 K by GM cryocooler. However, compared with the traditional low temperature superconductors, MgB₂ often exhibits a rapid decrease of J_c with the increase of applied magnetic field (B). Therefore, the low critical current density and poor pinning behavior are the key problems restricting the practical applications of MgB₂ superconductor. In order to improve the critical current density, the effects of raw materials, fabrication process, elemental doping and substitution on the microstructures and superconducting properties of MgB₂ have been systematically investigated in this thesis.

At first, the monofilament MgB₂ wires with Nb/Cu composite tube as the sheath are fabricated by *in-situ* PIT technique and heat treated from 600°C to 950°C for 2 hours. The influences of sintering temperatures on the superconducting properties of the MgB₂/Nb/Cu wires have been systematically investigated. And the phase formation processes and microstructures of the diffusion layer between MgB₂ and Nb, which exhibited severe effect on the degradation of superconducting properties, have also been observed and studied. The XRD analysis show that all the samples heat treated at different temperature contain the MgB₂ phase as the main phase. The heat treatment temperature does not effect on the lattice parameter of MgB₂, but the crystallinity increases with increasing heat treatment temperatures. Transport resistance test and the magnetization measurements also indicate that the wire is in superconducting state. However, the transport critical current measurements did not show superconducting current of MgB₂ at all for the sample heat treated at 750°C or higher heat treatment temperature. Therefore, we carried out the study on the microstructures and phase formation process of the interface layer between MgB₂

superconducting core and Nb sheath. The results show that there is a diffusion layer at this region which is composed of non-superconducting phase for the sample heat treated at high temperature, and this diffusion layer obstructs the current transmission. This diffusion layer has obvious effects on the critical current of MgB₂ wires heat treatment at high temperature and the best heat treatment temperature for the MgB₂ wires with Nb as the barrier layer should be lower than 750°C. Further more, the presences of holes at the interface between MgB₂ core and Nb also reduced the current transfer from Nb/Cu sheath to MgB₂ core.

MgB₂ monofilament wires were fabricated with C and TiC doping. The effect of doping on lattice parameters a and c , critical transition temperature (T_c), critical current density (J_c) and magnetic flux pinning was investigated under a wide range of processing conditions. Improved J_c (H) performance is found in both C and TiC-doped MgB₂ superconductor. T_c is reduced by doping, but can still remain reasonably high above 36 K with different doping contents in zero field. It is found that TiC doping can result in a small depression in T_c . J_c can be obviously affected by both the doping content and the sintering temperature. From the magnetic critical current density measurement, MgB_{1.92}(TiC)_{0.08} with the sintering temperature of 800°C exhibits the highest J_c at 20 K. While from the transport critical current density measurement, J_c exhibits the highest and steadiest value at the doping content of $x = 0.08$ with TiC-doped when the sintering temperature is fixed at 700°C. This basal work has provided an effective way to fabricate kilometer level long length MgB₂ wires.

The Cu-clad 6-, 12-, and 36-filamentary MgB₂/Nb/Cu wires with Nb reinforcement have been fabricated with *in-situ* PIT method. In order to improve the strength of wires, the Nb-core was used as the central filament. The stress-strain, bending properties, microstructures, and superconductivity properties were analyzed, respectively. The results confirmed that the yield stress decreases with increasing quantity of MgB₂ filament. The bending measurement shown that when the samples are bent to the same diameter excess the maximal strain about 10%, in 1-filamentary

wire, there will be a large deep crack appeared, while in 6-filamentary wire, there may be a small crack appeared due to center Nb/Cu rod acting as the reinforcement. Therefore, the good homogeneity of I_c distribution of 6-filamentary MgB₂/Nb/Cu wires with the length in 100 meters has been observed. That means the *in-situ* PIT technique with the Nb as the reinforcement can be used to produce a certain long length MgB₂/Nb/Cu wires. The superconducting filaments of MgB₂/Nb/Cu composite tubes have well workability suitable for the long length and multi-filament MgB₂ wires.

REFERENCE

- [1]. H. Kamerlingh Onnes, The superconductivity of mercury, *Comm. Phys. Lab. Univ. Leiden, Nos.* 122-124, 1911.
- [2]. J. Bardeen, L. N. Cooper, and J. R. Schrieffer. Theory of superconductivity, *Physical Review*, Volume 108, 5. December 1957, pp 1175-1204.
- [3]. Nagamatsu Jun, Nakagawa Norimasa, Muranaka Takahiro, *et al.*, Superconductivity at 39 K in magnesium diboride. *Nature*, Volume 410, 1 March 2001, pp 63-64.
- [4]. D. C. Larbalestier, L. D. Cooley, M. O. Rikel, *et al.*, Strongly linked current flow in polycrystalline forms of the superconductor MgB₂. *Nature* 410(2001) 186-189.
- [5]. Y. Takano, H. Takeya, H. Fujii, *et al.*, Superconducting properties of MgB₂ bulk materials prepared by high-pressure sintering, *Appl. Phys. Lett.*, Vol. 78, No. 19, 7-MAY-2001, pp. 2914-2916.
- [6]. V. N. Narozhnyi, G. Fuchs, A. Handstein, *et al.*, Comparative study of dense bulk MgB₂ materials prepared by different methods, *Journal of superconductivity: Incorporating novel magnetism*, Vol. 15, No. 6, Dec. 2002, pp. 599-601.
- [7]. S. Lee, A. Yamamoto, H. Mori, *et al.*, Single crystals of MgB₂ superconductor grown under high-pressure in Mg-B-N system, *Physica C*, Vol. 378-381, (2002), pp. 33-37.
- [8]. J Karpinski, M Angst, J Jun, *et al.*, MgB₂ single crystals: high pressure growth and physical properties, *Supercond. Sci. Technol.* 16 (2003) 221-230.
- [9]. D. Blank, H. Hilgenkamp, A. Brinkman, *et al.*, Superconducting Mg-B films by pulsed-laser deposition in an in situ two-step process using multicomponent targets, *Appl. Phys. Lett.*, Vol. 79, No. 3, 16-July-2001 394-396.
- [10]. W. N. Kang, Hyeong-Jin Kim, Eun-Mi Choi, *et al.*, MgB₂ Superconducting Thin Films with a Transition Temperature of 39 Kelvin, *Science*, Vol. 292, 25-May-2001, pp. 1521-1523.
- [11]. S. Jin, H. Mavoori, C. Bower, *et al.*, High critical currents in iron-clad superconducting MgB₂ wires. *Nature*, 31-May.-2001, Vol. 411, pp. 563-565.
- [12]. A. K. Pradhan, Y. Feng, Y. Zhao, *et al.*, Transport behavior and critical current densities in MgB₂ wires, *Appl. Phys. Lett.*, Vol. 79, No. 11, 10-Sep-2001, pp. 1649-1651.
- [13]. Giovanni Grasso, Andrea Malagoli, Carlo Ferdeghini, *et al.*, Large transport critical currents in unsintered MgB₂ superconducting tapes, *Appl. Phys. Lett.*, Vol. 79, No. 2, 9-Jul-2001, pp. 230-232.
- [14]. H. Fang, S. Padmanabhan, Y. X. Zhou, *et al.*, High critical current density in iron-clad MgB₂ tapes, *Appl. Phys. Lett.*, Vol. 82, No. 23, 9-Jun-2003, pp. 4113-4115.

- [15]. T. Masui, S. Lee, and S. Tajima, Effect of the growing process on the electronic properties of MgB₂ single crystals, *Physica C*, vol. 392–396 pp. 281–285, 2003.
- [16]. Yu. Eltsev, S. Lee, K. Nakao, *et al.*, Anisotropic superconducting properties of MgB₂ single crystals, *Physica C*, vol. 378–381, pp. 61–64, 2002.
- [17]. Cristina Buzea, Tsutomu Yamashita. Review of the superconducting properties of MgB₂. *Supercond. Sci. Technol.* 14 (2001) R115-R146.
- [18]. L. Lyard, P. Samuely, P. Szabo. *et al.*, Anisotropy of the upper critical field and critical current in single crystal MgB₂. *Physical Review B.* 66(2002) 180502.
- [19]. J R Thompson, M Paranthaman, D K Christen, *et al.*, High temporal stability of supercurrents in MgB₂ materials. *Supercond. Sci. Technol.* 14 (2001) L17-L20.
- [20]. M. Dhalle, P. Toulemonde, C. Beneduce, *et al.*, Transport and inductive critical current densities in superconducting MgB₂. *Physica C* 363(2001), 155-159.
- [21]. Zi-Kui Liu, D. G. Schlom, Qi Li. *et al.*, Thermodynamics of the Mg–B system: Implications for the deposition of MgB₂ thin films. *Appl. Phys. Lett.*, Vol. 78, No. 23, 4 June 2001, 3678-3680.
- [22]. G. Yan, Y. Feng, B. Q. Fu, *et al.*, Effect of synthesis temperature on density and microstructure of MgB₂ Superconductor at ambient pressure, *Journal of Materials Science*, 39 (2004): 4893-4898.
- [23]. Tomáš Holúbek. Current transfer and thermal stability of composite MgB₂ superconductors. *Ph.D Thesis*, Slovak Academy of Sciences, Slovak Republic, Apr. 2008, pp. 16.
- [24]. M. Putti, V. Braccini, C. Ferdeghini, *et al.*, Neutron irradiation of Mg¹¹B₂: From the enhancement to the suppression of superconducting properties, *Appl. Phys. Lett.* 86, 112503 (2005).
- [25]. Y. Bugoslavsky, L. F. Cohen, G. K. Perkins, *et al.*, Enhancement of the high-magnetic-field critical current density of superconducting MgB₂ by proton irradiation, *Nature* vol. 410, pp.561-563 2001.
- [26]. Tania M. Silver, Joseph Horvat, Mark Reinhard, *et al.*, Uranium Doping and Thermal Neutron Irradiation Flux Pinning Effects in MgB₂, *IEEE Trans. on Appl. Supercond.*, Vol. 14, No. 1, March 2004, pp. 33-39.
- [27]. K. Agatsuma, M. Furuse, M. Umeda, *et al.*, Properties of MgB₂ superconductor by doping impurity of SiC, graphite, C60, and C nano-tube. *IEEE Trans. on Appl. Supercond.*, Vol. 16, No. 2, June 2006, pp. 1407-1410.
- [28]. S. X. Dou, S. Soltanian, J. Horvat, *et al.*, Enhancement of the critical current density and flux pinning of MgB₂ superconductor by nanoparticle SiC doping, *Appl. Phys. Lett.*, vol. 81, pp. 3419-3421, 2002.
- [29]. M. D. Sumption, M. Bhatia, M. Rindfleisch, *et al.*, Large upper critical field and irreversibility field in MgB₂ wires with SiC additions. *Appl. Phys. Lett.* vol. 86, p.092507, 2005.
- [30]. X Xu, S X Dou, X L Wang, *et al.*, Graphene doping to enhance the flux pinning and supercurrent carrying ability of a magnesium diboride superconductor. *Supercond. Sci. Technol.* 23 (2010) 085003 (5pp).

- [31]. Y. W. Ma, A. X. Xu, X. H. Li. *et al.*, Enhanced Critical Current Density of MgB₂ Superconductor Synthesized in High Magnetic Fields, *Jpn. J. Appl. Phys.* Vol.45, pp. L493-L496, 2006.
- [32]. S. X. Dou, W. K. Yeoh, O. Shcherbakova. *et al.*, Magnetic field processing to enhance critical current densities of MgB₂ superconductors, *Appl. Phys. Lett.*, vol. 89, p. 202504, 2006.
- [33]. X Xu, J H Kim, W K Yeoh, *et al.*, Improved J_c of MgB₂ superconductor by ball milling using different media. *Supercond. Sci. Technol.* 19 (2006) L47-L50.
- [34]. G. Romano, M. Vignolo, V. Braccini, *et al.*, High-energy ball milling and synthesis temperature study to improve superconducting properties of MgB₂ *ex-situ* tapes and wires. *IEEE Trans. on Appl. Supercond.*, Vol. 19, No. 3, Jun. 2009, 2706-2709.
- [35]. C E J Dancer, D Prabhakaran, A Crossley, *et al.*, The effects of attrition and ball milling on the properties of magnesium diboride. *Supercond. Sci. Technol.* 23 (2010) 065015 (10pp).
- [36]. Jinyuan Ma, Aimin Sun, Guidan Wei, *et al.*, Al-Doping Effects on the Structural Change of MgB₂, *J. Supercond. Nov. Magn.* (2010) 23: 187-191.
- [37]. J.Y. Xiang, D.N. Zheng, J.Q. Li, *et al.*, Effects of Al doping on the superconducting and structural properties of MgB₂. *Physica C.* 386 (2003) 611-615.
- [38]. M. Putti, M. Affronte, P. Manfrinetti, *et al.*, Effects of Al doping on the normal and superconducting properties of MgB₂: A specific heat study. *Physical Review B* 68, 094514 (2003).
- [39]. R.H.T. Wilke, S.L. Bud'ko, P.C. Canfield, *et al.*, Superconductivity in MgB₂ doped with Ti and C. *Physica C* 418 (2005) 160-167.
- [40]. N Hörhager, M Eisterer, H W Weber, *et al.*, Ti and Zr doped MgB₂ bulk superconductors, *Journal of Physics: Conference Series.* 43 (2006) 500-504.
- [41]. Y. Zhao, C. Kea, C.H. Cheng, *et al.*, Concurrent doping effect of Ti and nano-diamond on flux pinning of MgB₂, *Physica C.* 470 (2010) 1096-1099.
- [42]. Y. Zhao, Y. Feng, C. H. Cheng, *et al.*, High critical current density of MgB₂ bulk superconductor doped with Ti and sintered at ambient pressure. *Appl. Phys. Lett.*, Vol. 79, No. 8, 20-Aug-2001, pp. 1154-1156.
- [43]. Y. Feng, Y. Zhao, Y. P. Sun, *et al.*, Improvement of critical current density in MgB₂ superconductors by Zr doping at ambient pressure. *Appl. Phys. Lett.*, Vol. 79, No. 24, 10-Dec-2001, pp. 3983-3985.
- [44]. Y. Zhao, Y. Feng, D.X. Huang, *et al.*, Doping effect of Zr and Ti on the critical current density of MgB₂ bulk superconductors prepared under ambient pressure. *Physica C*, Vol. 378–381 (2002), pp. 122-126.
- [45]. G. J. Xu, J. C. Grivel, A.B. Abrahamsen, *et al.*, Superconducting properties of Zn and Al double-doped Mg_{1-x}(Zn_{0.5}Al_{0.5})_xB₂, *Physica C.* 403 (2004) 113-118.
- [46]. W. X. Li, Y. Li, M. Y. Zhu, *et al.*, Effect of magnetic field processing on the microstructure of micronsize Zn doped MgB₂, *Physica C.* 460-462 (2007)

310–311.

- [47]. Zongqing Ma, Hai Jiang and Yongchang Liu, *et al.*, The acceleration of low-temperature sintering of MgB₂ bulks with high critical density by minor Sn doping, *Supercond. Sci. Technol.* 23 (2010) 025005 (4pp).
- [48]. Markus Kuhberger, Gerhard Gritzner. Effects of Sn, Co and Fe on MgB₂, *Physica C* 370 (2002) 39-43.
- [49]. C.H. Cheng, Y. Yang, C. Ke, *et al.*, Iron doping effect on superconducting properties of MgB₂. *Physica C.* 470 (2010) 1092-1095.
- [50]. Yoshihide Kimishima, Masatomo Uehara, Tetsuji Kuramoto, *et al.*, La-doping effects on pinning properties of MgB₂ *Physica C* 412-414 (2004) 402-406.
- [51]. Chandra Shekhar, Rajiv Giri, R S Tiwari, *et al.*, Effect of La doping on microstructure and critical current density of MgB₂, *Supercond. Sci. Technol.* 18 (2005) 1210-1214.
- [52]. Y. G. Zhao, X. P. Zhang, P. T. Qiao, *et al.*, Effect of Li doping on structure and superconducting transition temperature of Mg_{1-x}Li_xB₂, *Physica C* 361 (2001) 91-94.
- [53]. H.L. Li, K.Q. Ruan, S.Y. Li, *et al.*, Upper critical field and the effect of Li doping on the activation energy in MgB₂, *Physica C* 386 (2003) 560-564.
- [54]. I Pallechi, P Brotto, C Ferdeghini, *et al.*, Investigation of Li-doped MgB₂, *Supercond. Sci. Technol.* 22 (2009) 095014 (12pp).
- [55]. C Y Zhang, Y B Wang, W W Hu, *et al.*, The effect of Si addition in MgB₂ thin films by hybrid physical–chemical vapor deposition using silane as the doping source, *Supercond. Sci. Technol.* 23 (2010) 065017 (7pp).
- [56]. A. V. Pogrebnyakov, X. X. Xi, J. M. Redwing, *et al.*, Properties of MgB₂ thin films with carbon doping, *Appl. Phys. Lett.*, Vol. 85, No. 11, 13-Sep-2004, 2017-2019.
- [57]. R. H.T.Wilke, S. L. Bud'ko, P. C. Canfield, *et al.*, Systematic Effects of Carbon Doping on the Superconducting Properties of Mg(B_{1-x}C_x)₂, *Physical Review Letters*, Vol. 92, No. 21, 28-May-2004, 217003.
- [58]. Xianping Zhang, Yanwei Ma, Zhaoshun Gao, *et al.*, Effect of nano-C doping on the critical current density and flux pinning of MgB₂ tapes, *IEEE Trans. on Appl. Supercond.*, Vol. 17, No. 2, Jun. 2007, 2915-2918.
- [59]. C. B. Eom, M. K. Lee, J. H. Choi, *et al.*, High critical current density and enhanced irreversibility field in superconducting MgB₂ thin films, *Nature*, Vol 411, 31-May-2001, pp. 558-560.
- [60]. M.J. Mehl, D.A. Papaconstantopoulos, D.J. Singh, Effects of C, Cu and Be Substitutions in Superconducting MgB₂, *arXiv:cond-mat/0104548*.
- [61]. K. Q. Ruan, Z. M. Lv, H. Y. Wu, *et al.*, Enhanced critical current properties of MgB₂ bulks by doping amorphous carbon containing magnetic impurity, *J. Supercond. Nov. Magn.*, (2008) 21: 237-242.
- [62]. Chandra Shekhar, Rajiv Giri, R. S. Tiwari, *et al.*, Enhancement of flux pinning

- and high critical current density in graphite doped MgB₂ superconductor, *Journal of applied physics*, 102, 093910 (2007).
- [63]. L. Miu, G. Aldica, P. Badica, *et al.*, Improvement of the critical current density of spark plasma sintered MgB₂ by C60 addition, *Supercond. Sci. Technol.* 23 (2010) 095002 (5pp).
- [64]. C H Cheng, H Zhang, Y Zhao, *et al.*, Doping effect of nano-diamond on superconductivity and flux pinning in MgB₂, *Supercond. Sci. Technol.* 16 (2003) 1182-1186.
- [65]. J. H. Kim, W. K. Yeoh, X. Xu, *et al.*, Improvement of upper critical field and critical current density in single walled CNT doped MgB₂/Fe wires, *IEEE Trans. on Appl. Supercond.*, Vol. 17, No. 2, Jun. 2007, 2907-2910.
- [66]. Wen Xian Li, Ying Li, Rong Hua Chen, *et al.*, Increased superconductivity for CNT doped MgB₂ sintered in 5T pulsed magnetic field, *IEEE Trans. on Appl. Supercond.*, Vol. 19, No. 3, June 2009, 2752-2755.
- [67]. S. K. Chen, K. S. Tan, B. A. Glowacki, *et al.*, Effect of heating rates on superconducting properties of pure MgB₂, carbon nanotube- and nano-SiC-doped in situ MgB₂/Fe wires, *Appl. Phys. Lett.*, 87, 182504 (2005).
- [68]. S. X. Dou, S. Soltanian, J. Horvat, *et al.*, Enhancement of the critical current density and flux pinning of MgB₂ superconductor by nanoparticle SiC doping, *Appl. Phys. Lett.* Vol. 81, No. 18, 28-Oct.-2002, 3419-3421.
- [69]. Z X Shi, M A Susner, M D Sumption, *et al.*, Doping effect and flux pinning mechanism of nano-SiC additions in MgB₂ strands, *Supercond. Sci. Technol.* 24 (2011) 065015 (7pp).
- [70]. Akiyasu Yamamoto, Jun-ichi Shimoyama, Shinya Ueda, *et al.*, Effects of B₄C doping on critical current properties of MgB₂ superconductor, *Supercond. Sci. Technol.* 18 (2005) 1323-1328.
- [71]. P Lezza, C Senatore, and R Flukiger, Improved critical current densities in B₄C doped MgB₂ based wires, *Supercond. Sci. Technol.* 19 (2006) 1030-1033.
- [72]. H Yamada, M Hirakawa, H Kumakura, *et al.*, Effect of aromatic hydrocarbon addition on in situ powder-in-tube processed MgB₂ tapes, *Supercond. Sci. Technol.* 19 (2006) 175-177.
- [73]. J. H. Kim, S. Zhou, M. S. A. Hossain, *et al.*, Carbohydrate doping to enhance electromagnetic properties of MgB₂ superconductors, *Appl. Phys. Lett.*, 89, 142505 (2006).
- [74]. J. Wang, Y. Bugoslavsky, A. Berenov, *et al.*, High critical current density and improved irreversibility field in bulk MgB₂ made by a scaleable, nanoparticle addition route, *Appl. Phys. Lett.* 81, (2002) 2026-2028.
- [75]. X F Rui, Y Zhao, Y Y Xu, *et al.*, Improved flux pinning behaviour in bulk MgB₂ achieved by nano-SiO₂ addition, *Supercond. Sci. Technol.* 17 (2004) 689-691.
- [76]. S. Ueda, J. Shimoyama, A. Yamamoto, *et al.*, Enhanced critical current properties observed in Na₂CO₃-doped MgB₂. *Supercond. Sci. Technol.* 17 (2004)

926-929.

- [77]. P. C. Canfield, D. K. Finnemore, S. L. Bud'ko *et al.* Superconductivity in dense MgB₂ wires. *Phys. Rev. Lett.*, 2001, 86(11): 2423-2426.
- [78]. Y Feng, Y Zhao, A K Pradhan, *et al.*, Fabrication and superconducting properties of MgB₂ composite wires by the PIT method, *Supercond. Sci. Technol.* 15 (2002) 12-15
- [79]. K Yamamoto, K Osamura, S Balamurugan, *et al.*, Mechanical and superconducting properties of PIT-processed MgB₂ wire after heat treatment, *Supercond. Sci. Technol.* 16 (2003) 1052-1058
- [80]. A Malagoli, C Bernini, V Braccini, *et al.*, Fabrication and superconducting properties of multifilamentary MgB₂ conductors for AC purposes: twisted tapes and wires with very thin filaments. *Supercond. Sci. Technol.* 22 (2009) 105017.
- [81]. M. D. Sumption, M. Bhatia, S. X. Dou, *et al.*, Irreversibility field and flux pinning in MgB₂ with and without SiC additions. *Supercond. Sci. Technol.* 17, (2004) 1180-1184.
- [82]. J. M. Hur, K. Togano, A. Matsumoto, *et al.*, Fabrication of high-performance MgB₂ wires by an internal Mg diffusion process. *Supercond. Sci. Technol.* 21, 032001 (2008).
- [83]. G. Giunchi, C. Orecchia, L. Malpezzi, *et al.*, Analysis of the minority crystalline phases in bulk superconducting MgB₂ obtained by reactive liquid Mg infiltration. *Physica C.* 433, 182-188 (2006).
- [84]. K Tachikawa, Y Yamada, K Katagiri, *et al.*, Effects of metal powder addition in Ni-sheathed PIT MgB₂ tapes. *Advances in cryogenic engineering: Transactions of the international cryogenic materials conference*, 2004, Vol. 50, 561-568.
- [85]. Satoru Murase, Toshiaki Ohzawa, Takashi Harada, *et al.*, Self-field loss in AC transport current of Ni-sheathed MgB₂ superconducting tapes, *IEEE Trans. on Appl. Supercond.*, Vol. 16, No. 2, Jun. 2006, 1403-1406.
- [86]. K. Mizuno, D. Uchiyama, M. Maeda, *et al.*, Microstructure and critical current densities of MgB₂/Cu wires. *IEEE Trans. on Appl. Supercond.*, 2005, 15(2): 3345-3348.
- [87]. T. Nakane, K. Takahashi, H. Kitaguchi, *et al.*, Fabrication of Cu-sheathed MgB₂ wire with high J_c-B performance using a mixture of in situ and ex situ PIT techniques, *Physica C* 469 (2009) 1531-1535.
- [88]. N. M. Strickland, R. G. Buckley, A. Otto, *et al.*, Enhanced critical current densities in Cu-sheathed MgB₂. *Current Applied Physics.* Vol. 4 (2004) 688-692.
- [89]. H. Fang, P. Gijvanekar, Y. X. Zhou, *et al.*, Development of Fe-sheathed MgB₂ wires and tapes for electric power applications. *IEEE Trans. on Appl. Supercond.*, Vol. 15, No. 2, Jun. 2005, pp. 3200-3203.
- [90]. Dongliang Wang, Yanwei Ma, Zhengguang Yu, *et al.*, Strong influence of precursor powder on the critical current density of Fe-sheathed MgB₂ tapes. *Supercond. Sci. Technol.* 20 (2007) 574-578.

- [91]. P Kovac, I Husek, T Melisek, *et al.*, MgB₂ composite wires with Fe, Nb and Ta sheaths. *Supercond. Sci. Technol.* 19 (2006) 600-605.
- [92]. V. Beilin, I. Felner, M.I. Tsindlekht, *et al.*, Critical state instability in Nb-clad MgB₂ superconducting wires, *Physica C*, 2008, 468: 223-228.
- [93]. K. J. Song, N. J. Lee, H. M. Jang, *et al.*, Single-filament composite MgB₂/stainless-steel ribbons by powder-in-tube process, *Physica C*, 370 (2002) 21-26.
- [94]. K. J. Song, S. W. Kim, C. Park, *et al.*, The effect of geometry of composite MgB₂/stainless-steel (SS) wires fabricated by PIT process on the superconducting properties. *Physica C*. 407 (2004) 17-22.
- [95]. Fu B Q, Feng Y, Yan G, *et al.*, High critical current density in Ti-doped MgB₂/Ta/Cu tape by powder-in-tube process. *J. Appl. Phys.*, 2002, 92(12): 7341-7344.
- [96]. Kumakura H, Matsumoto A, Fujii H, *et al.*, High transport critical current density obtained for powder-in-tube processed MgB₂ tapes and wires using stainless steel and Cu-Ni tubes, *Appl. Phys. Lett.*, 2001, 79: 2435-2437.
- [97]. Goldacker W, Schlachter S I, Zimmer S, *et al.*, High transport currents in mechanically reinforced MgB₂ wires. *Supercond. Sci. Technol.*, 2001, 14: 787-793.
- [98]. Q. Y. Wang, G. F. Jiao, G. Q. Liu, *et al.*, Fabrication and properties of multifilamentary MgB₂ wires by *in-situ* powder-in-tube process, *Physica C*, 470 (2010) 1415-1418.
- [99]. K. Tanaka, H. Kitaguchi, H. Kumakura, *et al.*, Fabrication and Transport Properties of MgB₂ Mono-Core Wire and Solenoid Coil, *IEEE Trans. on Appl. Supercond.*, 2005, 15(2): 3180-3183.
- [100]. Columbus Superconductors srl <http://www.columbussuperconductors.com/>
- [101]. A Stenvall, I Hiltunen, A Korpela, *et al.*, A checklist for designers of cryogen-free MgB₂ coils, *Supercond. Sci. Technol.* 20 (2007) 386-391
- [102]. M Tomsic, M Rindfleisch, J Yue, *et al.*, Development of magnesium diboride (MgB₂) wires and magnets using in situ strand fabrication method, *Physica C*, 456 (2007) 203-208
- [103]. Marco Razeti, Silvano Angius, Leonardo Bertora, *et al.*, Construction and operation of cryogen free MgB₂ magnets for open MRI systems. *IEEE Trans. on Appl. Supercond.*, Vol. 18, No. 2, June 2008, 882-886.
- [104]. Rossella B. Dalessandro, Marco Bocchi, Valerio Rossi. *et al.*, Test Results on 500 kVA-Class MgB₂-Based Fault Current Limiter Prototypes, *IEEE Trans. on Appl. Supercond.*, Vol. 17, No. 2, Jun-2007, pp. 1776-1781.
- [105]. <http://www.the-infoshop.com/report/bc134594-superconductor.html> (Superconductors: Technologies and Global Markets).
- [106]. S.C. Yan, G. Yan, C.F. Liu, *et al.*, Experimental study on the phase formation for the Mg-B system in Ar atmosphere. *Journal of Alloys and Compounds*, 437 (2007) 298-301.

- [107]. Kim J H, Dou S X, Wang J L, *et al.*, The effects of sintering temperature on superconductivity in MgB₂/Fe wires. *Supercond. Sci. Technol.* 20(2007) 448-451.
- [108]. Gumbel A, Eckert J, Fuchs G, *et al.* Improved superconducting properties in nanocrystalline bulk MgB₂. *Appl. Phys. Lett.*, 2002, 80: 2725-2727.
- [109]. C R M Grovenor, L Goodsir, C J Salter, *et al.*, Interfacial reactions and oxygen distribution in MgB₂ wires in Fe, stainless steel and Nb sheaths. *Supercond. Sci. Technol.* 17 (2004) 479-484.
- [110]. Th. Schuster, H. Kuhn, E. H. Brandt. *et al.*, Current and field pattern in rectangular and inhomogeneous superconductors. *Phys. Rev. B.* 52, 10375-10389 (1995).
- [111]. H. Okamoto. B-Nb (Boron-Niobium). *Journal of Phase Equilibria and Diffusion.* Vol. 31 No. 2. 2010. 208-209.
- [112]. Mati Raudsepp, Recent advances in the electron-probe micro-analysis of minerals for the light elements. *The Canadian Mineralogist.* 33, 203-218. 1995.
- [113]. M. D. Sumption, M. A. Susner, M. Bhatia, *et al.*, High Critical Current Density Multifilamentary MgB₂ Strands, *IEEE Trans. on Appl. Supercond.*, Vol. 17, No. 2, Jun-2007, pp. 2838-2841.
- [114]. Minyi Fu, Zhengquan Pan, Zhengkuan Jiao, *et al.*, Quench characteristics and normal zone propagation of an MgB₂ superconducting coil. *Supercond. Sci. Technol.* 17 (2004) 160-163.
- [115]. Sumption, M.D. Collings, E.W. Stability and flux jumping of internal-Sn, Nb₃Sn conductors (and a model system MgB₂). *IEEE Trans. on Appl. Supercond.*, Vol. 13, No. 2, June 2003, 3394-3397.
- [116]. H Kitaguchi and H Kumakura. Superconducting and mechanical performance and the strain effects of a multifilamentary MgB₂/Ni tape. *Supercond. Sci. Technol.* 18 (2005) S284-S289.
- [117]. P Kovac, M Dhalle, T Melisek, *et al.*, Dependence of the critical current in ex situ multi- and mono-filamentary MgB₂/Fe wires on axial tension and compression. *Supercond. Sci. Technol.* 16 (2003) 600-607.
- [118]. P Kovac, I Husek, T Melisek, *et al.*, Stainless steel reinforced multi-core MgB₂ wire subjected to variable deformations, heat treatments and mechanical stressing. *Supercond. Sci. Technol.* 23 (2010) 065010 (7pp).

PUBLICATIONS

1. **Wang Qingyang**, Yan Guo, Liu Guoqing, Li Chengshan, Lu Yafeng, Zhang Pingxiang. Superconductivity of MgB₂/NbZr/Cu Wires with B₁₀C Doping. *Rare Metal Materials and Engineering*, 2008, 37(S4): 83~86.
2. **Wang Qingyang**, Yan Guo, Liu Guoqing, Jiao Gaofeng, Xiong Xiaomei, Feng Yong, Zhang Pingxiang. Effect of Heat treatment temperature on MgB₂/Nb/Cu Wires with carbon doping. *Chinese Journal of Low Temperature Physics*. 2010, 32(2): 133~137.
3. **Wang Qingyang**, Jiao Gaofeng, Liu Guoqing, Xiong Xiaomei, Zhang Pingxiang, Andre Sulpice, Eric Mossang, Feng Yong, Yan Guo. Fabrication and properties of multi-filamentary MgB₂/NbCu wires by *in-situ* PIT process. *Physica C*, 470 (2010): 1415~1418.
4. **Wang Qingyang**, Yan Guo, Andre Sulpice, Liu Guoqing, Jiao Gaofeng, Xiong Xiaomei, Feng Yong, Zhang Pingxiang. Fabrication and Properties of Multi-Filamentary MgB₂ Wires with Nb Reinforcement. *Chinese Journal of Low Temperature Physics*. 2011, 33(3): 199~202.
5. **Wang Qingyang**, Yan Guo, Andre Sulpice, Zhang Pingxiang. Progress of multi-filamentary MgB₂ superconductor wires and tapes. *Materials Review*. 2011, 25(9)A: 33~36.
6. **Wang Qingyang**, Yan Guo, Zhang Pingxiang, Andre Sulpice, Yang Fang, Xiong Xiaomei, Feng Jianqing, Ji Ping, Li Chengshan. Influence of Bending Stress on Mono- and Multi- filamentary MgB₂/Nb/Cu Wires, *Physica C*, (2013) 484: xxx-xxx.
7. **Wang Qingyang**, Yan Guo, Andre Sulpice, Eric Mossang, Zhang Pingxiang. Influence of Amorphous Carbon Doping on Superconductivity of MgB₂/Nb/Cu Wires. *Rare Metal Materials and Engineering*, 2012, 41(10): 1709~1712..
8. **Wang Qingyang**, Zhang Pingxiang, Yan Guo, Andre Sulpice, Xiong Xiaomei, Yang Fang, Liu Guoqing, Jiao Gaofeng, Li Chengshan. Influence of Nb Diffusion Layer on Superconductivity of MgB₂/Nb/Cu Wires. *Rare Metal Materials and Engineering*. Accepted.
9. Yan Guo, **Wang Qingyang**, Liu Guoqing, Yang Huan, Li Chengshan, Lu Yafeng, Wen Haihu. Fabrication and Superconducting Properties of MgB₂ Wires with Amorphous Carbon Doping by *In situ* Powder-in-tube Method. *Science and Technology Review*, 2008, 26(1): 28~32.
10. Yan Guo, **Wang Qingyang**, Liu Guoqing, Xiong Xiaomei, Feng Yong, Sulpice A, Mossang E. Fabrication and Properties of Multifilamentary MgB₂/NbZr/Cu Wires. *Materials China*, 2009, 28(4): 23~27.
11. Liu Guoqing, **Wang Qingyang**, Sun Yuyan, Xiong Xiaomei, Jiao Gaofeng, Yan Guo. The Effect of Heat treatment Temperature on Microstructure and Properties of mono-filamentary MgB₂/Fe/Cu Wires with Carbon doping. *Chinese Journal of Low Temperature Physics*. 2011, 33(2): 116~119.

12. Sun Yuyan, **Wang Qingyang**, Yang Fang, Xiong Xiaomei, Qi Ming, Liang Ming, Yan Guo, André Sulpice, Zhang Pingxiang. Mechanical and superconducting properties of 6-filament MgB₂ wires reinforced by Cu, Cu-Nb and NbTi. *Physica C*, 2012, 477: 56-62.
13. Feng Jianqing, **Wang Qingyang**, Xiong Xiaomei, Chen Sihua, Bai Zhiming, Yang Fang, Liu Guoqing, Jiao Gaofeng, Yan Guo, Li Chengshan. Study on Quenching Characteristic of MgB₂ Wires Doped by Carbon. *Chinese Journal of Low Temperature Physics*. 2012, 34(2): 90~93.
14. Li Chengshan, **Wang Qingyang**, Yan Guo, A.Sulpice, Xiong Xiaomei, Yang Fang, Liu Guoqing, Jiao Gaofeng, Jia Jialin, Zhang Pingxiang. Fabrication and Properties of Kilometer Level Multi-filamentary MgB₂/Nb/Cu Wires. *Chinese Journal of Low Temperature Physics*. 2012, 34(4): 292~296.
15. Liu Guoqing, Yan Guo, **Wang Qingyang**, Lu Yafeng. The Effect of Heat treatment Temperature on Microstructure and Properties of MgB₂/Fe/Cu Wires. *Rare Metal Materials and Engineering*, 2008, 37(S4): 444~447.
16. Yan Shicheng, Zhou Lian, Yan Guo, **Wang Qingyang**, Lu Yafeng. Effect of carbon doping on the formation and stability of MgB₂ phase. *Journal of Alloys and Compounds*, 2008, 459: 452~456.
17. Shan Di, Liu Guoqing, Jiao Gaofeng, **Wang Qingyang**, Tang Xiaodong, Yan Guo, Feng Yong. Microstructure and Superconductivity of MgB₂/Nb/Cu with TiC Doping by Two Step Reaction Method, *Chinese Journal of Low Temperature Physics*. 2009, 31(5): 223~226.
18. Xiong Xiaomei, Yan Guo, Liu Guoqing, **Wang Qingyang**, Feng Yong. Phase and micro-structure comparison of pure and carbon doped MgB₂ superconducting bulks during acid exposure, *Rare Metal Materials and Engineering*, 2009, 38(9): 1526~1529.
19. Shan Di, Yan Guo, Zhou Lian, Li Chengshan, **Wang Qingyang**, Xiong Xiaomei. Large Ti₃SiC₂ bulks fabricated by infiltration method, *Rare Metal Materials and Engineering*, 2011, 40(S3): 372-375.
20. Shan Di, Yan Guo, Zhou Lian, Li Chengshan, **Wang Qingyang**, Zhang Shengnan, Yang Fang, Liu Guoqing. Effect of Ti₃SiC₂ doping on critical current density and flux pinning in MgB₂. *Rare Metal Materials and Engineering*, 2012, 41(7): 1135-1138
21. Shan Di, Yan Guo, Zhou Lian, Ji Ping, Li Chengshan, **Wang Qingyang**, Zhang Shengnan, Yang Fang, Liu Guoqing. The effect of Ti₃SiC₂ doping on the microstructure and superconducting properties of MgB₂. *Physics Procedia*, 2012, 27, 172-175.
22. K.Q. Ruan, Z.M. Lv, H.Y. Wu, S.L. Huang, M. Li, Z.Q. Pang, **Q.Y. Wang**, Y. Feng, G. Yan. Enhanced Critical Current Properties of MgB₂ Bulks by Doping Amorphous Carbon Containing Magnetic Impurity, *J. Supercond. Nov. Magn.*, 2008, 21: 237~242.

ABSTRACT

Mono- and multi-filamentary MgB₂ wires sheathed with Nb/Cu composite tube have been elaborated by *in-situ* powder-in-tube (PIT) technique, pure or with carbon and TiC doping, and heat treated between 600 and 950 °C. The structural and physical properties of the wires were investigated by XRD, SEM, magneto-optical imaging, magnetization, etc. Substitution of B for C depresses T_c slightly but enhances the flux pinning, with the result of optimized performances of $J_c(H)$ in high field, with a partial amorphous C substitution and a control of the processing parameters. For the samples reacted at high temperature, there is a diffusion layer at the interfacial region between the Nb sheath and MgB₂, which is non-superconducting and obstructs the current transmission : the best heat treatment for the MgB₂ wires with Nb as the barrier layer should be lower than 750 °C. The Cu-clad 6-, 12-, and 36-filamentary MgB₂ wires with Nb buffer layer also have been fabricated by the *in-situ* PIT method. To improve the strength of wires, the Nb-core was used as the central filament. The results show that the *in-situ* PIT technique can be used to produce long length multifilamentary MgB₂/Nb/Cu wires, as a result of the well workability of the composite.

Keywords: magnesium diboride, chemical doping, powder-in-tube technique, superconductivity, critical current.

RESUME

Des conducteurs mono- ou multi-filamentaires de MgB₂ dans une gaine Nb/Cu ont été élaborés par une technique PIT (Powder-In-Tube), purs ou dopés au carbone ou TiC, et traités thermiquement entre 600 et 950 °C. Nous avons étudié leurs caractéristiques structurales et leurs propriétés physiques par des mesures de RX, MEB, imagerie magnéto-optique, aimantation, etc. La substitution de B par C diminue légèrement la T_c mais augmente le piégeage du flux, améliorant ainsi le courant critique $J_c(H)$ en fort champ. Nous avons mis en évidence que pour les températures de traitements thermiques supérieures à 750 °C, il apparaît une couche de diffusion résistive à l'interface entre la gaine Nb et MgB₂ qui empêche le transfert du courant entre la matrice et le supraconducteur. Par suite, les meilleures performances de J_c sont obtenues pour un traitement à 700 °C par des mesures de courant de transport et pour 800 °C par des mesures d'aimantation, insensibles à cette couche de diffusion. Nous avons fabriqué des conducteurs de 6, 12 ou 36 filaments de MgB₂ avec des barrières de Nb dans une matrice de cuivre par la méthode PIT, en utilisant un filament central de Nb pour renforcer mécaniquement le conducteur. Nos résultats montrent que cette technique peut être utilisée pour produire des conducteurs MgB₂/Nb/Cu de longueur kilométrique grâce à la bonne fonctionnalité du composite.

Mots-clés: diborure de magnésium, dopage chimique, technique PIT, supraconductivité, courant critique.